The Spatial Resolution Achievable with Parametric Pulse Shape Analysis of AGATA Detectors and its Application to In-beam Data

Thesis submitted in accordance with the requirements of the University of Liverpool for the degree of Doctor in Philosophy

by

Laura Nelson

Oliver Lodge Laboratory

2008

Abstract

The next generation γ-ray spectrometer designed for nuclear structure studies will consist of a large array of highly segmented High-Purity Germanium (HPGe) detectors, capable of tracking the path of scattered γ-rays. The energy deposited at each instance of the scattered photon will be added back to reconstruct a full energy event in a technique known as Gamma Ray Tracking (GRT). The photon interaction positions within the detecting volume will be determined to within a few millimetres by Pulse Shape Analysis (PSA) of the charge signals produced at the electric contacts.

Three prototype detectors for the Advanced GAmma Tracking Array (AGATA) [Ge01] have been constructed and tested. The n-type HPGe, highly segmented detectors each have 36 outer electrodes and are of closed ended coaxial configuration. The current work combines the results of detailed photon scans of two of these prototype detectors, providing a spatial calibration based on parameterisations of the digitised pulses obtained. The calibration in two dimensions throughout the volume of the detectors, is then applied to an experimental data set.

The experiment was performed at IKP Köln in summer 2005, and consisted of a 100MeV ^{48}Ti beam incident on a deuterated target using inverse kinematics. A mixture of reaction channels was created at $\sim$6.5% v/c. Three prototype AGATA detectors, 108 detecting elements in total, were in a single cryostat creating a modular triple cluster unit. An annular silicon strip detector was used to determine the energy and the angle of the recoils in order to perform a veracious Doppler correction. The Doppler correction of the spectral peaks obtained was improved due to the decreased solid angle subtended by the physical segmentation of the detector. Furthermore, the Doppler broadening reduction is improved by, firstly, determining the radius of interactions using the risetime analysis of the scan data, and secondly, determining the azimuthal angle of interactions using the image charge analysis of the scan data.

The spatial resolution achievable with this simple parametric pulse shape analysis approach is inferred. It will provide a direct and independant means of assessing the efficacy of PSA algorithms which are based on the use of theoretically calculated pulse shapes. Moreover, satisfactory results in the present work, and evidence of crystal to crystal reproducibility, will greatly simplify the future use of the tracking array by eliminating the need for basis data set generation. The results of this analysis are therefore of great consequence to the nuclear structure community.

Contents

List of Figures

List of Tables

Chapter 1

Introduction

1.1 Background and Motivation

The structure of the nucleus, one of the most fundamental entities in the Universe, is still largely unexplained by modern physics. Indeed no mathematical model currently exists which can accurately be applied to all nuclei. Naturally, this has been the driving force behind nuclear scientists' research for many decades. Of the thousands of known isotopes, a large proportion have been studied and many nuclear models have been constructed with some success. For example, the Strutinsky shell correction [St67, St68] to the Liquid Drop Model or the Skyrme-Hartree-Fock mean field approach [Cw96] are both used to predict aspects of nuclear behaviour such as the location of the superheavy magic N and Z numbers. There are however limitations to current experimental techniques preventing the procurement of results for rarer nuclei. Recent progress in detector characterisation [De05] and technology has enabled the design of γ-ray spectrometers which will address these limitations [Le03]. Thus, this field of research currently lies at the brink of a proliferation of previously unobtainable results which could ultimately lead to greater understanding of the nuclear force.

1.2 Limitations to Current Experimental Techniques

Experimental methods in nuclear physics include the production and study of nuclei in excited states; the gamma rays they emit as they subsequently decay can be detected and their properties are indicative of the nucleonic arrangement and movement. Currently, the most advanced γ-ray spectrometers designed for this purpose are made of a number of High-Purity Germanium (HPGe) detectors, namely Gammasphere [De88] and Euroball [Si97]. They rely on Compton suppression shielding to veto those events in which a photon scatters out of a primary detecting element before depositing its full energy [No94, Be96]. Although this technique reduces the unwanted background continuum, it is detrimental to the detection efficiency; not only are many events disregarded in the process but the solid angle coverage of HPGe is reduced by the presence of the shields themselves.

Furthermore, as the nuclei under investigation can often be moving at a significant fraction of the speed of light, the energy of the γ-rays they emit can be subject to a Doppler shift. The Doppler shifted energy can be reconstructed with the knowledge of the incident photons' trajectory from its path of origination (that of the recoiling nucleus). However, this angle will have an uncertainty associated with the size of the solid angle subtended by the detecting element, manifested as a degraded spectral energy resolution.

Further experimental challenges lie in the physical creation of nuclei which lie far from stability and, to this end, Radioactive Ion Beam (RIB) facilities have been developed in recent years. This has further propelled the necessity for improvements to current γ-ray spectrometer designs as these elusive nuclei will undoubtedly have a low production rate, leading to poor statistics, and exist in the extreme conditions of velocity and background.

1.3 The Future of Nuclear γ-ray Spectroscopy

The next generation of γ-ray spectrometers designed for nuclear structure studies will consist of a large array of highly segmented High-Purity Germanium (HPGe) detectors, capable of tracking the path of scattered γ-rays. The energy deposited at each instance of the scattered photon can be added back to reconstruct a full energy event. This technique is known as Gamma-Ray Tracking (GRT) [Sc99]. While the granularity achieved by the segmentation of the detector will affect the tracking process, the spatial resolution, and thus the tracking capability, provided by each detecting volume can be improved by Pulse Shape Analysis (PSA) [Ve00a, Ve00b]. The photon interaction positions will be determined to within a few millimetres by interpretation of the digitised signals produced at the electric contacts. Tracking the photons will eliminate the requirement for Compton suppression shielding, permitting unparalleled efficiency, and the spatial information will provide excellent angular resolution, enabling a precise Doppler correction.

The ultimate realization of the Advanced GAmma Tracking Array (AGATA) will be a spherical shell comprised almost completely of HPGe material, creating the most efficient high resolution γ-ray spectrometer in the world [Ge01]. Three prototype AGATA detectors have been constructed and tested. The n-type HPGe, highly segmented detectors each have 36 outer electrodes and are of closed end coaxial configuration.

Presently, it is widely believed that a database of simulated pulse shapes for every spatial coordinate within each detecting volume must be constructed. The charge response of each electrode from an event will be fitted to this database in order to determine the most probable photon interaction position. Production of these pulse shapes using electric field simulation software is laborious and as yet no available software has been experimentally validated. Moreover, minimisation algorithms between simulated and experimental pulse shapes will be highly demanding on computer

power.

1.4 Aims of This Work

This work combines the results of detailed photon scans of the front faces of two prototype AGATA detectors with data from an in-beam experiment. The experiment provides a platform to test the detectors' ability to determine photon interaction locations through assessing the improvement to the spectral peaks following a Doppler correction utilising this spatial information. A spatial calibration based on polynomial fitting of pulse shape parameterisations of the scan data is achieved and this calibration is then used to locate photon interaction sites within the detecting volumes of events from the experimental data. The improvement to the energy resolution of the spectral peaks obtained in the experiment, following a Doppler correction incorporating this spatial information, is used to assess the effectiveness of the method.

This work will provide the only means of directly testing theoretical predictions relating the energy resolution obtained following a Doppler correction to the spatial resolution achieved using pulse shape analysis techniques.

Analysis and comparison of the prototype detectors' scan data is included in order to aid characterisation of the detectors. Greater understanding of the detector configuration and the implications to its functionality is promoted in the process.

Chapter 2

Fundamentals of γ-ray Detection in Nuclear Spectroscopy

The beginning of this chapter describes the mechanisms by which γ-radiation can interact with matter. It will be apparent that each of these processes results in the production of one or more unbound electrons providing the basis for an information carrying signal. This fact is exploited by semiconductors in order to detect the presence of the radiation; the physical principles and practicalities of which are also described.

2.1 γ-ray Interactions with Matter

Electromagnetic radiation incident on matter will attenuate according to the exponential relationship,

$$I = I_0 e^{-\mu x} \tag{2.1}$$

where I_0 is the original photon intensity, μ is a material and energy specific attenuation coefficient and is proportional to the interaction cross section, and x is the length of the material traversed. In the case of γ-rays, there are a number of different interaction mechanisms which cause this reduction in intensity and the total attenuation is the linear sum of the contributions of each of these processes. This is

illustrated in Figure 2.1 for germanium material. The type of interaction undergone is largely governed by the energy of the photon. The dominant effects for the energy range of interest for nuclear structure experiments ($\sim$0.1 to $\sim$20 MeV) are described in more detail below, however it should be noted that there are other processes such as Rayleigh, Thomson and Delbruck scattering which are small in comparison. It should also be observed that γ-rays are a highly penetrating form of radiation due to their lack of electronic charge and mass. If a significant level of efficiency is required, it is therefore necessary to place an emphasis on the amount of detecting material and consequently the volume becomes important for a low density γ-radiation detector. This is particularly relevant for higher energy photons which are more penetrating.

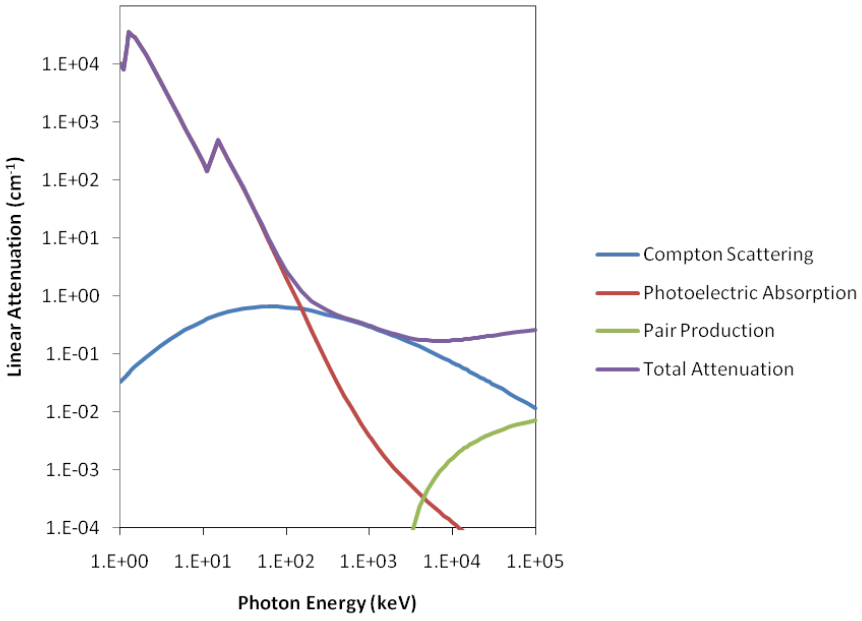

Figure 2.1: Total linear attenuation coefficient, μ, of γ-rays in germanium showing the relative contributions of photoelectric, Compton and pair production interactions. Data taken from [NI08c].

2.1.1 Photoelectric Absorption

Photoelectric absorption is the dominant process for low energy γ-rays, up to ∼150 keV. The photon is completely absorbed by an atom and energy is conserved by the release of a bound atomic electron. This process will only occur providing

$$E_\gamma = h\nu > B_e \tag{2.2}$$

where E_γ is the energy of the incident photon and B_e is the electron's binding energy. The kinetic energy of this ejected photoelectron is given by

$$T_e = E_\gamma - B_e. \tag{2.3}$$

The vacancy left behind in the low lying electron shell (K or L) is quickly filled by electron rearrangement from higher orbitals which also necessitates the release of binding energy as characteristic X-rays or low energy Auger electrons.

The probability of photoelectric absorption occurring, τ, is proportional to the n^{th} power of the proton number of the absorbing material, Z, where n is a number between 4 and 5, and inversely proportional to the γ-ray energy [Da52],

$$\tau \propto \frac{Z^n}{E_\gamma^{3.5}}. \tag{2.4}$$

2.1.2 Compton Scattering

The Compton scattering process is dominant for γ-rays in the approximate energy range 0.2 MeV $\leq$ E_γ $\leq$ 8 MeV. In this case, the incident photon is scattered by an outer shell electron and $E_\gamma \gg B_e$. This process causes only partial energy deposition and therefore adds to the spectral background, or Compton continuum, and not to the photopeak. Assuming that the electron is at rest, conservation of energy and momentum gives the remaining photon energy, E'_γ, as a function of the scattering angle, θ,

$$E'_\gamma = \frac{E_\gamma}{1 + (E_\gamma/m_0c^2)(1 - \cos\theta)} \tag{2.5}$$

where m_0c^2 is the electron rest mass energy [Da52]. The kinetic energy imparted to the electron is given by,

$$T_e = E_\gamma - E'_\gamma \tag{2.6}$$

and it can thus be shown that the maximum value of T_e occurs when θ=180°. Furthermore, there is a corresponding maximum portion of the photon energy that can be transferred, giving rise to the characteristic Compton edge observed in energy spectra.

The cross section for this process increases linearly with Z and is inversely proportional to E_γ. The Klein-Nishina formula calculates the differential cross section for Compton scattering as a function of scattering angle [Kl29],

$$\frac{\mathrm{d}\sigma}{\mathrm{d}\Omega} = Zr_0^2 \left(\frac{1}{1+\alpha(1-\cos\theta)}\right)^2 \left(\frac{1+\cos^2\theta}{2}\right) \left(1 + \frac{\alpha^2(1-\cos\theta)^2}{(1+\cos^2\theta)[1+\alpha(1-\cos\theta)]}\right) \tag{2.7}$$

where $\alpha \equiv (h\nu)/(m_0c^2)$ and r_0 is the classical electron radius. It is apparent from this formula that higher energy γ-rays have more inclination to forward scatter than those with lower energy. This is depicted in Figure 2.2.

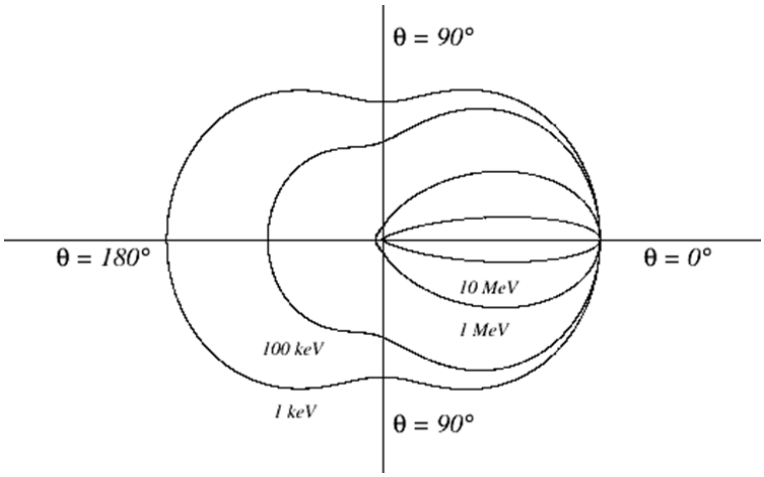

Figure 2.2: Polar plot of the angular distribution of scattered photons incident from the left for a selection of γ ray energies as predicted by the Klein-Nishina formula.

2.1.3 Pair Production

Pair production is the dominant interaction for high energy γ-rays. The presence of a nucleus in the absorbing material allows the creation of an electron-positron pair using the incident photons' energy. This is therefore required to be above the combined rest mass of the pair produced (1.022 MeV). Although this process is possible at this γ-ray energy, it is not dominant until the photons reach a much higher energy, as can be seen in Figure 2.1. The excess energy is shared between the kinetic energies of the electron and positron. Subsequent annihilation of the positron with an atomic electron in the material produces two back to back 511 keV γ-rays in close proximity to the photon interaction. The probability of this process occurring is approximately proportional to $\sqrt{Z}$ and, unlike the interaction mechanisms above, pair production increases with E_γ.

2.2 Basics of Semiconductor Physics

Semiconducting materials have many applications in technology due to their intrinsic and unique electric properties. The following section briefly discusses aspects of these properties that are relevant to the fabrication of a γ-radiation detector.

2.2.1 Electron Energy Bands in Solids

Allowed electron energy states in materials give rise to the band structures of both covalently bonded and free electrons, separated by an energy gap. This is the energy which must be overcome in order to excite an electron from the valence band to the conduction band where charge is free to move. The size of this band gap depends on the material itself, but, in general terms, its magnitude is largest in insulators ($\sim$5 eV), and smaller in semiconductors ($\sim$0.7 eV for Ge at room temperature) [Lu00]. In the case of metals the conduction band is already occupied. A physical result of this concept is that a relatively small amount of energy is required to excite the elec-

trons of semiconductor atoms to the conduction band and thus provide an information carrying signal. For this reason, Ge detectors are generally operated at liquid nitrogen temperature (77 K) in order that this excitation is predominantly caused from the energy of the incoming radiation, and not by thermal excitations which would exacerbate the system noise and result in a poorer energy resolution.

2.2.2 Crystal Structure and Doping

Semiconducting materials, such as Si and Ge, are crystalline in nature and can be grown such that a reasonable volume of material forms a single crystal lattice structure. They are tetravalent: each atom has four outer shell electrons which form covalent bonds with their neighbours. Electron excitation to the conduction band implies its bonds must be broken and a vacancy left behind in the lattice. This electron-hole pair is likely to recombine in the absence of an electric field. The concentrations of electrons and holes are equivalent in a pure (intrinsic) crystal and their sum is equal to the total number of intrinsic charge carriers. However the number of available information carriers, and hence the conductivity of the semiconductor, can be increased by the introduction of impurities into the crystal structure. In the case of an n-type crystal, the dopant is an element with 5 valence electrons, such as phosphorus, which replaces intrinsic atoms in the lattice. Consequently there is an unbound (or free) electron surplus of 1 for every impurity atom present. These electrons belong to neither the valence nor the conduction bands, as they are weakly bound to the impurity atom, so they reside in *Donor* energy states just below the conduction band. Similarly, p-type material will have a trivalent dopant, such as boron, in order to introduce an excess of holes which occupy *Acceptor* energy levels just above the valence band. The energy band structures of semiconductors is discussed in more detail in References [Sh50] and [Dr55].

2.2.3 The p-n Junction

From the description above, it is clear that p-type semiconductors have an excess of holes, while n-type have an excess of electrons. When p- and n-type semiconductors are in close contact, these free electrons and holes pertaining to each type of material are attracted to one another and diffuse across the junction until they recombine. A recombined electron-hole pair represents an electron which has filled a valence vacancy and is then bonded to a lattice atom. A non-conducting (or depleted) region is created extending from the junction. The impurity atoms from which the recombined charge carriers originate are now ionic; positively charged on the n-type side and negatively charged on the p-type. Their remaining covalent bonds prevent the charged atoms from moving from their lattice site, creating a space charge density. An electric potential is produced by this arrangement of ions and opposes further diffusion of electrons and holes until the depletion zone reaches an equilibrium state. The Poisson equation can be solved to give the value of this potential, ϕ, at any point,

$$\nabla^2\phi = -\frac{\rho}{\epsilon} \tag{2.8}$$

where ρ is the net charge density (space charge) and ϵ is the material specific dielectric constant. The resulting electric field, $\mathcal{E}$, can be calculated according to

$$\mathcal{E} = -\nabla\phi \tag{2.9}$$

and is evidently greatest at the region where the 2 types of material meet.

2.3 Semiconductor Radiation Detection

The fabrication and operation of a semiconductor detector is described in very general terms in this section. Particular emphasis is placed on that which fulfills the requirements of nuclear structure experiments.

2.3.1 Reverse Biasing

If the n-type material of a p-n junction (or diode) is given a positive electric potential with respect to the p-type, the diode is said to be reverse biased. This enhances the space charge electric field and causes the depletion region to extend further. The potential can be chosen sufficiently large to deplete the entire volume of the semiconductor. Moreover, increasing the potential further causes the field strength to increase and approach uniformity throughout the volume. The solution of Equations 2.8 and 2.9, applying the relevant boundary conditions, yields the following equation for the thickness of a depleted region, d,

$$d \cong \sqrt{\left(\frac{2\epsilon V}{eN}\right)} \tag{2.10}$$

where V is the applied reverse bias voltage, e is the electronic charge and N is the Donor or Acceptor concentration in the type of semiconductor that makes up the bulk of the material. This equation implies that, in order to facilitate a large depleted volume, N must be small on one side of the junction. In other words, the bulk of the material should be *high-purity*.

Within this depleted region, free electrons and holes created by incident ionising radiation, or indeed by any other means, will be swept to opposite sides of the junction by the electric field. Here they can be collected by electrical contacts at the material boundaries in order to signal the presence of the energy depositing radiation.

2.3.2 Electric Contacts

Continually flowing current is expected through a conductive medium under the application of an electric potential and this would overwhelm the small current of the free electrons caused by ionising radiation. It is therefore appropriate to block this leakage current using non-injecting (or blocking) contacts. This serves to restrict the flow of charge to one direction or, alternatively expressed, to allow one type of charge

carrier (electrons or holes) to flow. It is anticipated that there will still be some level of residual leakage current through the bulk of the crystal and also across its surface. This will add to the electronic noise and thus degrade the energy resolution achievable with the device.

Conveniently, blocking contacts can be provided by semiconducting material. The principal concept being; if a substance is nearing saturation of a charge species, the injection of further charges of the same type in to the volume would be restricted. If the bulk of the detector is of particular type, n (or p), then one of the blocking contacts is provided by the other type, p (or n). Therefore this contact, known as the rectifying contact, forms part of the diode itself as well as restricting the current flow. The rectifying contact will be heavily doped in comparison to the main body of the detector in order to compensate for its smaller volume. For the detectors of interest in this work, the other contact is generally of the same impurity type as the bulk of the detector and also serves as a blocking contact, but does not form part of the diode. For example, boron is used as the outer contact for the High-Purity Germanium AGATA detectors discussed in this work and lithium is used for the inner contact.

2.3.3 Detector Configuration

Germanium is currently the most suitable material for γ-radiation detection in the majority of nuclear structure experiments. This is primarily due to three main factors. The first is the superior energy resolution achievable with semiconducting material over other detectors, as described in Section 2.4.1. Moreover, at 77 K, both the ionisation energy and the Fano factor are lower for germanium than for silicon (these terms are described in Section 2.4). The second reason is the ability to produce High-Purity Germanium material (HPGe) and thus create larger depletion regions than is possible with silicon. Section 2.3.1 introduces this concept. The requirement for large detecting volumes in nuclear structure experiments was highlighted at the beginning of this chapter, as was the dependence of photon interaction, in particular

photoelectric, cross sections on Z. This leads directly to the third consideration: the atomic number for Ge is 32 compared to Z=14 for Si creating a considerably higher interaction cross section.

HPGe crystals are grown using the Czochralski technique [Or08]. Due to this process, the largest volume of crystalline Ge is fabricated with a cylindrical shape and this forms the basis of most large volume detectors. One of the two electric contacts is formed on the outer surface of the cylinder and covers all but its back face. From this face a bore hole is drilled along the cylinder's axis and the second electrode is applied to this inner cylindrical surface area. Figure 2.3 depicts a typical detector of this configuration. In order to minimise leakage currents on the crystal's front face and to maximise its solid angle coverage and active volume, the bore hole does not extend throughout the length of the cylinder to the front surface. This configuration is known as closed-ended coaxial. It is usual for the required low temperature to be provided by liquid nitrogen from a nearby dewar via a "cold finger" which is accomodated in the detector's axially drilled bore hole. Section 2.2.1 highlights the requirement for HPGe detectors to be operated at low temperature. The detector is therefore housed in an evacuated cryostat to thermally isolate the crystal from its surroundings and to avoid damage to the surface of the crystal which can promote surface leakage current.

It is preferable to fabricate the outer surface with the rectifying contact as the depletion region will extend from this surface inwards creating optimal (fully depleted) conditions in the bulk of the detecting volume. It can be seen in Figure 2.3 that the electrodes do not extend to the back face of the cylinder. This creates a passivated layer of germanium and acts as an electrostatic mirror in an attempt to prevent warping of the electric field lines away from the radial direction.

The detectors discussed in this work are of n-type germanium, which implies that the outer, and hence the rectifying, contact is of p-type material, termed the p^+

contact (cathode). It is believed that this configuration was preferentially chosen due to the ability to fabricate thinner p^+ contacts ($\sim$0.6 μm) using ion implantation, and hence provide a more suitable entrance window for the radiation. It is usual to produce the central contact to the order of $\sim$700 μm using diffusion methods. Moreover, damage caused by energetic radiation particles can remove Ge atoms from their lattice sites creating hole traps which hinder complete charge collection. The use of n-type detectors minimises this effect because, as the majority of interactions will occur at the outside of the detecting volume, the holes will have less material to traverse (Section 2.4 discusses the mobility of charge carriers).

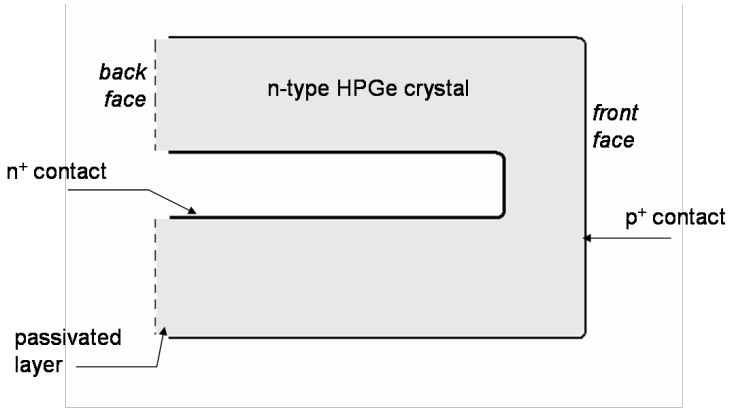

Figure 2.3: N-type HPGe closed-ended coaxial detector configuration

Segmentation of the volume into smaller detecting elements is provided by creating, instead of 1, a number of electrically independent cathodes over the outer surface of the cylinder. The spacing between the contacts will be of the order of $\sim$100 μm and they are produced using photolithographic processes. The requirements for detector segmentation are described in Section 2.6. Due to the shape of these detectors it is customary to segment them in cylindrical polar co-ordinates into rings and sectors. Section 3.2.1 describes the specific details of the AGATA detectors analysed in this work.

2.3.4 Electric Field Calculation

Assuming a truly coaxial geometry to be a good approximation to the detector under consideration, Equation 2.8 in cylindrical polar coordinates can be written as a function of radius, r,

$$\frac{\mathrm{d}^2\phi}{\mathrm{d}r^2} + \frac{1}{r}\frac{\mathrm{d}\phi}{\mathrm{d}r} = -\frac{\rho}{\epsilon} \tag{2.11}$$

where ϕ represents the electric potential between the contacts, ρ is the density of space charge and ϵ is the permittivity of the medium. Upon solution of this equation with substitution of Equation 2.9 and setting the potential difference to the applied voltage, V, the electric field is found to be,

$$-\mathcal{E}(r) = -\frac{\rho}{2\epsilon}r + \frac{V + (\rho/4\epsilon)(r_2^2 - r_1^2)}{r\ln(r_2/r_1)} \tag{2.12}$$

where r_1 and r_2 are the inner and outer radii of the coaxial detector. Following directly from this, the voltage required to fully deplete the detector, V_d, is calculated by setting $\mathcal{E}(r_1)=0$, resulting in the following formula,

$$V_d = \frac{\rho}{2\epsilon}\left[r_1^2 \ln\left(\frac{r_2}{r_1}\right) - \frac{1}{2}(r_2^2 - r_1^2)\right] \tag{2.13}$$

These formulae are applied to the detectors of interest to this work in Section 4.1.

2.4 Signal Generation

The free electron, generated by one of the interaction mechanisms discussed in Section 2.1 will migrate toward the positive potential of the n^+ central contact (anode). The concept of a *hole* is used to represent the vacancy left behind by the creation of a free electron. Neighbouring electrons will preferentially fill this vacancy as they are also drawn to the positive potential, generating a hole migration toward the negative potential of the p^+ contact (cathode).

2.4.1 Charge Carrier Production

The free electron will lose its kinetic energy within the volume of the detector as it is drawn towards the electric contact. This will occur either by impact ionisation, or radiation emission, for example Bremsstrahlung

$$\left(\frac{\mathrm{d}E}{\mathrm{d}x}\right)_{tot} = \left(\frac{\mathrm{d}E}{\mathrm{d}x}\right)_{ion} + \left(\frac{\mathrm{d}E}{\mathrm{d}x}\right)_{rad}. \tag{2.14}$$

In this situation, Bremsstrahlung photons are of small energy (to the order of ∼10 keV) and will ultimately result in photoelectric absorption in close proximity to their creation. The dominant process for the energy range of interest is impact ionisation. This results in the creation of mobile charge pairs which drift toward the respective contacts. The ionisation energy loss per unit path length is given by the Bethe-Block formula. Application of this formula to electrons in germanium can be seen in Figure 2.4 which also shows the energy loss due to radiative processes.

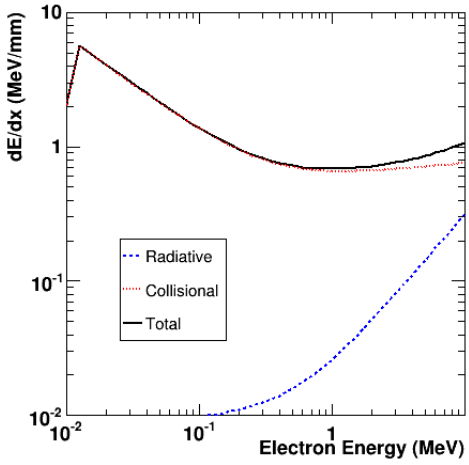

Figure 2.4: Energy loss per unit path length of electrons in Ge. The plot shows the result of the two contributory processes as well as their sum. The data is taken from [NI08a].

The average energy required to create an electron-hole pair has been found experimentally to be independent of the energy deposited, E, implying that it is the number

of these charge pairs produced, N_p, that is indicative of the incoming energy:

$$N_p = \frac{E}{\epsilon} \tag{2.15}$$

where ϵ is the average energy required to create an electron-hole pair, also termed the ionisation energy. This ionisation energy is small ($\sim$3 eV for Ge at 77 K) compared with the energy deposited. Statistical fluctuations in N, caused by the charge carriers dissipating a fraction of their energy to lattice vibrations, will therefore be small compared to the total number per γ-ray interaction. It is this fact which is responsible for the superior energy resolution of semiconductors over other radiation detectors.

Because the presence of an electron-hole pair affects the probability of subsequent pair generation, the fluctuations in the total number produced cannot be treated by Poisson statistics and the actual variation in charge carriers produced is smaller than that expected by the Poisson model. The Fano factor, F, is determined experimentally to relate the variance with the number of charge carriers produced,

$$\left\langle \Delta N^2 \right\rangle = FN. \tag{2.16}$$

The limit to the resolution (Full Width at Half Maximum) achievable is then given by

$$FWHM = 2.35\sqrt{FE\epsilon}. \tag{2.17}$$

For germanium the Fano factor is found to be approximately 0.1 [Kn00]. This equates to a best achievable energy resolution of $\sim$1.5 keV for a 1332 keV γ-ray.

2.4.2 Charge Collection

The applied electric potential and resulting electric field cause a net migration of the charge carriers. The velocity vector is approximately antiparallel to the field direction in the case of electrons, and in the case of holes, the opposite is true. Furthermore the magnitude of the vector differs between the two charge species. This is due to

the fact that the motion of holes is not a direct process but the result of electron rearrangement as the vacancy left behind by the electron pertaining to the pair is successively filled. At low values of electric field, the velocities of both electrons, v_e, and holes, v_h, increase proportionally to the electric field, $\mathcal{E}$, and can be defined as,

$$v_e = \mu_e \mathcal{E}. \tag{2.18}$$

$$v_h = \mu_h \mathcal{E}. \tag{2.19}$$

In these equations the constant of proportionality is termed the *mobility* of the corresponding charge species. At higher values of the electric field ($\sim 10^4$ V/cm), a saturation velocity for each charge type is reached at $\sim 10^7$ cm/s. This equates to a total charge collection time from the moment of the γ-ray interaction of $\sim$300 ns for a distance of 3 cm to the furthest collecting electrode. Although there will be some transit time between the photon interaction and collection of electrons and holes on their respective electrodes, charge will begin to be *induced* on these electrodes immediately. The pulse therefore begins to rise immediately following the interaction and continues until complete charge collection has occurred.

2.4.3 Anisotropic Drift Velocity

In a cubic crystal at high electric fields, the charge carrier mobilities, and hence their drift velocities, are no longer scalar quantities and therefore the conductivity of the material no longer obeys Ohm's law. The mobility of the charge carriers varies according to temperature and the electric field, despite the apparent simplicity of Equations 2.18 and 2.19. The lattice structure of the crystal affects the charge mobility depending on the orientation of the electric field vector with respect to the lattice planes. Germanium has a Face Centred Cubic (FCC) lattice structure, this arrangement of atoms can be seen in Figure 2.5. Upon definition of Cartesian coordinate axes, Miller indices can be used to denote lattice planes. The (111), (110) and (100) planes are depicted in Figure 2.6. In a cubic lattice, such as crystalline germanium,

the associated lattice vector is normal to the lattice plane and due to the symmetry of the lattice, many directions are considered equivalent. Three principal lattice vectors, [111], [110] and [100], result from the planes depicted in Figure 2.6 and equivalent vectors result from symmetrically equivalent planes. The principal crystallographic directions $\langle 111 \rangle$, $\langle 110 \rangle$ and $\langle 100 \rangle$ are thus constructed.

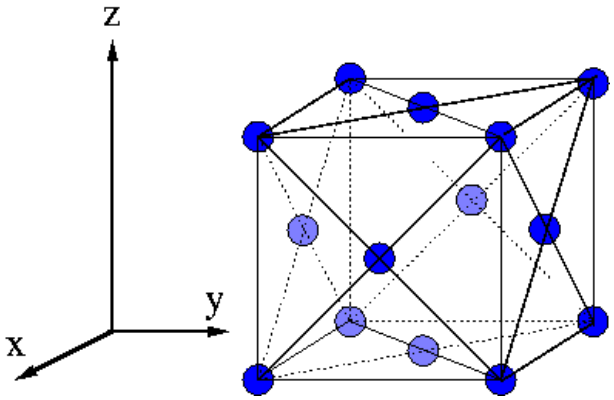

Figure 2.5: The Face Centred Cubic lattice structure of crystalline Germanium.

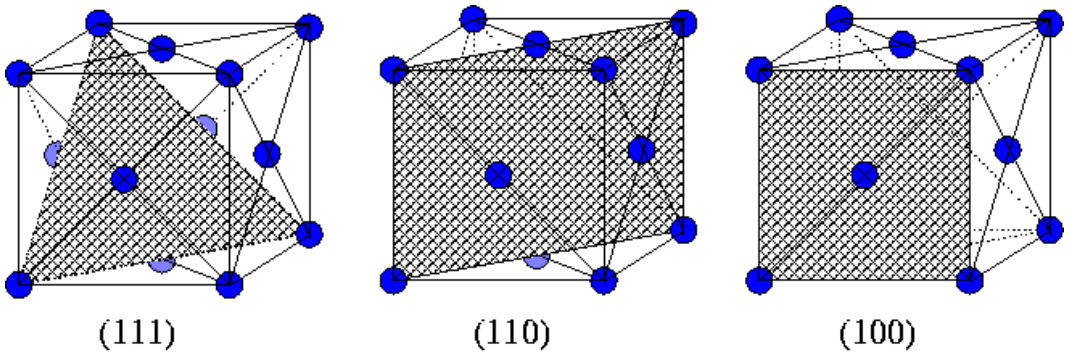

Figure 2.6: The (111), (110) and (100) lattice planes of a Face Centred Cubic crystal.

Quantitative descriptions of the conductivity of Germanium, and hence the velocity of its charge carriers, as a function of its lattice orientation are available in [Mi00b] and [Br06b] and references therein. In qualitative terms, the velocity of charge carriers is greater when the field vector lies along the lattice orientation which contains the

largest density of lattice atoms. Figure 2.7, taken from [Mi00b], and consideration of Figure 2.6 illustrate this. Furthermore, the direction of the velocity vector is only parallel to the electric field when the lattice orientation has rotational symmetry - this is true along the principal crystallographic axes.

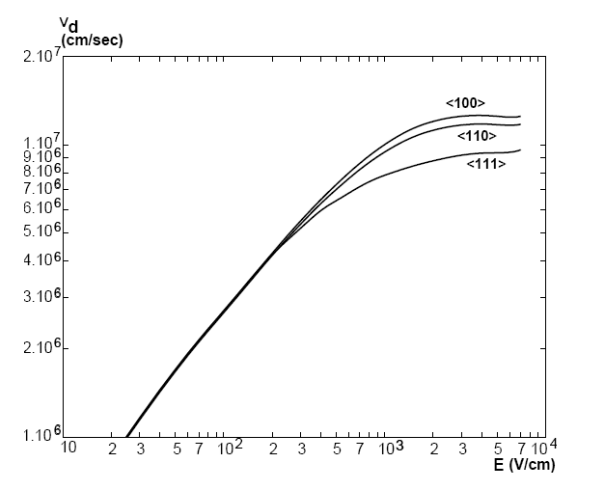

Figure 2.7: Plot taken from [Mi00b]. Drift velocities of electrons in germanium for the three principal crystallographic axes. The $\langle 111 \rangle$ and $\langle 100 \rangle$ curves originate from experimental data in [Ot75] while that of the $\langle 110 \rangle$ direction is from simulated data described in [Mi00b].

2.4.4 Induced Charge

As described in the previous section, the energy deposited by ionising radiation will result in the production of a cloud of charge carriers which drift toward the electrodes. The result of each charge cloud can be considered as the sum of the effects from the individual charge carriers as discussed here.

A charge, q, moving within an electric field, $\mathcal{E}$, will cause a time dependent charge to be induced on nearby electrodes. The instantaneous value of this charge, Q, induced on an electrode surface, S, is given by Gauss's law,

$$Q = \oint_S \epsilon \mathcal{E} \cdot dS \tag{2.20}$$

where ϵ is the dielectric constant of the material. Solution of this equation becomes tedious as it involves recalculation at every point on the charge's trajectory. It can be shown [He01] that Q depends exclusively on the momentary location of q and the geometry of the bounding electrodes, and not on the space charge nor the applied potentials. On this basis, the Shockley-Ramo theorem [Sh38, Ra39] can be devised, which states that the instantaneous induced charge can be found according to,

$$Q = -q\phi_w(x) \tag{2.21}$$

and the instantaneous induced current from,

$$i = qv \cdot \mathcal{E}_w(x) \tag{2.22}$$

where v is the instantaneous velocity of q. The weighting potential, ϕ_w, is introduced as well as the weighting field, $\mathcal{E}_w$. The weighting concept simply provides a relationship between the location of the charge and the configuration of the electrode, and therefore need only be calculated once for each electrode, making this approach computationally advantageous. The weighting potential will be $0 \leq \phi_w \leq 1$, and for a given electrode, j, is given by the Laplacian:

$$\nabla^2\phi_w(x) = 0 \tag{2.23}$$

where $\phi_w|S_j{=}1$ at electrode j, and $\phi_w|S_k{=}0$ at all other electrodes (k=1,2,3...). The details of the method are independently proven in [He01].

A direct observable of Equation 2.21, with the above conditions applied, is that when the charge, q, reaches the electrode toward which it is traveling, j, the net charge it has induced on that electrode will be equal to -q and the net charge induced on the remaining electrodes will be zero. This leads directly to the concept of transient charges, also termed image charges, in which there is a momentary charge induced during the transit time of q but the net charge on electrode k after collection on electrode j is 0. Due to the strong spatial dependence of the weighting field, the transient

charges produced are highly indicative of the position of origination of the charge q. Also evident is the fact that electron collecting electrodes (the central anode of the detectors of interest) will produce a positive charge signal while the hole collecting contacts (outer cathodes) pulse will be negative.

An important feature of the weighting potential is its rapid decrease with distance from the sensing electrode. This implies that the charge species moving away from the electrode will have little contribution to the induced signal. It should also be noted that for a set of k electrodes, the total charge induced:

$$Q(t) = \sum_k Q_k(t) = 0 \tag{2.24}$$

implying that the electrodes collecting opposite charge species will collect equal and opposite charge signals [Br06a]. Applied to segmented coaxial detectors; the core charge pulse will be equal and opposite to the sum of the segment pulses.

2.5 Signal Processing

Collection of charge carriers at an electric contact creates a small pulse which must be delivered to the signal processing chain for analysis. Due to the size of the signal and the fact that electronic noise will be produced in the subsequent components of the chain, amplification and shaping of this signal is required. Moreover, it is important that minimal noise has been induced before the initial amplification because it will be enlarged along with the signal. For this reason a *preamplifier* is used as close to the detector as possible.

2.5.1 The Preamplifier

The main function of the preamplifier is to create an output voltage signal which is amplified proportional to the input. Semiconductor detectors generally utilise preamplifiers that are charge sensitive, as opposed to voltage sensitive, as the proportionality

of the former is invariant to changes in input capacitance (which can differ according to the detector's operational parameters). A Field Effect Transistor (FET) forms the basis of an amplifier, the operation of which is not discussed here [Lu00]. The principle of the charge sensitive preamplifier is depicted in Figure 2.8.

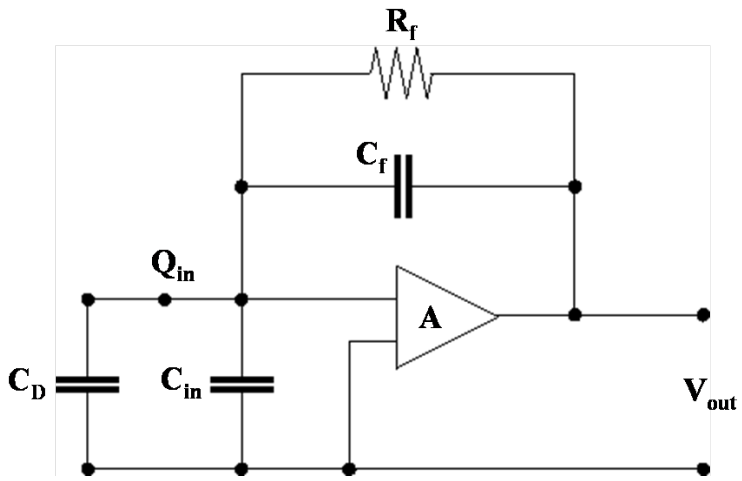

Figure 2.8: Schematic representation the operation of a typical charge sensitive preamplifier.

The signal charge pulse, Q_{in}, is integrated over the contact's output capacitance, C_D, and that of the input circuitry to the amplifier, C_{in}. This small signal is then input to an inverting amplifier with capacitive feedback, C_f, and gain, A. The output signal V_{out} is then given by,

$$V_{out} = -\frac{Q_{in}}{C_f + \frac{C_D + C_{in} + C_f}{A}}. \tag{2.25}$$

For large amplification the second term in the denominator of equation 2.25 approaches zero, implying that Q_{in} is completely transferred to the feedback capacitor and the output signal is proportional to the total integrated charge input to the amplifier. The equation reduces to,

$$V_{out} = -\frac{Q_{in}}{C_f}. \tag{2.26}$$

Figure 2.9 shows the circuit structure of a preamplifier typical to those used in the detectors discussed in this work.

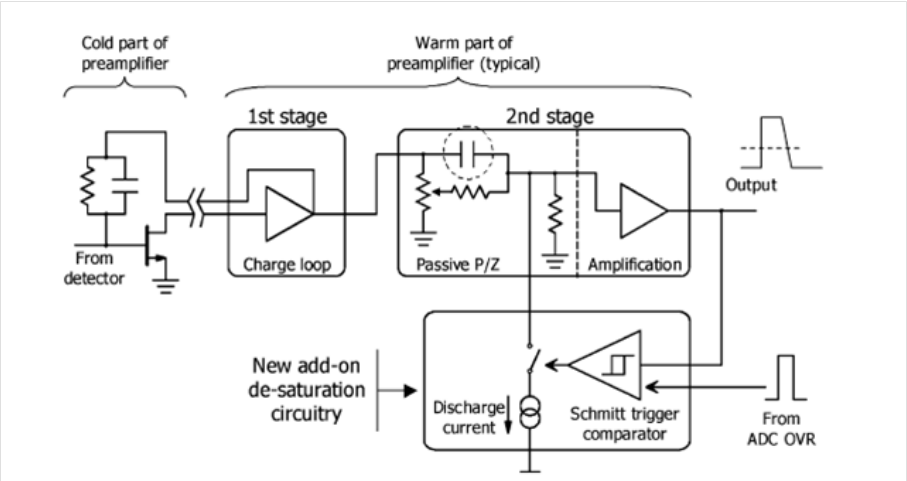

Figure 2.9: A typical charge sensitive preamplifier used for a HPGe detector such as those used in this work. The cold part is located in the cryostat. The reader is referred the citation where this figure was taken [Pu04b] for more information.

The preamplifier preserves the leading edge of the pulse from the detector so that its shape is consistent with the charge collection as seen by the contacts. After complete charge collection, the pulse decays according to the time constant given by the feedback capacitance and resistance ($\tau = R_f C_f$). The preamplifier also serves as an impedance matcher, minimising input loading from the detector to promote successful propagation. The bandwidth of a preamplifier limits the signal frequencies which it can process. A typical bandwidth for the preamplifiers such as these is $\sim$10 MHz.

As stated earlier, electronic noise generated pre-amplification is of great consequence to the signal and for this reason much emphasis is placed on the Equivalent Noise Charge (ENC). This is defined as the the amount of charge that would be necessary at a preamplifier's input terminals to generate an output voltage equal to the RMS noise value. In a charge sensitive preamplifier, the output voltage is fed-back to the input terminals and the noise generated internally to the amplifier is therefore also

significant when considering the ENC. The equivalent input noise charge is given by,

$$Q_{in} = v_{in}(C_f + C_D + C_{in}) \tag{2.27}$$

where v_{in} is the input noise voltage and the other symbols are as detailed in Figure 2.8. Evidently the value of a preamplifier's ENC is highly dependent on the capacitance of its input circuitry, its feedback and that of the detector itself.

2.5.2 Electronic Noise

Any components of an electronic circuit will be subject to electronic noise caused by thermal excitation of electrons. This type of noise is often referred to as Johnson noise. Thermal noise is a source of *white* noise as, due to its stochastic nature, it contains all frequencies. To keep the white noise to a minimum before amplification, there are advantages in housing the FET within the low temperature environment of the cryostat. The spectral power density, $\mathrm{d}P/\mathrm{d}f$, of thermal noise is given by thermodynamic consideration [Ko96],

$$\frac{\mathrm{d}P_n}{\mathrm{d}f} = 4kT \tag{2.28}$$

where P is the total power, f is the frequency, T is the absolute temperature and k is the Boltzmann constant. The spectral density of white noise is inherently constant.

Shot noise is the term given to represent the statistical fluctuations in the number, N, of individual charges, q, which comprise the total charge, Q. Shot noise is also a white noise source. It is only important in non-Ohmic conductors where charge carriers are limited, as is the case in components of the FET. Shot noise (as well as thermal noise) can also be generated in the detector itself and can be considered as the thermodynamic minimum of its output. The spectral density of the shot noise current is given by [Ko96],

$$\frac{\mathrm{d}I_n^2}{\mathrm{d}f} = 2qI \tag{2.29}$$

Semiconducting electronic components also suffer from noise due to crystal defects which cause trapping of charge carriers. These trapping sites generally release the charge after a short time. Several trapping sites with differing characteristic release lifetimes yield an approximate *1/f* dependence on the spectral power density [Ko96],

$$\frac{\mathrm{d}P_n}{\mathrm{d}f} = \frac{1}{f^\alpha} \tag{2.30}$$

In this equation α can vary between 0.5 and 2. This type of noise is often referred to as Low Frequency or *1/f* Noise.

2.5.3 Signal Manipulation

In general there are two types of signal propagation, differential and single-ended. A preamplifier is configured for one type of signaling. Single-ended signaling is the more common and consists of a single wire transmitting the signal. Differential signaling involves the use of two wires of equal impedance known as balanced lines. The two lines transmit the same signal with one inverted with respect to the other. The receiver reads the difference between the two signals, as opposed to the difference with respect to ground, giving twice the noise immunity of a single-ended system. An increased tolerance to ground offsets between devices is also gained.

Traditional analogue electronics utilise many subsequent components in the signal processing chain for the purposes of further amplification, pulse height and timing measurements [Kn00]. However, digital synthesis of detector signals is increasingly commonplace in order to extract this information and also infer the location of the photon interaction sites. This is achievable due to the strong dependence of signal shapes on the path of the charge carriers through the sensitive detecting volume as described in Section 2.4.

2.6 Spectrometer Design and Functionality

Current techniques in experimental nuclear physics involve the bombardment of a target nucleus with a beam of accelerated stable or, more recently, radioactive ions. There are a number of reactions which can occur between the two constituents resulting in the production of the nucleus of interest. This nucleus can be populated with high recoil velocity and at extremes of angular momentum, energy and isospin. The cross sections for such reactions can be low and the γ-rays of interest are often amidst a high level of background radiation. It should be noted that radioactive ion beams, used to produce more exotic nuclei, will inherently have low intensity. The highly excited nucleus will decay via the emission of cascades of γ-rays. Isolation of these photons from the large amount of background radiation produced in the reaction is facilitated by the selection of time-correlated photons originating from the same cascade. The angle of emission, energy, multi-polarity, intensity and timing of the photons are all indicative of the nuclear structure. There are therefore a number of factors which can contribute to the efficacy of a γ-ray spectrometer. The pertinent issues are highlighted below, although there are others, such as timing resolution, not discussed here.

2.6.1 Energy Resolution

The importance of good spectral energy resolution is clear, particularly when photons of many differing energies are expected and reaction cross sections are low. The intrinsic spectral energy resolution achievable with a semiconductor detector can be expressed as a function of its contributory factors:

$$\Delta E_i^2 = \Delta E_s^2 + \Delta E_c^2 + \Delta E_n^2. \tag{2.31}$$

In this equation, ΔE_s represents the peak width that would be observed solely due to the statistical spread in the total number of charge carriers produced, as described in Section 2.4.1. The second term, ΔE_c, is the spread in energies pertaining to incomplete

charge collection. This can occur due to defects or residual impurities in the crystal lattice structure, creating trapping sites or recombination centres, and is amplified in large volume or low electric field detectors. Incomplete charge collection manifests as a low energy tail on the spectral peaks.

Broadening of the peaks due to all components of electronic noise is responsible for the third term, ΔE_n. These will be attributed to either the detector (surface leakage, bulk leakage or Johnson noise from electrical contacts) or the electronic components in the pulse processing circuitry following the detector (as described in Section 2.5.2). These elements combine in quadrature in a similar fashion to the above equation to give the total electronic noise component, ΔE_n.

However in the context of nuclear structure experimental conditions, the following expression applies,

$$\Delta E^2 = \Delta E_i^2 + \Delta E_D^2. \tag{2.32}$$

The final term in the above equation, ΔE_D, is the broadening of spectral peaks due to Doppler shifting of the γ-ray energy and is therefore only relevant when the radiation source is moving at a significant fraction of the speed of light. As this is frequently the case in nuclear structure experiments, this is a significant problem and is often the major cause of peak broadening and hence poor energy resolution. This is therefore considered in more detail in Section 2.6.5.

2.6.2 Granularity

The nuclei produced during in-beam experiments can have angular momenta up to $\sim$90 $\hbar$ (for compound nucleus reactions) while the emitted γ-rays each carry only a few units of $\hbar$. Evidently, cascades of many γ-rays can be expected and, in order to avoid summing their energies, it is necessary to be able to detect each one individually. It is therefore desirable to have a large number of detecting elements in comparison

with the total number of γ-rays anticipated from an event in order to keep the single hit probability high. For this reason the most powerful current spectrometer systems consist of a large number of HPGe detectors, such as Gammasphere [De88] containing $\sim$110. Granularity of a spectrometer can also be improved by the fairly new concept of electrically segmenting the individual detectors, this process is described in Section 2.3.3. Some of the Gammasphere detectors are segmented 2-fold while the EXOGAM array makes use of 64 individual HPGe crystals each with 4-fold segmentation [Si00]. The TIGRESS spectrometer, when completed, will consist of 48, 8-fold crystals [Sc05b]. Granulation is also required for determination of interaction location within the volume of a detector; this is discussed in more detail in Section 3.4.

2.6.3 Detection Efficiency

The absolute efficiency of an array of N individual detectors is defined as,

$$\varepsilon_{abs} = \frac{N\Omega}{4\pi}\varepsilon_{int} \tag{2.33}$$

where Ω is the solid angle subtended by each detector as seen from the source position. ε_{int} represents the intrinsic efficiency of each individual detector and is proportional to, amongst other things, its volume. However, it is the fraction of events which fall into the photopeak that are of interest and so the photopeak efficiency, ε_{ph} is introduced,

$$\varepsilon_{ph} = \frac{P}{T}\varepsilon_{abs} \tag{2.34}$$

where P/T is the ratio of the photopeak counts to the total number detected, termed the peak-to-total ratio. For an array of N individual detectors of identical intrinsic efficiency, the spectrometer's total photopeak efficiency is given by,

$$\varepsilon_T = \frac{1}{4\pi}\sum_N \frac{P}{T}\Omega\varepsilon_{int}. \tag{2.35}$$

It can be seen in Figure 2.1 that Compton scattering is the dominant interaction process of γ-rays for a large portion of the energy range of interest. As described in

Section 2.1.2 photons which scatter out of a detecting element add to the spectral background and not to the photopeak, decreasing the peak-to-total ratio. This has lead to the development of Compton Suppression Shields (CSS) [No94, Be96] which have increased peak-to-total ratios from ∼20 % to ∼50 %. The shields are generally high density scintillation detectors, such as BGO, which surround each HPGe detector and operate in anti-coincidence with it to veto those events which would otherwise add to the Compton continuum. More recently, composite HPGe detectors have been produced. In this configuration, a number of individual detectors are close-packed in the same cryostat. Encapsulation of the individual detectors enables them to be handled without causing damage to the sensitive crystals. Both the EXOGAM and TIGRESS arrays pack 4 HPGe crystals into a common cryostat. The instantaneous energies resulting from a Compton scattered photon between the detecting elements can be summed in order to improve the peak-to-total ratio of the array.

2.6.4 Resolving Power

The resolving power of a detector for a cascade of evenly spaced photons (usually resulting from depopulating high spin states of a rotational band) is given by [No94],

$$R = \frac{S_\gamma}{\Delta E}\frac{P}{T}. \tag{2.36}$$

In this equation S_γ quantifies the average energy separation between peaks in a spectrum, P/T is the peak-to-total ratio and ΔE is the FWHM of the photopeak. The ability of a spectrometer to resolve a cascade of γ-rays above a high level of background is fundamentally important to modern nuclear physics experiments. A spectrometer's resolving power for multiple fold, and hence multi-dimensional, spectra is therefore introduced [De88]. If a fold, f, of γ-rays are detected from a cascade with intensity α, the detection sensitivity increases as αR^f. The statistics are also improved according to

$$n = \alpha N_0 \varepsilon_T^f \tag{2.37}$$

where n is the number of photopeak counts in an f-fold coincidence spectrum, N_0 is the total number of these events produced in the experiment and ε_T is the array's total photopeak efficiency for the energy of interest. An optimal fold, F, can be derived for the weakest branch resolvable, whereby the photopeak is just visible above the background. In this case

$$\alpha R^F = 1 \tag{2.38}$$

and the resolving power of the spectrometer, RP, is found by substitution

$$RP = R^F = \exp\left(\frac{\ln(N_0/n)}{1 - \ln\varepsilon/\ln R}\right). \tag{2.39}$$

It is apparent that the important parameters in resolving a sequence of γ-rays are the energy resolution of the detectors, their peak-to-total ratios and the total photopeak efficiency of the spectrometer.

2.6.5 Doppler Broadening

The factors contributing to the energy resolution of a single detector are discussed in Section 2.6.1 where Doppler broadening is introduced. The shifted γ-ray energy due to the velocity of its source, in this case a recoiling nucleus, is given by,

$$E_\gamma = E_{\gamma 0}\left(\frac{\sqrt{1-\beta^2}}{1-\beta\cos\theta_\gamma}\right) \approx E_{\gamma 0}\left(1+\beta\cos\theta\right) \tag{2.40}$$

where $E_{\gamma 0}$ is the unshifted energy, $\beta = v/c$ and is the ratio of the nucleus' velocity to the speed of light, and θ_γ is the photon's angle of emission from the path of the recoiling nucleus. The spread in energies due to this shifting is given by the differential of Equation 2.40 with respect to the variables θ and v, and is referred to as Doppler broadening of the spectral peaks.

$$\Delta E_\gamma \approx E_{\gamma 0}\cos\theta\frac{\Delta v}{c} - E_{\gamma 0}\frac{v}{c}\sin\theta\Delta\theta \tag{2.41}$$

Uncertainty in the recoil velocity, Δv, results from;

1. Spread in the kinetic energy of the beam particles due to straggling within the target before the reaction has taken place. This will depend on the target thickness as well as its exact composition which dictate the likely location of the reaction within the target.

2. Energy lost by the recoiling nucleus before it leaves the target material. This uncertainty suffers from the same quantification difficulties as the previous point.

3. Conservation of momentum dictates that the velocity of the recoil will depend on its trajectory following the reaction. It is usual for the recoil to have an associated cone of kinematically allowed angles from the primary (beam) axis resulting in a spread of its velocities.

The spread in recoil velocity is discussed in more detail in Section 6.3.

The uncertainty in the angle of photon emission from the recoil, $\Delta\theta$, results from;

1. The angular range of the recoil itself as discussed above.

2. Uncertainty in the photon angle due to the finite size of its detecting element.

Practically the latter is large in comparison to the spread due to the cone of the recoiling nucleus and until the advent of Pulse Shape Analysis (PSA) could only be compensated for by decreasing the size of the detecting volume. Figure 2.6.5 shows the contribution to the FWHM of spectral peaks due to the Doppler shifting of the photon energy associated with the finite size of the detecting element.

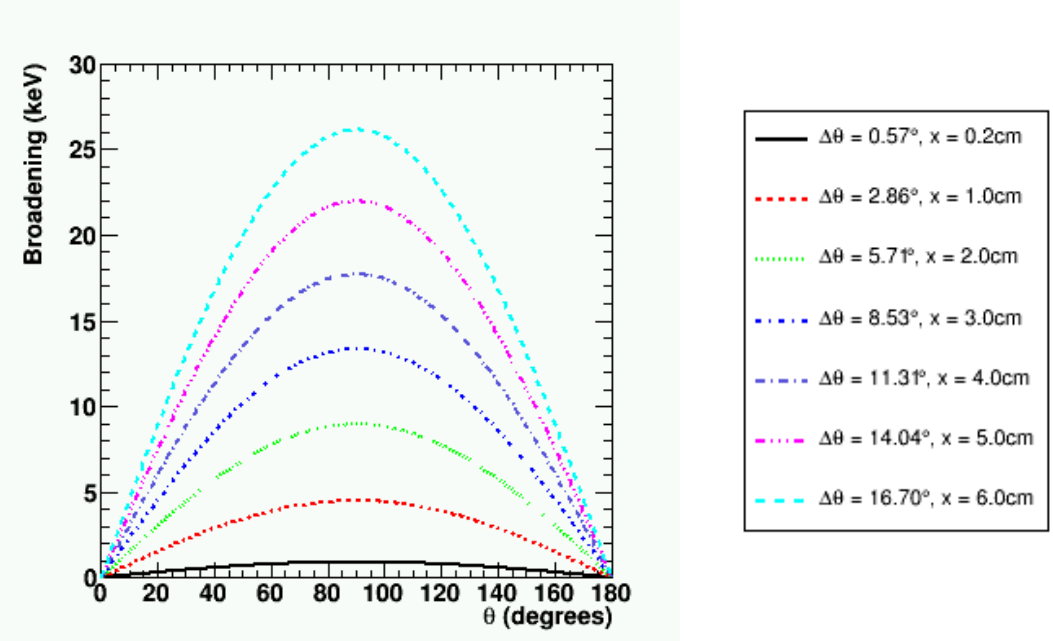

Figure 2.10: Doppler broadening of spectral peaks as a function of γ-ray emission angle. $\Delta\theta$ corresponds to the uncertainty in the angle of detection (half of the detecting element's opening angle) at a distance of 10 cm from the γ source. x is the associated size of the detecting element at its front face. In this plot the spread in recoil velocities was considered negligible, β was taken as 6.5 % and the initial γ-ray energy was taken to be 1.38 MeV. (This energy was chosen so that the results of this calculation are comparable to experimental data discussed in Chapter 6.)

Chapter 3

The AGATA Spectrometer

3.1 The AGATA Array

The ultimate realization of the Advanced GAmma Tracking Array (AGATA) will be a spherical shell comprised almost completely of HPGe material creating the most efficient high resolution γ-ray spectrometer in the world [Ge01]. The AGATA collaboration [AG03] is responsible for its design and construction. It will consist of 180 close packed hexagonal detectors,[1] each with 36-fold segmentation. This number of detecting elements is optimum in keeping the single hit probability high in comparison to the multiplicity of γ-rays anticipated. The detectors are arranged such that their front faces geodesically tile the surface of a sphere with the target position at its centre. This arrangement can be seen in Figure 3.1. The full solid angle coverage of Ge will be minimally compromised by the presence of the indispensable encapsulation of each detector and the cryostats which hold them. There will be 3 close packed hexagonal detectors per triple cluster cryostat creating 60 modular triple units. Section 3.2 describes the detector details further.

[1] A 120 detector configuration was also considered, however, the solid angle coverage and total photopeak efficiency are significantly greater in the 180 detector configuration [Ro04]. Additionally, the larger version leaves more space at the centre of the array for ancillary particle detectors.

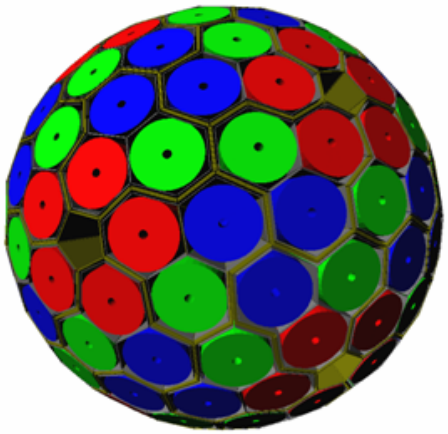

Figure 3.1: Conceptual drawing of the completed array configuration. The three colours represent the three irregular hexagonal geometries.

The solid angle coverage expected with AGATA is ∼80 % providing a total photopeak efficiency at 1MeV of ∼50 % for multiplcity M_γ=1 events and ∼25 % for M_γ=30 [Ge01]. Multipicities greater than 1 require γ-ray tracking (described in Section 3.3) to be implemented and their corresponding efficiencies are therefore currently based on simulation. The predecessors to AGATA currently achieve P/T ratios of ∼50 % and photopeak efficiencies of ∼20 % for M_γ=1 and ∼6 % for M_γ=30, 1 MeV γ-rays. The resolving power of the AGATA array is expected to be several orders of magnitude (∼3) above current spectrometer systems.

3.2 The AGATA Detectors

There will be three types of hexagonal AGATA detectors used in the completed array, 60 of each, and they will differ only by their geometries; the front face of each type will be a slightly differing asymmetric hexagon. This is merely to aid the tessellation of the detectors. One of each of the 3 differing hexagonal geometries will be placed in each triple cluster cryostat.

The fundamental concept of an AGATA detector is a closed ended coaxial n-type HPGe crystal which is hexaconical in shape; that is, each detector has a hexagonal front face which tapers backwards to form a cylindrical rear. Figures 3.2 and 3.3 depict this geometry. Each detector is cut from a cylinder of crystalline HPGe with a diameter of 8 cm and length of 9 cm. Six tapered faces are cut from the rounded surface of the cylinder in order to form a hexagonal front face. A 1 cm diameter bore hole is drilled from the back surface along the axis of the cylinder to a distance of 1.3 cm from the front face. The detectors are fabricated from n-type HPGe and their purity is discussed in Section 4.1.2. The inner contact is the n^+ material, believed to be lithium and created by diffusion, while the outer p^+ contact is believed to be implanted boron. The outer contact is electrically segmented; azimuthally into 6 equal sectors of 60°, and vertically into 6 rings of unequal depth. The segment depths can be seen in Figure 3.4 for the prototype detectors.

The detectors are produced by Canberra Eurisys, Lingolsheim [Can] and their cryostats are manufactured by Cryostat and Detector Technique Thomas [CTT]. Each detector has 37 charge sensitive preamplifiers (36 segments plus the core channel). Each preamplifier has a cold part which includes the FET, as well a warm section mounted outside the cryostat. There are 7 LVDS digital video cable outputs from each detector to convey the differential signals from the preamplifiers, 1 of which carries the anode signal, and each of the other 6 cables carries the 6 segment signals from a sector.

3.2.1 Symmetric Prototypes

Three prototype detectors have been constructed, each with a symmetric front face, the dimensions of which can be seen in Figures 3.4 and 3.5. Their geometries are identical, within specifications, and they are labelled S001, S002 and S003. Each Ge crystal is encapsulated in aluminium and then placed in its own single cryostat for testing. A photograph of the test cryostat is included in Figure 3.6.

Figure 3.2: Ge crystal before segmentation and encapsulation.

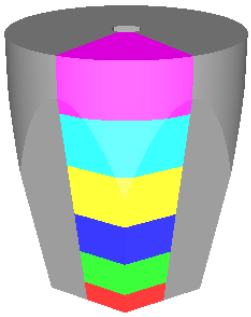

Figure 3.3: Three dimensional illustration of a single AGATA detector showing some segmentation.

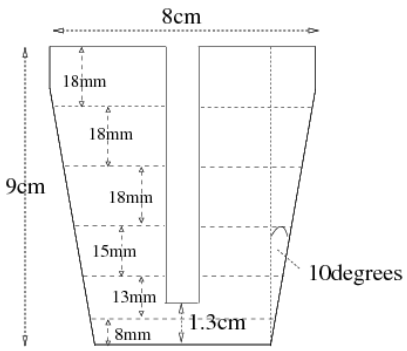

Figure 3.4: Cross sectional schematic of the prototype germanium crystal showing the horizontal segmentation and the bore hole.

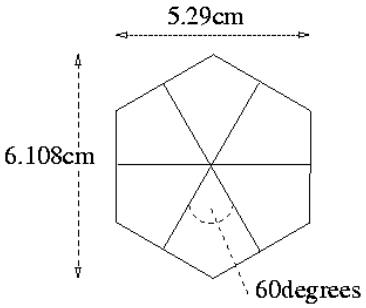

Figure 3.5: Dimensions of the front face of the symmetric prototype detectors showing the vertical segmentation.

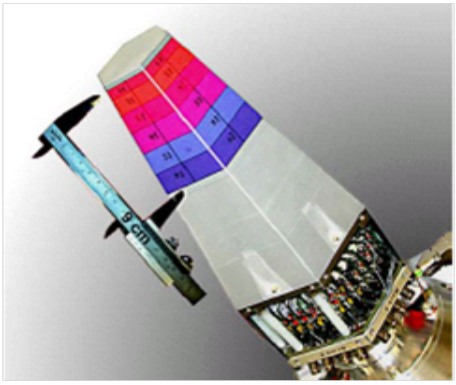

Figure 3.6: Prototype test cryostat.

3.3 Gamma-Ray Tracking

The solid angle coverage of HPGe in AGATA is improved by a factor of ∼2, compared to the previous generation of spectrometers, by the elimination of Compton suppressors. This is clearly advantageous to detection efficiency. Furthermore, the granularity achieved by segmentation of the detectors will allow a cascade of simultaneous γ-rays to be detected independently. However the photopeak efficiency, discussed in detail in Section 2.6.3, will still be limited by the partial energy deposition of Compton scattered photons. In order to reconstruct the full energy event from the scattered photon interaction sites, and thus increase the peak-to-total ratio of the spectrometer, the scattered photons must be disentangled from the multiplicity of photons from the cascade. This is achieved by the application of tracking algorithms which incorporate the physical photon interaction possibilities, as discussed in Section 2.1, in order to determine the most likely nature and sequence of interactions. The time resolution of HPGe (∼5 ns) does not allow the temporal ordering of the sequence to be measured and it is therefore necessary to use the Compton scattering formula (Eq. 2.5) to calculate the scattering angle, θ, based on the deposited energy. A figure of merit can then be devised between this calculated angle, θ_c, and the measured angle, θ_m, derived from the knowledge of the interaction coordinates, for all

possible permutations of the sequence, according to [Le03]

$$\chi_j^2 = \sum_{n=1}^{N-1} \left(\frac{\theta_m - \theta_c}{\sigma_\theta} \right)_n^2 . \tag{3.1}$$

This equation assumes N interaction sites (the final of which is absorption), $j(=N!)$ possible permutations of the sequence and σ_θ is the estimated angle uncertainty. It is then possible to determine the permutation with the least χ^2 value. The method is limited by the energy and spatial resolutions of the spectrometer which cause uncertainty in θ_c and θ_m respectively.

There are currently 2 prominent approaches to Gamma-Ray Tracking (GRT); the clusterisation method [Sc99] and the backtracking method [Mi04]. In the backtracking process, the most likely final interaction point is determined first and the preceding scatters are determined in reverse order. The clusterisation method groups likely scatter events into clusters and compares each possible sequence of interactions against the Compton equation as outlined above. There are merits to both approaches and it is likely that the ultimately adopted GRT method will be a combination of the two.

3.4 Pulse Shape Analysis

Pulse Shape Analysis (PSA) is expected to provide the necessary spatial information as input to GRT algorithms. It makes use of the differences in signal shapes observed as a result of photon interactions from different spatial locations within a detecting volume. These differences can be attributed to one of two specific characteristics of semiconductor radiation detection, both of which are caused by the motion of the charge clouds through the detector (See Section 2.4.1). The first characteristic is the amount of charge *induced* at the electrodes of segments containing the interaction (hit-segments) and their neighbouring segments, as the charge clouds migrate toward their collecting electrodes. It should be noted that it is the amount of charge *collected* at the electrodes of hit segments that is indicative of the incoming photon energy, not the

charge induced (which is a function of the detector geometry and the path of the charge cloud exclusively). Section 2.4.4 describes this in more detail. The second characteristic is the *time* the charge clouds take to drift toward their collecting electrodes, termed the *risetime* of the charge pulse, as discussed in Section 2.4.2. Both of these attributes are highly dependent on the location of the photon interaction and are discussed in detail in Chapter 5. Multiple hits per segment as well as multiple segment fold cause complications in that the charge contributions of each interaction will be convoluted and separation of the contributions to the pulse is necessary before meaningful spatial information can be retrieved.

Figure 3.7 shows the pulses obtained in the hit and surrounding segments for three different interaction sites within an AGATA detecting element. Section 4.2.2 describes the process by which the pulses are digitised. The spatial dependance of the pulse shapes is evident in the figure.

It can be seen that the pulses originating from an interaction at the outer edge of the crystal (the black pulses) begin to respond more quickly than the other interactions. This is particularly evident in the hit-segment containing the real charge pulse; the black pulse begins to rise faster than the others by approximately 6 samples. Using the sample time described in Section 4.2.2, this equates to 74 ns between the start times of the black pulse and the others. It could be considered that the faster response from the "black" interaction is due to the shorter time taken for the charge carriers to reach this electrode due to their close proximity. However, Section 2.4 discusses the charge collection process and states that charge begins to be induced instantaneously follwing a photon interaction and therefore the time at which the pulse begins to rise, termed t_0, should not depend directly on the location of the interaction. It is likely that the "black" pulses' apparently faster response can be explained by the fact that the pulses are all collected relative in time to the trigger point on the central contact ($\sim$420 keV). The difference in the central contact's pulse shape at $\sim$420 keV between

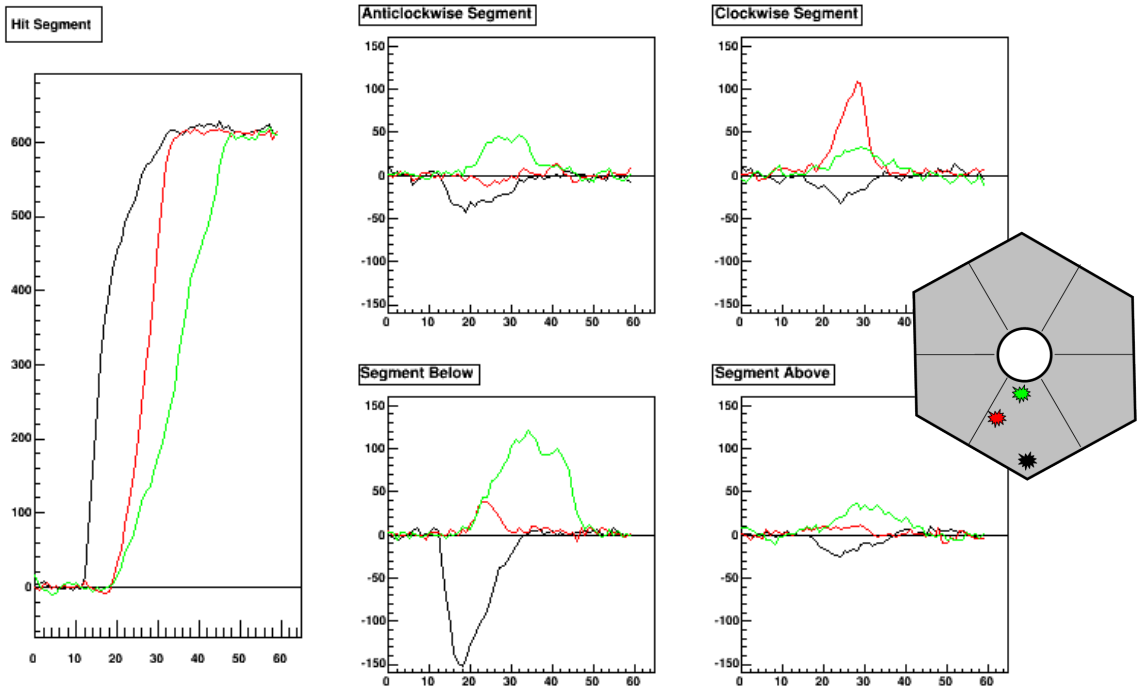

Figure 3.7: Pulses obtained from the hit segment and its neighbours for various photon interaction locations within a segment. The y-axis has units of keV and the x-axis denotes the pulse sample number. The dependence on azimuthal position is visible from the relative sizes of the transient (image) charges induced in segments either side of the segment containing the interaction. The same principle can be applied to obtain depth information from transients induced in the segments above and below the hit segment. Radial position dependence is inferred from the variation in pulses from the hit segment.

the outer interaction and the others creates a different time window within which the cathode pulses are stored. This interpretation is supported by the difference in the core contact's T60 risetimes (the trigger point is ∼63 % of a 662 keV pulse) between the outer interaction and the other locations evident in Figure 5.16; approximately 70 ns.

3.4.1 Basis Dataset Generation

It is generally accepted that a database of calculated pulse shapes for every spatial coordinate within the detecting volume must be constructed in order that the experimental pulses be fitted to it. The most likely interaction position is inferred from the set of calculated pulse shapes that best fits the real data. In Europe the most widely used software to generate this basis is developed and maintained by personnel at IReS, Strasbourg and is known as MGS (Multi Geometry Simulation) [Me04]. MGS utilises a matrix environment to create a cubic grid based modeling system. Firstly a detector geometry is specified by the user, along with various other parameters, such as the applied voltage and the maximum and minimum impurity concentrations. The Poisson equation (Eq. 2.8) is then solved at discrete grid points using a combination of iterative methods, which converge to a solution for the potential and hence the electric field. The velocities of the charge carriers are then calculated according to mobility models of electrons [Mi00a] and holes [Br06b], and the weighting potential for each electrode is calculated as detailed in Section 2.4.4. It is then possible to calculate the charge pulses expected as a result of a photon interaction at any location within the specified volume.

There are problems inherent to this process, the most significant being the cubic grid upon which the calculations are performed. This results in void space between the grid points as well as difficulties in modeling geometries with sharp edges. Other problems include the necessary assumption that the entire volume of the detector is depleted. A detailed comparison between MGS pulse shapes and data from known

coordinates of AGATA detectors has been performed [Di07] and the problematic areas of the simulation are discussed in more detail.

3.4.2 PSA Algorithms

Simple PSA based on pulse shape parameterisations has been successfully used on the MINIBALL array [Eb01] to improve the Doppler correction of experimental data. These detectors have 6-fold segmentation in azimuthal angle only and no depth segmentation. Localisation of the first (or only) interaction site of a γ-ray in 2 dimensions (r, θ) provides sufficient information; MINIBALL is not used for full GRT. The approach parameterises the *time to steepest slope* of the hit segment's charge pulse to determine the radius of the interaction, and the magnitudes of the induced charges in neighbouring segments to determine the azimuthal angle. The method has significantly improved the spectral resolution from detector level to PSA level by $\sim$56 % [Sc05a], however the true location of the interaction is never calculated in the process, and therefore it is insufficient for tracking algorithms (which would also require the third dimension).

There are $\sim$9 PSA algorithms, at various stages of development, which are intended to be suitable for use with AGATA. Most rely on the use of a basis data set of calculated pulses for a defined set of spatial locations within the detector. It should be noted here that a fundamental prerequisite of methods relying on the comparison between simulated and real pulses is the accurate determination of the point in time where the pulses begin to rise, termed t_0. In the presence of electronic noise, as is always the situation for real pulses, t_0 will have a large uncertainty ($\sim$10 ns). Most algorithms incorporate a time degree of freedom such that the calculated signals be shifted in time according to their best fit to the real pulses. Some PSA algorithms are briefly discussed below.

The Matrix Method

This method solves a linear equation involving a matrix of *all* possible basis signals, the experimental pulses and a vector representing the deposited energy for each basis signal [Ol06]. It invokes a large number of parameters and it is therefore necessary to enlist techniques, such as singular value decomposition. The algorithm attempts to determine the locations of multiple hits per segment and multiple segment fold events. Results of the algorithm on the Liverpool scan data (described in Section 4.2) show that the determined interaction sites tend toward the central regions of segments [Ol07]. This is attributed to the inconsistencies between the basis data (generated by MGS) and the scan data.

Adaptive Grid Search

This method searches the basis data set using, initially, a coarse grid to find the point with minimum χ^2 between the reference and real signals [Ve07]. Upon localisation of this point, a finer grid is defined in the surrounding volume and the search is repeated. The method uses, in addition to the preamplifier signal, the signal derived in the Moving Window Deconvolution algorithm [La04a], which is used by the digitisers to calculate the deposited energy [Ve07].

Recursive Subtraction

At present this method attempts to find the number of interactions per segment and their radial positions using the net current pulse only [Cr07]. It utilises the fact that there is a peak in the current pulse corresponding to each interaction and that this is related to its radial coordinate. A region of interest surrounding the peak is expected to be indicative of the single interaction only and this small window is compared to the basis pulses. The simulated pulse that best fits this window is subtracted from the detector pulse and the method is repeated a number of times corresponding to an expected maximum number of interactions per segment (typically $\sim$2 or 3).

Comparison of Methods

All of the above methods have been tested by their authors with the same in-beam data set obtained using the three prototype AGATA detectors (this experiment is discussed at length is Chapter 6). The improvement to the Doppler correction of the spectral peaks is a measure of the success of the PSA algorithms to localise the photon interaction sites. Using a Monte-Carlo simulation [Fa03] it has been possible to isolate the contribution of position resolution to Doppler broadening [Re07a]. Figure 3.8 shows the results of the simulation as well as the energy resolution achieved with the PSA algorithms outlined above and the corresponding spatial resolution of each.

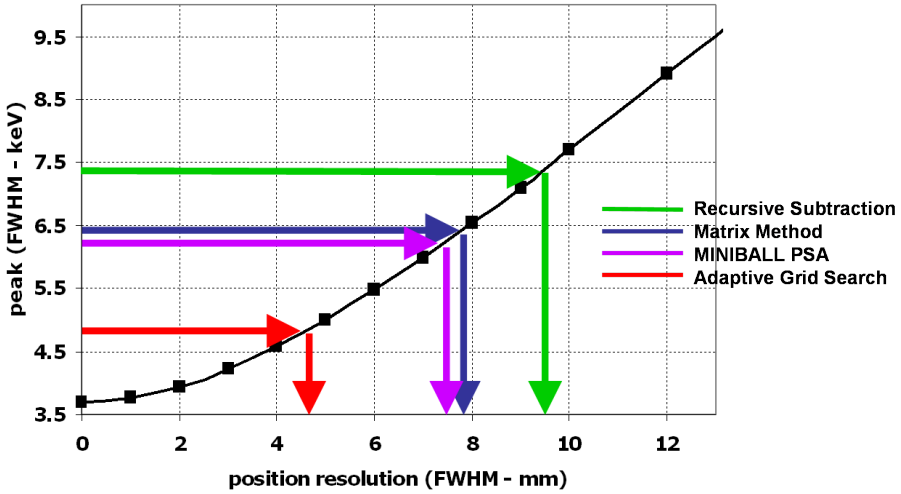

Figure 3.8: Plot taken from [Re07b]. Spectral energy resolution expected as a function of detector spatial resolution showing the achievements of some PSA algorithms.

Chapter 4

Prototype Detector Characterisation

All three of the symmetric prototype AGATA detectors (S001, S002 and S003) have been tested at the University of Liverpool in chronological order. The tests included efficiency and resolution measurements using digital and analogue electronics as well as detailed highly collimated photon scans of the detectors to determine their response as a function of photon interaction position. The scanning procedure and results are discussed in Section 4.2. Results of the S001 detector tests [Ne07] are not included in this work as the quality of the data obtained was poor in comparison to that of the subsequent detectors. This is largely due to two main reasons, the first being the large amount of electronic noise on the signals obtained (caused by a fault with the instrumentation used to convert from differential to single ended signals). The second issue was the scanning procedure adopted for this detector, which was limited by, amongst other things, the strength of the source available [Ne06]. Results from the S002 and S003 detectors only will be discussed in this work.

4.1 Physical and Electrical Details

4.1.1 Labelling Scheme

The geometry and segmentation of the symmetric prototype detectors are discussed in Section 3.2.1. Conventionally the detector segments are labeled alphabetically according to their sector (A-F), and numerically according to their ring (1-6). For example, a segment in sector A at the front face of the detector will be labeled A1 and the segment at the top of this sector is labeled A6. This labelling scheme is depicted in Figure 4.1. To ease graphical display and the construction of algorithms, it is sometimes convenient to label the segments of an AGATA detector numerically only (1-36). When this is the case, the segment index increases logically from front-to-back and sector-to-sector, as detailed in Table 4.1. In this notation it is usual to label the core electrode as the 37^{th} channel.

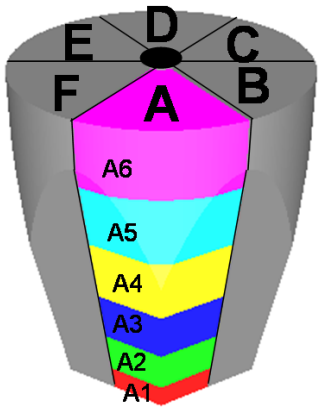

Figure 4.1: Labelling scheme adopted for AGATA detectors. Only the segments in sector A are shown however the same pattern is repeated for all sectors.

	Sector					
Ring	A	B	C	D	E	F
1	1	7	13	19	25	31
2	2	8	14	20	26	32
3	3	9	15	21	27	33
4	4	10	16	22	28	34
5	5	11	17	23	29	35
6	6	12	18	24	30	36

Table 4.1: Alternative numerical segment labelling scheme for AGATA detectors.

4.1.2 Concentration of Impurity Atoms

The most fundamental crystal attribute significant to its detecting functionality is the concentration of impurity atoms in the lattice. This property is defined in the crystal growing process and is not homogeneous within its volume. There is a longitudinal gradient along the axis of rotation (which is also the direction in which the crystal is pulled)[1]. Furthermore, the physical measurement of this value is destructive to the crystal itself and is therefore only measured from the pieces which are cut off to form the desired geometrical shape. In general the crystal manufacturer [Can] measures the impurity concentration at the front and back of the crystal and the gradient is assumed to be linear between these two values. However, for the S003 AGATA prototype, data sheets included impurity concentration measurements for various depths into the crystal, presumed to be measured from the HPGe material removed in the shaping process. Figure 4.2 shows the impurity concentration values quoted by the manufacturers as a function of depth from the front face of the crystal for the three prototype detectors. A linear fit is presumed in all cases and confidence is

[1]There may also be a small rotational gradient in impurity concentration perpendicular to the this axis, perhaps resulting from temperature variations as the crystal is rotated, although this is not quantified by crystal manufacturers and therefore considered negligible.

gained in this presumption by the extra data points for the S003 detector. The reader is advised that the orientation of the values with respect to the crystal geometry is correct to the data sheets, included in Appendices B and C. There has been some confusion over this matter and other sources have been known to claim that the purest part of the crystal is at the front of the detector [Gu05]. Indeed this may be true for other AGATA detectors but is believed not to be the case for the three prototypes.

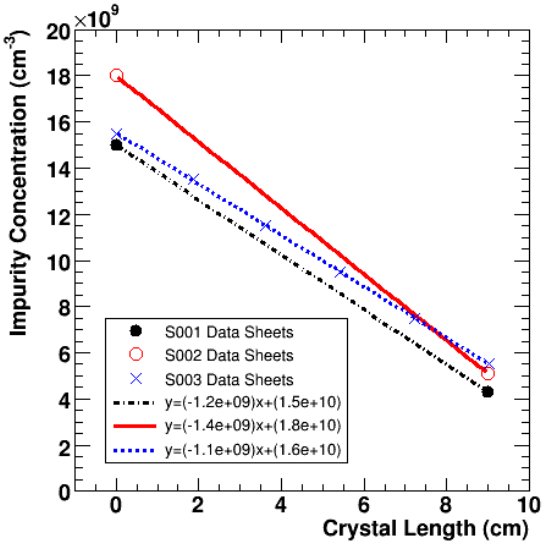

Figure 4.2: Concentration of impurity atoms for each crystal as a function of depth. The front of the crystal is defined as 0 mm while the back surface (from which the bore hole is drilled) is at 90 mm. See the text for a more detailed description.

4.1.3 Impurity Concentration Implications for Crystal Depletion

The operating voltage of the S002 crystal is +5000 V and that of S003 is +4000 V (for completeness, S001 operating voltage is +4000 V). The larger voltage for S002 is required due to its higher concentration of impurities and subsequent higher depletion voltage. This is apparent in Equation 2.13 and is plotted as a function of crystal depth

in Figure 4.3 for each of the three prototype detectors. The reader should remain aware that the equation is valid for truly coaxial detectors and therefore only approximates to the hexaconical crystal shape. Furthermore, the front of the detector in which the axial anode is not present, has less relevance to the equation than the rest of the detector. There is also ambiguity as to which dimension to use for the outer radius of the crystal. There are two radial axes of symmetry, observable in Figure 3.5, creating a maximum and minimum radial distance between the inner and outer contacts which vary with azimuthal angle and also with depth into the crystal due to its taper. As the crystals deplete from the rectifying contact (in the case of AGATA detectors: the outer contact) the regions most affected by prospective incomplete depletion will be close to the inner contact, and the azimuthal variation in radius resulting from the two symmetry axes, will cause small local differences. It is therefore appropriate to use the mean radius of Ge in calculations. This, along with the maximum and minimum values are plotted in Figure 4.4. The physical segmentation boundaries in one dimension which effectively slice the detector into 6 rings are also shown on the plot. It can be noted here that the *effective* segmentation is not necessarily equivalent to the depicted physical segmentation as the former results from the electric field produced by the arrangement of the contacts. In the true coaxial regions of the detector, this is not a significant problem as the field lines point in an approximately radial direction and consequently so do the effective segment boundaries. However, as the central anode extends only part way through the detector, the front regions will not have a radial electric field but one that is warped to follow the complex geometry of the contacts. This is studied for a similar geometry detector in [Go03].

Evident from Figure 4.3 is that, according to the calculation, S001 is operated at a voltage such that it is just depleted in some regions of the crystal. S002, with an operating voltage of +5000 V, is fully depleted throughout its length. The plot implies that S003 is undepleted at depths of between ∼1 cm and ∼6 cm, approximately rings 2 to 5. However, the energy resolutions obtained from the detectors (Section 4.3.1)

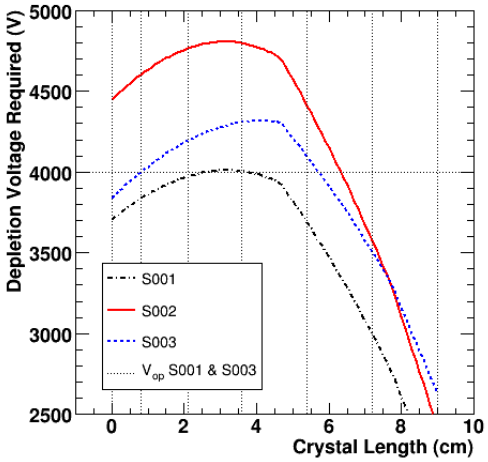

Figure 4.3: The bias voltage required to deplete the AGATA prototype crystals according to Equation 2.13 and using the average outer radius as seen in Figure 4.4.

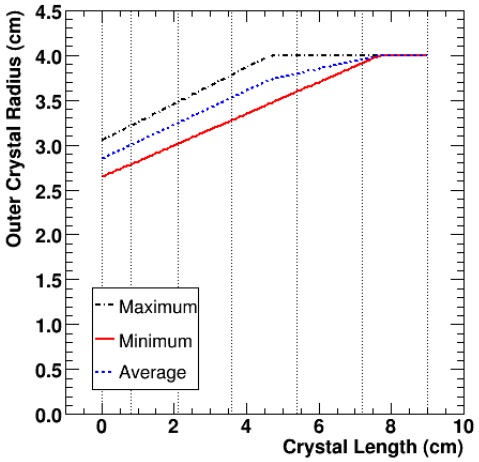

Figure 4.4: Maximum, minimum and average outer crystal radii as a function of depth.

imply that they are fully depleted.

Equation 2.10 enables calculation of the thickness of material depleted according to an applied voltage. It should be noted that this equation is more suited to a planar detector configuration. Application of this equation, using the linear fits from Figure 4.2 for the impurity concentration, yields depletion widths as a function of depth. These values are plotted in Figure 4.5. Furthermore, consideration of the radial distance between contacts can be applied in order to estimate the radial distance of Ge which is undepleted according to this equation. Here, as before the mean outer radius of germanium is used in calculations, this can be seen in Figure 4.4. The difference between the curves in Figures 4.5 and the width of germanium material gives the distance of germanium which is undepleted, according to Equation 2.10, and can be seen in Figure 4.6(a).

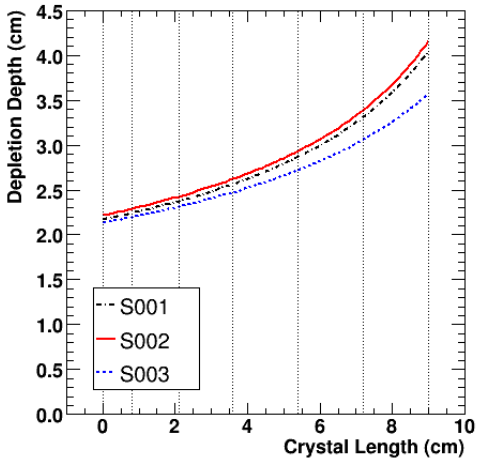

Figure 4.5: Depletion depth expected for the three prototype detectors as a function of crystal length, calculated using equation 2.10.

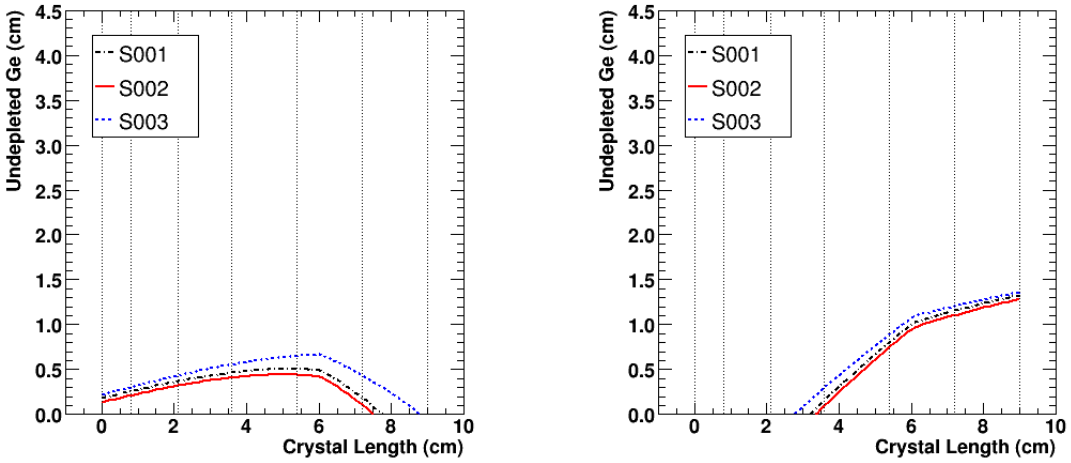

Figure 4.6: (a): (*left*) Undepleted region of Ge calculated using the average radial distance between contacts and using Equation 2.10. The impurity concentration values are as shown in Figure 4.2. The inner contact is assumed to be at a radius of 5 mm throughout the depth of the crystal, although this is not the case in the front two rings of the detector. It should be noted that the y-axis does not represent the absolute radius but the thickness of Ge (absolute radius minus 5 mm). (b): (*right*) As for (a) but with the impurity concentrations reversed such that the purest HPGe is at the front of the crystal.

However, experimental experience with the detectors suggests that they operate at full depletion. Basic knowledge of semiconductor detector physics, described in Sections 2.2 and 2.3, would imply that any regions of non-depleted material would contain free charges, primarily donor electrons, which would recombine with the information carrying charges from a radiation event and cause increased signal noise. As bias voltage is applied and reaches a significantly high value, the signal noise decreases sharply and, at this voltage, the detector is thought to be depleted. Furthermore, it is customary to operate detectors of this type significantly above their depletion voltage as this serves to homogenise the electric field and to saturate the charge carrier drift velocity (desirable for timing measurements). There are three proposed explanations for the depletion of the detectors in spite of Figures 4.3 and 4.6(a):

1. There are radial variations in impurity concentration which allow for adequately pure inner regions of the detectors such that they are depleted within the conditions of applied voltage and distance.

2. The impurity values stated in the data sheets are incorrect. No indication of the uncertainty of the measurements is given.

3. The concentration of impurities is reversed from Figure 4.2, causing the most pure part of the material to be at the front of the detector. Figure 4.6(b) shows the expected region of undepleted Ge if this were true. Evidently this would not account for the experimental evidence in support of full depletion.

It is also suggested that inner regions may not in fact be fully depleted in accordance with the calculations performed. In this case the donor electrons one would expect in undepleted n-type material, and thus the expected electronic noise, could be influenced by the strong electric field caused by the application of the high positive voltage in this region of the detector. The electric field strength is considered in the next section. The donor electrons which are not covalently bonded to the lattice atoms, as they are in the depleted material, would be attracted to the central anode and the only evidence of undepleted material would be an insensitivity to incoming radiation in these areas.

4.1.4 Electric Fields

Equation 2.12 can be used to calculate the electric field within the detectors. The first term of the equation represents the contribution that the fixed (space) charges make to the total field and has a linear dependence with radius. The second term represents the contribution of the free charges within the crystal and is greatly influenced by the presence of the bias voltage. The total electric field and its contributory factors can be seen as a function of radius in Figure 4.7. The calculation was performed for a depth of 4 cm into the S002 crystal and the impurity concentration was calculated according to the linear fit in Figure 4.2.

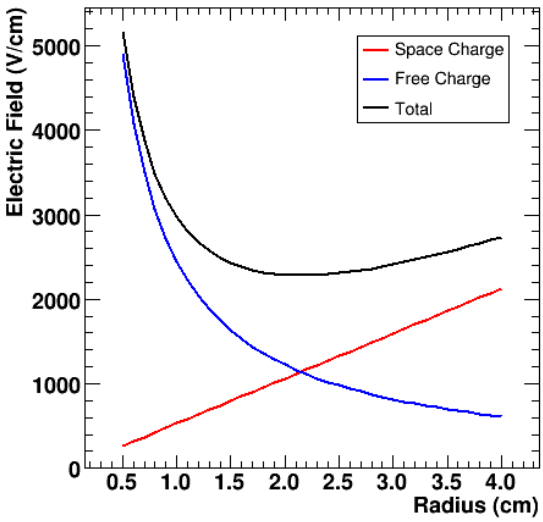

Figure 4.7: The electric field as a function of crystal radius calculated using Equation 2.12. The contributory components of space charge and free charge are also shown on the plot. It can be noted that although the plot extends to a radius of 4 cm, the average Germanium radius at this depth (4 cm) is only 3.6 cm due to the taper.

Although the cylindrical polar coordinates assumed for ease of calculations are a fair estimate to the real situation, it is appropriate to briefly consider the geometry of the six corners of the hexagon in a qualitative manner. The geometry of these crystal

edges has many implications to the electric field in these areas and this is evident in Chapter 5. It can be considered that the concentration of impurity atoms per unit centimetre at the extremities of the hexagonal shape is approximately one sixth that of the bulk of the volume. As the electric field produced by each impurity atom is local to its surrounding volume, and the contribution of each will be summed to give a total space charge field, this field will also be reduced to approximately one third of its expected value. For the example in Figure 4.7 for the S002 crystal at a depth of 4 cm, the space charge electric field at the hexagon apexes ($r \approx 3.6$ cm) would be $\sim 2500/3 \approx 833$ V/cm. This creates a total electric field, resulting from both fixed and free charges, of $\sim$1533 V/cm compared to $\sim$3200 V/cm in the bulk of the volume. Furthermore, following the same argument, the space charge field across the entire front face of the crystal is reduced by a factor of two, creating a value in the crystal corners of one sixth that of the bulk of the crystal. The reader is referred to the next chapter to see these effects.

4.2 Photon Scans

A number of highly collimated photon scans were performed on S002 and S003. An automated scanning table produced by Parker [Pa07] was utilised to scan a γ-source (and its lead collimation system) in 2 dimensions. The apparatus is capable of motion in the xy plane to a precision of 50 μm and is described in more detail in [De02]. Scans were performed using two methodologies; *singles* and *coincidence*. Coincidence scanning involves the use of a secondary collimation system perpendicular to the injection collimator which ensures that only photons which scatter through an angle of 90° within the primary detecting volume are incident on an arrangement of scatter detectors. This method allows the determination of the third dimension of the photon interaction site (z) from the position of the secondary collimator when the two detecting systems fire in coincidence. However, the time required to obtain adequate statistics limits the number of positions it is possible to investigate. Typically $\sim$5

hours are required per xy coordinate, which implies that it is only possible to scan a fraction of the detector volume in a realistic finite time. The coincidence procedure and analyses are discussed in detail in [Di07].

4.2.1 Singles Scanning

Singles mode involves the simple system of the injection source and collimator, scanned in the xy plane, and the primary detector only. The only information on the third dimension of the interaction position is obtained from the detector response. Singles scanning has the advantage of taking considerably less time than coincidence, allowing a full detecting volume to be investigated in a fine cubic grid. The only scanning mode discussed in the present work is singles - detailed results of which are included in Chapter 5.

The injection collimator was 1 mm in diameter and 11.9 cm long. The γ-radiation used in the scans discussed in this work was provided by a 990 MBq Cs-137 point source, with an energy of 662 keV. A threshold of $\sim$420 keV, set by an external Constant Fraction Discriminator (CFD), was applied to the central contact and this provided the trigger for the data acquisition. The majority of photons Compton scattering out of the detector would therefore not be recorded, although partial energy deposition can occur in any given segment.

4.2.2 Signal Manipulation and Data Acquisition

The high voltage was applied to the central contact in all cases, and was supplied using NIM modules, as was the preamplifier power ($\pm$12 V). The differential signals from the preamplifiers were transmitted via 7 LVDS cables,[2] each 5 m in length, and were converted to single-ended signals using CWC converter boxes manufactured at the

[2]One cable transmits the signals from the core electrode and each of the remaining six cables convey the information from all six rings of a sector.

Technical University in Munich. The converter boxes output 37 signals (36 segments plus the core channel) and these were conveyed to 10 GRT4 digitiser cards [La04b] using Lemo cables. Each card consists of 4 channels, pertaining to 4 electrodes, which sample the analogue signal over ±1 V using 14 bit 80 MHz FADCs. An external CFD from the central contact signal was used to trigger the cards. Moving Window Deconvolution (MWD) algorithms are used within the cards to digitally synthesise the pulse shapes in real time and hence extract the required energy [La04a]. Each channel provides 250 samples of the preamplifier pulse for each event as well as the MWD derived energy, a 48 bit time stamp and a value for the signal baseline. This data were read out to a Linux DAQ PC.

The data were acquired using MIDAS (Multi Instance Data Acquisition System) [Mi03] and recorded using an Eurogam input handler in MTSort [MT06] to SDLT tape for offline analysis. Subsequent presorting using a combination of MTSort and ROOT [RO07] programming results in the generation of a reduced size dataset in ROOT tree format. This dataset is geometrically suppressed and comprises only the hit segment and its neighbours for each event. The trace length of each channel is also reduced in the presorting process from 250 samples (3.13 μs) to 60 samples (0.75 μs), keeping only the mid-section of the pulse which contains the desired information.

4.2.3 Energy Calibration

Two sets of energy calibrations were performed on the data. γ-ray sources over a range of known energies were used to collect spectra. One of the calibrations was performed using the baseline difference between the beginning and the end of the pulse to extract the energy. The other calibration coefficients were obtained from the energies calculated by the MWD algorithm. The latter uses much more sophisticated pulse processing techniques [La04a] and therefore results in a much better energy resolution. However, the former and more crude approach is used frequently in this analysis as it does not mask the performance of the detector - largely the subject of

discussion. In both cases the response as a function of energy was almost linear and the following equation was used to calculate the energy, E,

$$E = a + bx + cx^2 \tag{4.1}$$

where x is the channel number and c, the squared term coefficient, was small.

4.3 Detector Performance

4.3.1 Energy Resolutions

Energy resolution measurements were taken prior to the detector scans using analogue electronics. The output cables from the converter boxes were input to a spectroscopy amplifier with 6 μs of shaping time. The spectra were collected using MAESTRO software. The results obtained using a 111 kBq ^{60}Co source, producing a core count rate of $\sim$1 kHz, are displayed in Figure 4.8 for both the S002 and S003 detectors. The reader may a observe a general, but not restrictive, trend which suggests that the resolution of a segment is dependent upon the ring to which it belongs (recall the labelling scheme in Table 4.1). This is explained by Equation 2.27, which relates the signal noise to the capacitance of a detecting element, which in turn is dependent upon its volume. Although the physical segmentation (and tapering) imply that the smallest segments are in the front ring of the detector and each successive ring contains larger segments, the effective segmentation dictates otherwise [Go03]. One implication of this fact is that the front ring segments are larger than the second ring and they therefore have a larger capacitance, evident in the generally slightly worse resolutions of ring 1 segments compared to ring 2 segments. This can be seen more clearly upon consideration of the arithmetic mean of the energy resolution of each ring of segments and is plotted in Figure 4.9. The pattern appears consistent between the two energies and, with the exception of the fourth ring, consistent between the two detectors. This discrepancy towards the back few rings of the detectors could be a result of the difference in impurity concentration discussed in Section 4.1.3.

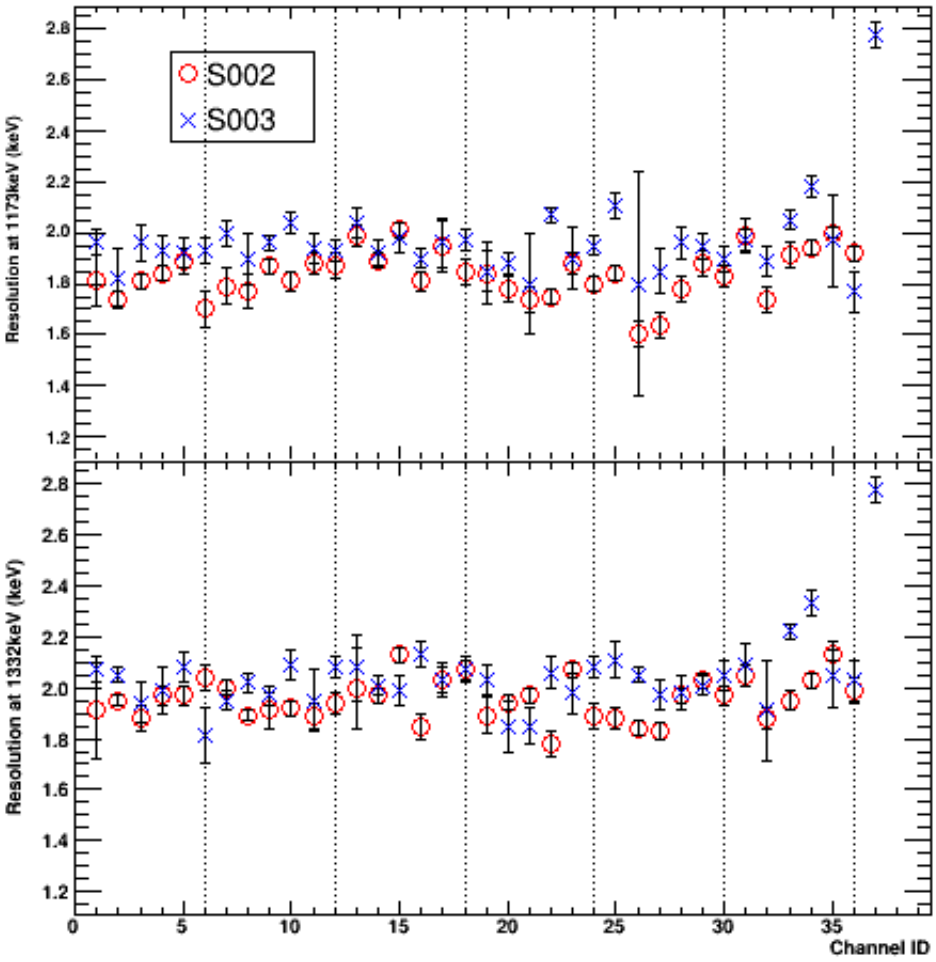

Figure 4.8: Measured FWHM of each channel of S002 and S003 at both 1173keV and 1332keV. Note that the core contact energy resolution is worse than that of the segments due to the fact that it incorporates a larger volume and hence has greater capacitance.

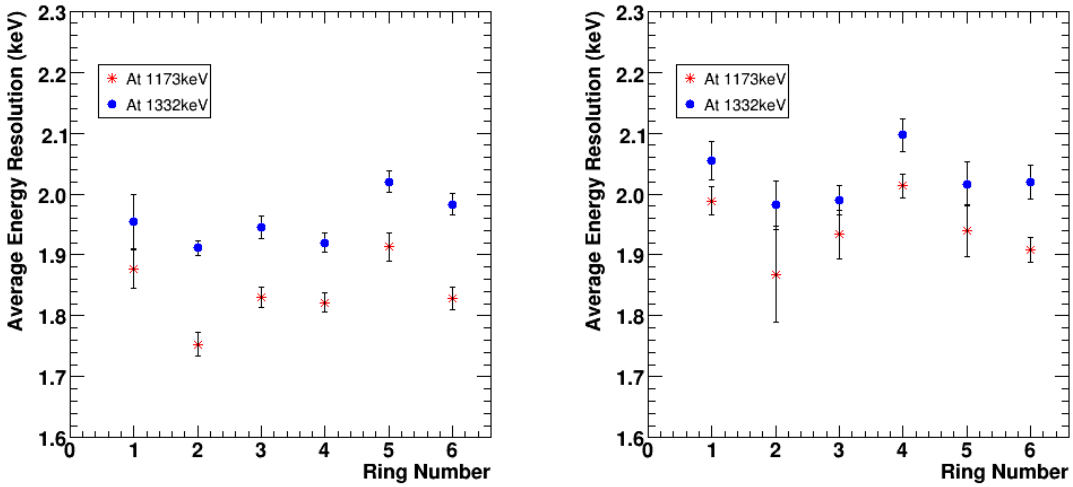

Figure 4.9: Average energy resolution for each ring of S002 (left) and S003 (right).

4.3.2 Efficiencies

The absolute efficiencies of S002 and S003 were measured as a function of energy using a 219 kBq ^{152}Eu point source at a distance of 25 cm from the detector's front face. The results for both the S002 and S003 detectors are shown in Figure 4.10. Evidently S002 is the more efficient detector. It is recommended that the last data point in the S003 data series, which causes the trend to increase with energy, is ignored. It is not physical that the detector's efficiency increases at this energy as the germanium-photon interaction probability decreases with energy, as described by Figure 2.1. The relative efficieny of these detectors as well as a comparison to the manufacturers specifications is discussed in Reference [Di07].

4.3.3 Noise Performance

Figure 4.11 displays the average baseline value of each channel of S002 and S003, as well as the peak-to-peak noise, the RMS noise and the standard deviation of the baseline samples. (Table 4.1 shows the segment labelling scheme.) Each noise parameter is calculated over the first few samples of each pulse before it starts to rise and

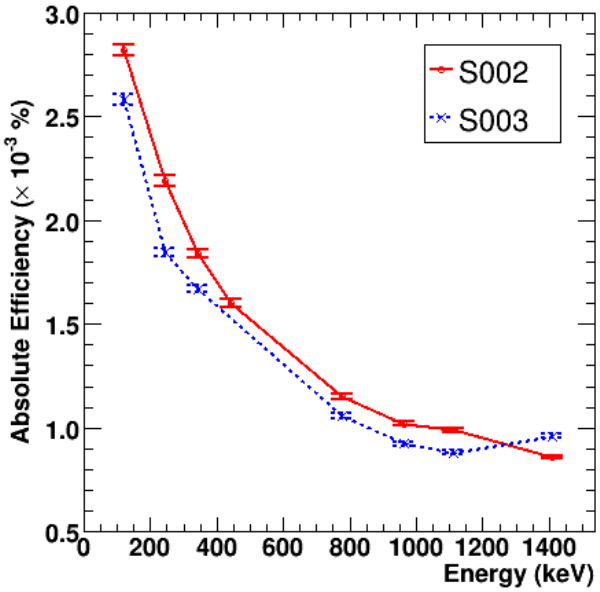

Figure 4.10: Absolute efficiency of S002 and S003 as a function of γ-ray energy. The expected maxima in the curves at low energy are not visible with the energy range measured.

from the last few samples, after taking into account any baseline shift. The values shown are obtained by taking the arithmetic mean of the respective noise parameter over the entire front face singles scan data set (described in Chapter 5). The number of interactions per channel is also shown in the bottom plot for completeness (note that there is a logarithmic scale on the y-axis of this plot). The noise pattern through the depth of each sector is clear, this is discussed in Section 4.3.1 and is associated with the size of the detecting volume. It is not clear why the segments in the 5^{th} and 6^{th} rings of S003 have significantly more noise and a larger negative baseline than the rest of the segments, although the pattern is repeated in S002 but to a far less extent. It does appear that, in general and with the exception of the back two rings, the segments of S002 have more noise than those of S003 although this is not reflected in the energy resolution measurements of Section 4.3.1.

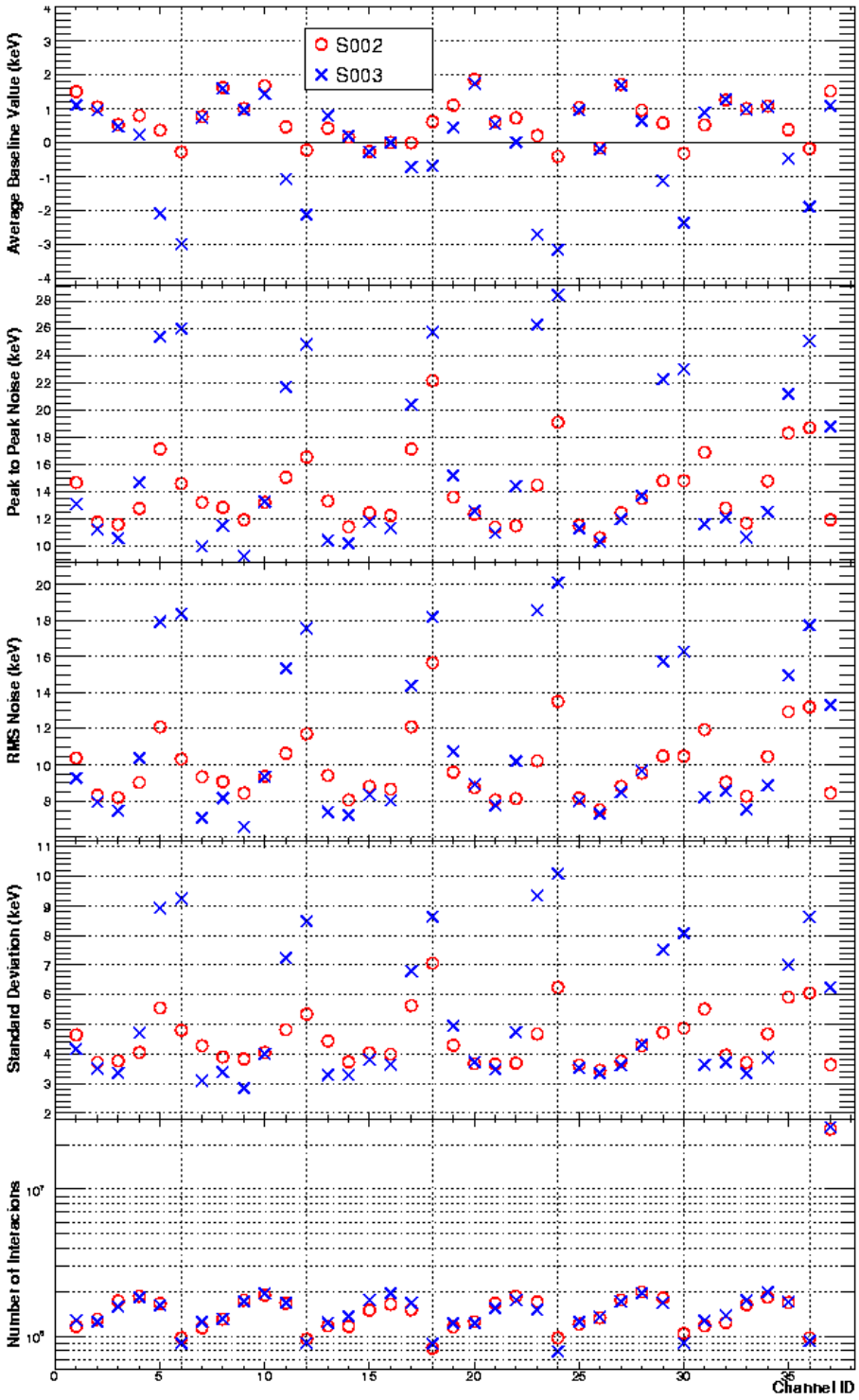

Figure 4.11: Baseline noise values of each channel of the S002 and S003 crystals. See the text for further description.

Using Fourier analysis it is possible to investigate the electronic noise in the time domain. The noise signal from segment E1 of each of the 2 detectors can be seen in Figure 4.12. The calibration to keV was performed using the baseline difference gain coefficients as described in Section 4.2.3. A Fast Fourier Transform (FFT) was used to produce the noise power spectrum which can be seen in Figure 4.13. The power spectrum for the S002 electrode indicates more low frequency noise than that of S003, including a large amount below 1 MHz. The dependence with frequency could be qualitatively compared with a *1/f* shape and could therefore be indicative of noise induced due to trapping sites within semiconducting material, discussed in Section 2.5.2, although it is not possible to speculate this with conviction without a higher quality noise signal. The power spectrum for the S003 electrode indicates that the biggest contribution to the noise is at a frequency of about 12 MHz.

It is possible that the differences between the power spectra of the two detectors can be attributed to their different preamplifiers although, without further investigation, this is purely speculative. There are three preamplifier designs which are being tested with AGATA detectors, designed by institutions at Milan, Köln and GANIL [Pu04a]. The Köln preamplifiers are utilised on the central contact of each of the three prototype detectors, the GANIL designed preamplifiers are fitted to the outer electrodes of S001 and S002 while thse from Milan are used on the outer contacts of the S003 detector.

The integrated power spectrum of S002, visible in Figure 4.14, shows a sharper initial rise with frequency than S003 and plateaus at a value of approximately 3.2 keV (10 keV^2). That of S003 rises more linearly with frequency and plateaus at approximately 2.9 keV (8.3 keV^2). The plateau values approached by the density curves represent the total white noise of the detector-preamplifier configuration, including thermal and shot noise, and are inherently low due to the fact that cold preamplifiers are utilised. From this discussion, it is evident that the S003 outer contact preamplifier (Milan) performs marginally better with a spectral density of 2.9 keV, compared to that of

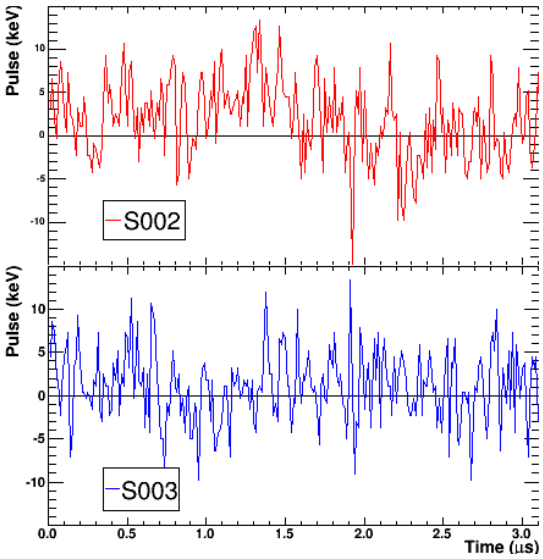

Figure 4.12: Noise signals from the E1 segment electrodes of S002 and S003. The pulses were each 250 samples long and digitised at a frequency of 80 MHz.

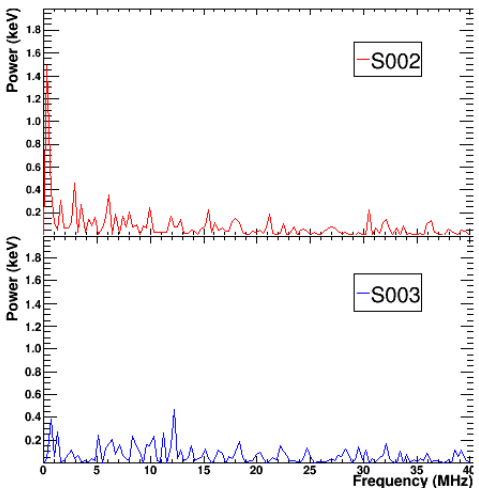

Figure 4.13: Power spectrum of the noise signals from Figure 4.12.

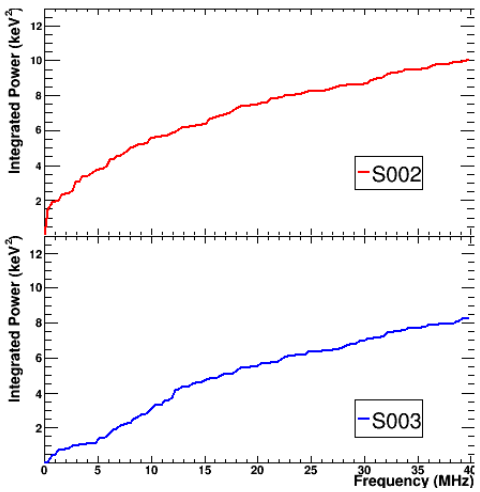

Figure 4.14: Integrated power spectrum of the noise signals shown in Figure 4.12.

3.2 keV for S002 (GANIL).

Chapter 5

Front Face Singles Scan

The detector is positioned such that its front face is parallel to the xy-plane. Figure 5.1 shows the setup. The scanning table moves in this plane in 1 mm steps over a square grid of approximately 85×85 mm. The collimated photon beam from the ^{137}Cs source shines vertically upwards, parallel to the z-axis, and stays at each position for 60 seconds before moving to the next. The orientation of the detectors with respect to the scanning coordinates axes can be seen in Figure 5.2 and was the same for both the S002 and S003 detectors.

5.1 Intensity of Counts as a Function of Position

Figure 5.3 shows the intensity seen by the core electrode for both the S002 and S003 crystals and Figure 5.4 shows the intensity map for each ring of segments. The only requirement on the energy of the interaction is that it passes the core CFD threshold. There is no requirement placed on the segment fold of an event. These conditions lead to the apparent increase in statistics around the segment boundaries in the ring plots. In these regions photons are likely to scatter between the segments before a photoelectric absorption occurs; the core will see a full energy event and there will be more than one segment reading a fraction of the full energy. The attenuation of the photons through the length of the detectors can be observed toward the back rings

Figure 5.1: Photograph of the S002 AGATA prototype detector in position for the front face singles scan. The collimation system comprised of lead bricks and a lead collar can be seen sitting upon the scanning apparatus. The detector is suspended over the collimator by a wooden plate beneath its dewar so that the scanning table, source and collimation system are free to move beneath it.

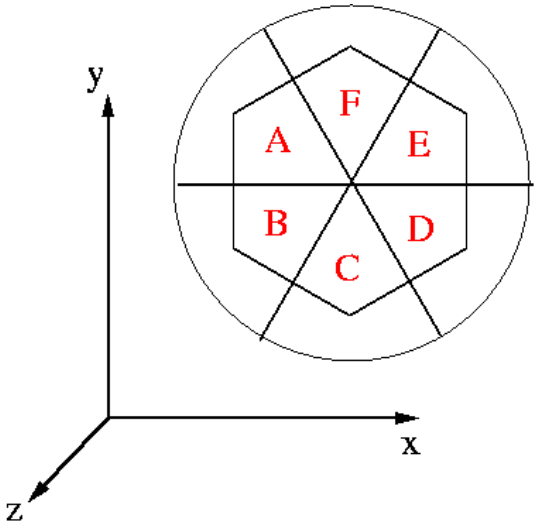

Figure 5.2: Detector orientation with respect to the scanning coordinate axes, as viewed from above.

and the areas where the photon beam shines directly into a tapered face, as opposed to traversing the full length of the crystal, have far greater statistics than the inner regions of these rings. The presence of the central bore hole can be seen in all but the first ring; its endpoint is 1.3 cm from the front face (in the 2nd physical ring). What is immediately noticeable by comparison of the two core intensity maps of Figure 5.3 is that there are more counts in the bulk of S003 than S002 despite the fact that, according to Figure 4.10, S002 is the more efficient crystal. Efforts were made to keep conditions identical between scanning the two detectors, however this discrepancy can be attributed to the fact that the trace length read by the digitising cards was changed from 256 to 128 samples between these two scans. With the longer trace length, the S002 scan had a greater system dead time.

Also evident from both Figures 5.3 and 5.4 is that the diameter of the central bore hole appears bigger in the S003 crystal. In order to quantify the difference, slices through the intensity maps can be plotted. These can be seen in Figures 5.5 and 5.7. There are a number of possible explanations for the difference:

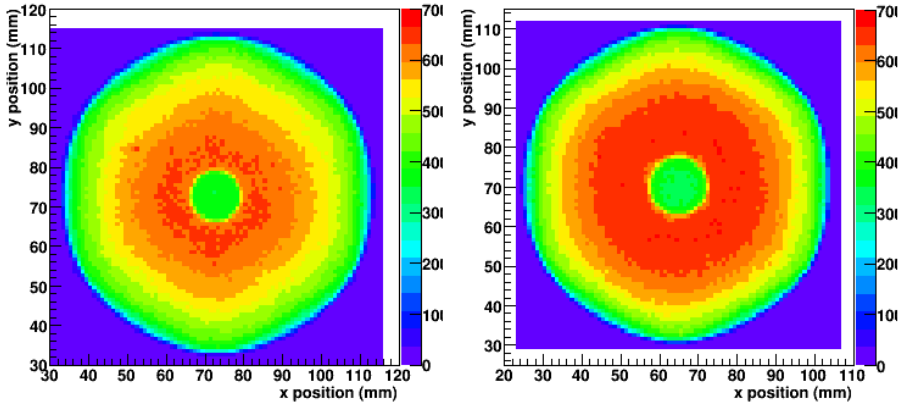

Figure 5.3: Photon interaction intensity maps as seen by the core electrode of S002 (left) and S003 (right). The coordinate system can also be observed; the z-axis points vertically upwards (out of the page).

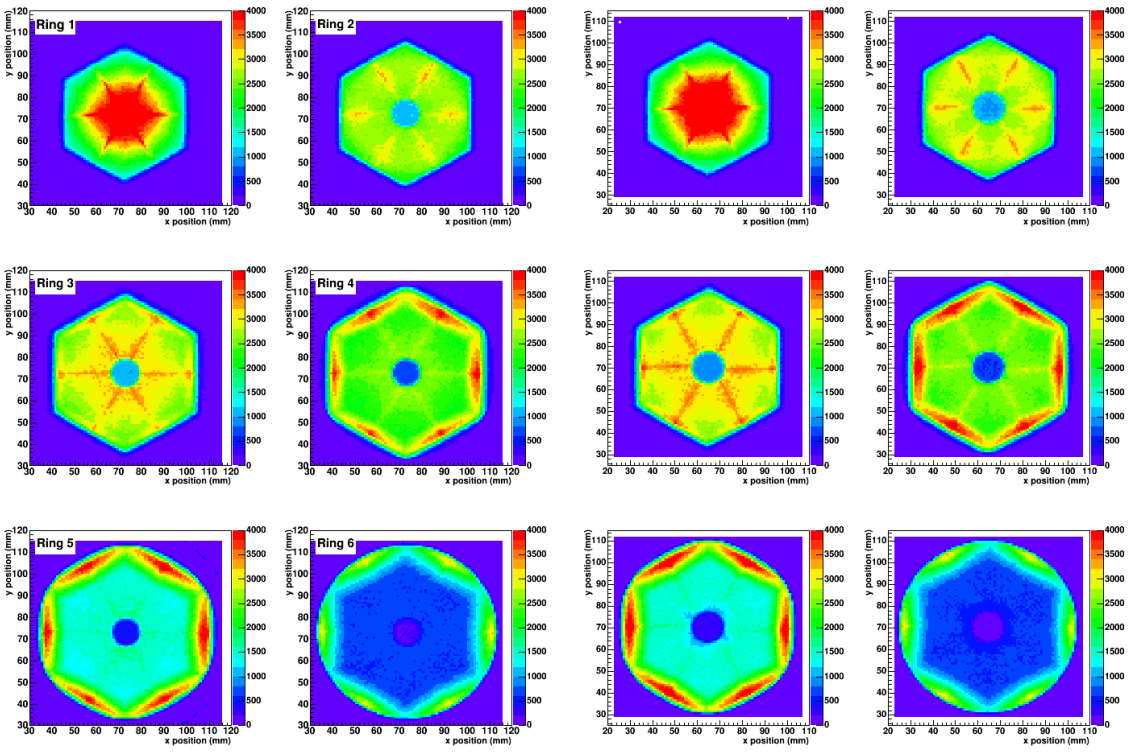

Figure 5.4: Photon interaction intensity maps for each ring of S002 (left) and S003 (right). See the text for a discussion of the plots' appearances.

1. The bore hole was physically drilled bigger in the S003 crystal than the S002. This is unlikely, as the crystals are well machined and such a large difference (1-2 mm) is likely to be outside of the expected uncertainty. If this were the case, one would expect consistency throughout the depth of each individual crystal.

2. The bore hole is not physically bigger but the Lithium contact was diffused further into the HPGe crystal.

3. It has been known that if a poor contact has been produced and identified by a detector manufacturer, the hole is re-drilled with a slightly larger diameter to remove the diffused Lithium in order that the contact be recreated. Again, it would be reasonable to expect that each bore hole be uniform throughout its length.

4. The operating voltage of S003 is not sufficient to deplete the entire volume of the crystal as suggested in Section 4.1.3 creating a region of HPGe close to the inner contact that is insensitive to incoming radiation. This would have implications to the electronic noise observed, as discussed in Section 4.1.3, and also to the drift velocity of the charge carriers which may not be saturated in all regions of the crystal.

Figures 5.5 and 5.7 can be used to estimate the effective size of the bore hole. The results of the estimation for the core electrode and rings 2 to 6 of both crystals (the bore hole is not present in the first ring) are displayed in Figure 5.6. The approximate depth of the x-axis is taken as the mid-point of the physical ring boundaries. The error bars are large due to the crude nature of the estimation and could in fact allow for a bore radius which is constant with depth. Despite the large error bars, it is clear that the difference between the effective radii of the two bore holes is 1-2 mm. This difference is consistent with the difference between the calculated undepleted regions of germanium for the two crystals depicted in Figure 4.6(a). The magnitudes of the

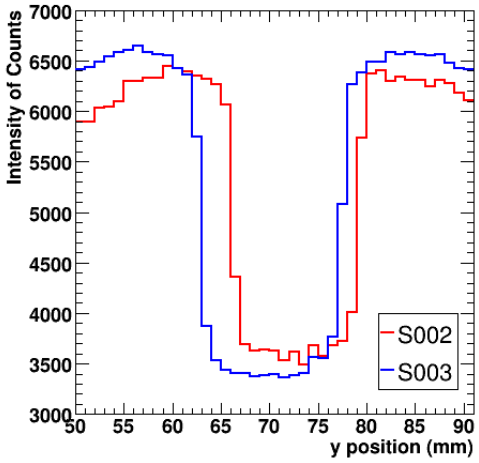

Figure 5.5: Intensity of counts seen by the core electrode as a function of y-coordinate for both the S002 and S003 crystals. The x-coordinate was chosen to be at the centre of intensity (discussed in more detail in the next section), namely x=73 mm for S002 and x=65 mm for S003.

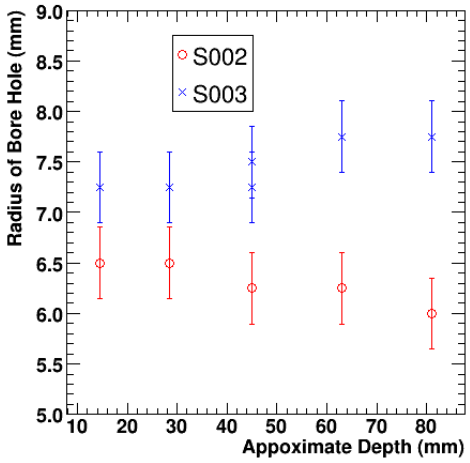

Figure 5.6: Effective radius of the bore hole for the S002 and S003 crystals, estimated from Figures 5.5 and 5.7.

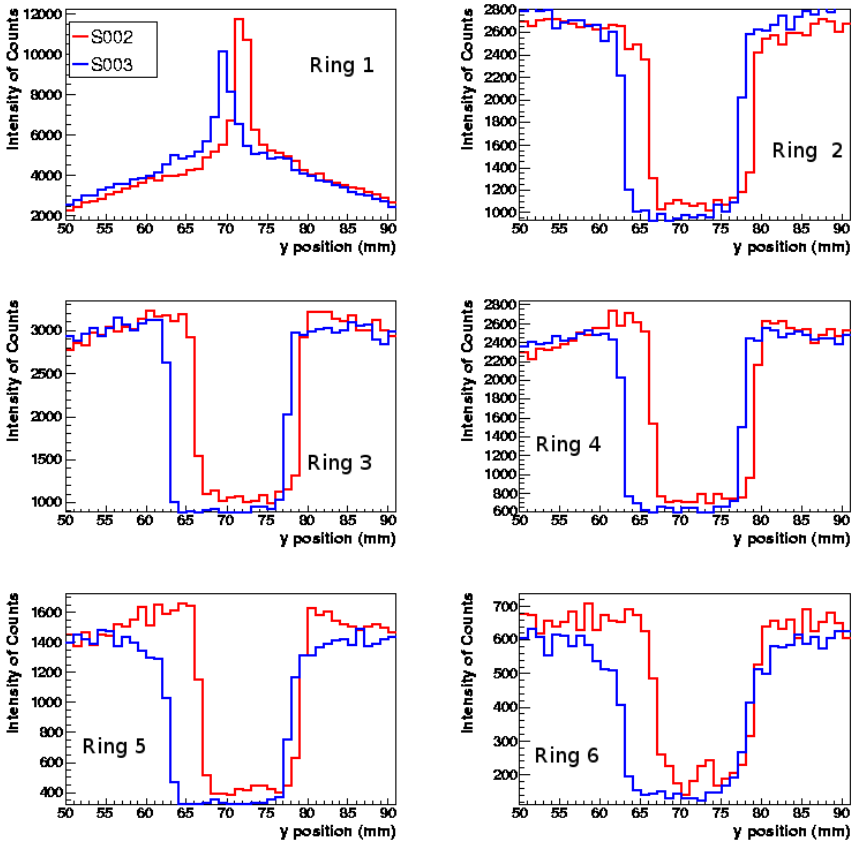

Figure 5.7: Intensity of counts for each ring of segments as a function of y-coordinate for both the S002 and S003 crystals. The x-coordinate was chosen as for Figure 5.5.

insensitive regions calculated and measured differ by a factor of approximately 2, this could however be explained by the fact that Equation 2.10 which is used to calculate the depletion width is more suited to a planar detector configuration than a coaxial.

5.2 Energy Gated Intensity of Counts

Gating on the photopeak energy of ∼662 keV reveals more information on the segmentation of the detectors. Photons that interact close to a segment boundary are more likely to scatter out of that segment, depositing only partial energy. This is evident as a reduction in photopeak events close to the segment boundaries. Photon interaction mechanisms are discussed in Chapter 2.1. The energy gated intensity of counts can be seen in Figure 5.8 for both the S002 and S003 detectors, as can the segment boundaries.

5.2.1 Incomplete Charge Collection

Evident from the plots, in each of the first rings, are regions at the extremities of specific axes that seem insensitive to full energy deposition. These occur in sectors C and F of S002 and sectors A and D of S003. It is apparent in Section 5.4 that the crystallographic axes are not in the same direction with respect to the segment labelling scheme for both of the detectors[1]. The orientation of the principal crystallographic axes can be seen in Figure 5.9 for both of the detectors. Furthermore, the ⟨100⟩ directions correspond to the positioning of these regions of insensitivity to full energy deposition. Inspection of the energy spectra from the contacts reveals that there is a low energy tail. This is most easily visible on the core contact and is displayed in Figure 5.10.

[1] AGATA specifications require only that one of the primary lattice axes crosses through the centre of one of the flat sides, but no relation to the segmentation is maintained between the detectors.

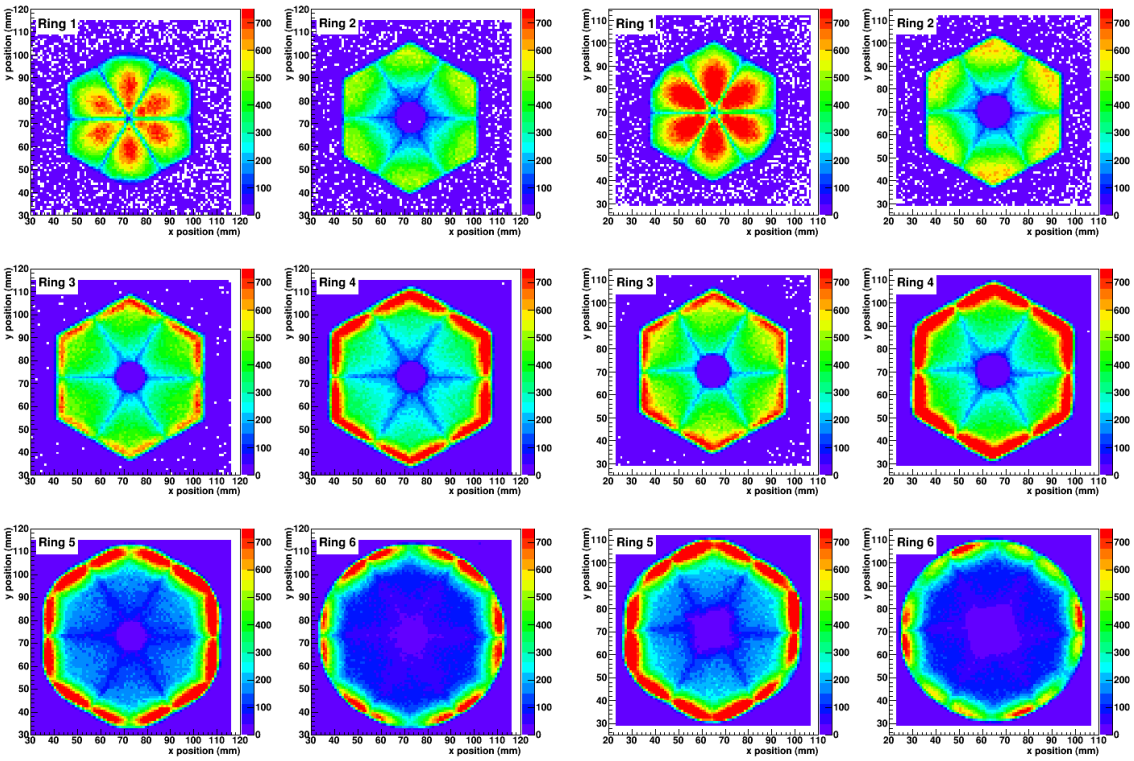

Figure 5.8: Photopeak energy gated photon interaction intensity maps for each ring of S002 (left) and S003 (right). See the text for a discussion of the plots' appearances.

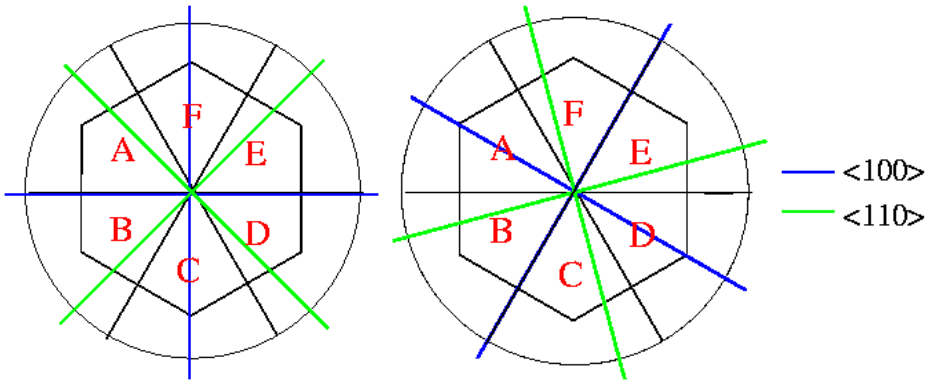

Figure 5.9: Location of two of the principal crystallographic directions with respect to the detector segmentation boundaries for both the S002 (left) and S003 (right) detectors. It should be noted that the angular brackets denote the family of equivalent directions which arise due to the symmetry of the lattice. The location of the axes are defined in the manufacturers specification sheets included in Appendices B and C.

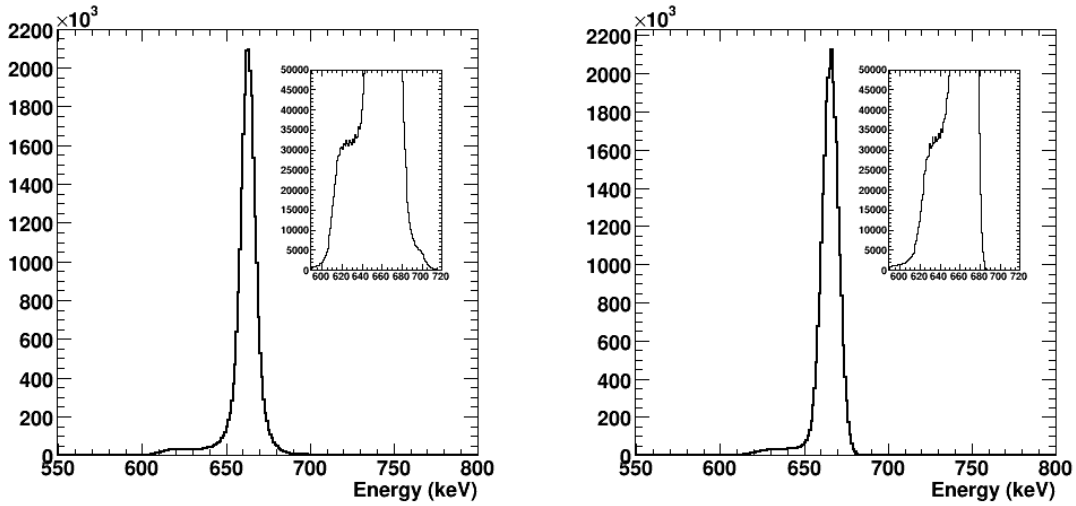

Figure 5.10: Energy spectra in the photopeak region from the core contact of S002 (left) and S003 (right). The energy was calculated using the baseline difference between the start and end of the pulse (hence the poor energy resolution). The inserts show the same spectra zoomed in. A low energy tail can be seen.

Gating on events which fall into the low energy tail of each of the outer electrodes (600 to 640 keV), produces the intensity maps seen in Figure 5.11. It is thought that the reduced space charge electric field strength at crystal extremities, as described in Section 4.1.4, is partly responsible for the patterns in Figure 5.11. Low field regions would imply that the charge carrier drift velocities do not reach their saturation value, and the pulse would struggle to reach its full height in the time window allocated. From Figure 2.7 it is clear that the crystallographic axes affect the drift velocity of electrons. The present evidence further implies that the $\langle 100 \rangle$ axis requires a higher electric field in order for the charge carriers to reach their saturation velocity. Similarly, gating on the low energy tail of the core contact energy spectra produces the plots in Figure 5.12. In this case, events which occur close to the core contact display incomplete charge collection, and a definite ring is observable in this region. It is possible that this is the location of the contact itself and charge is lost within this region. It can be noted that this ring has a larger radius in S003 than in S002.

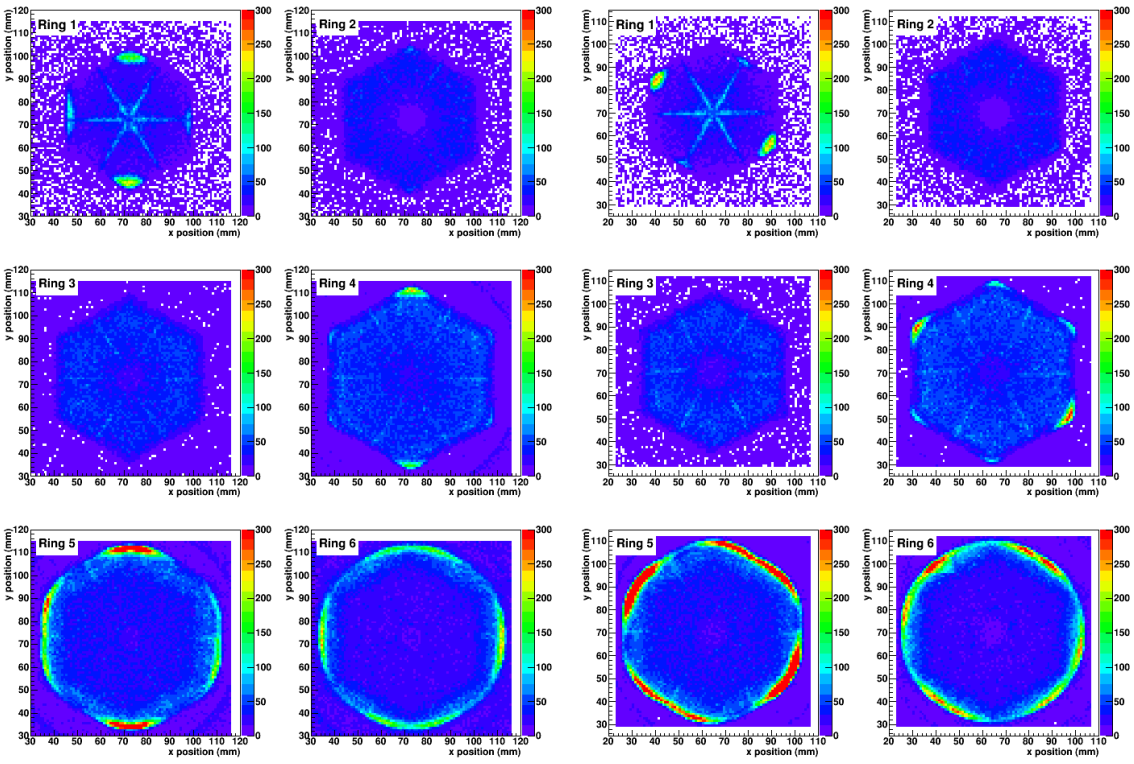

Figure 5.11: Photon interaction intensity maps for each ring of S002 (left) and S003 (right), gated on the low energy tail of the photopeak. See the text for a discussion of the plots' appearances.

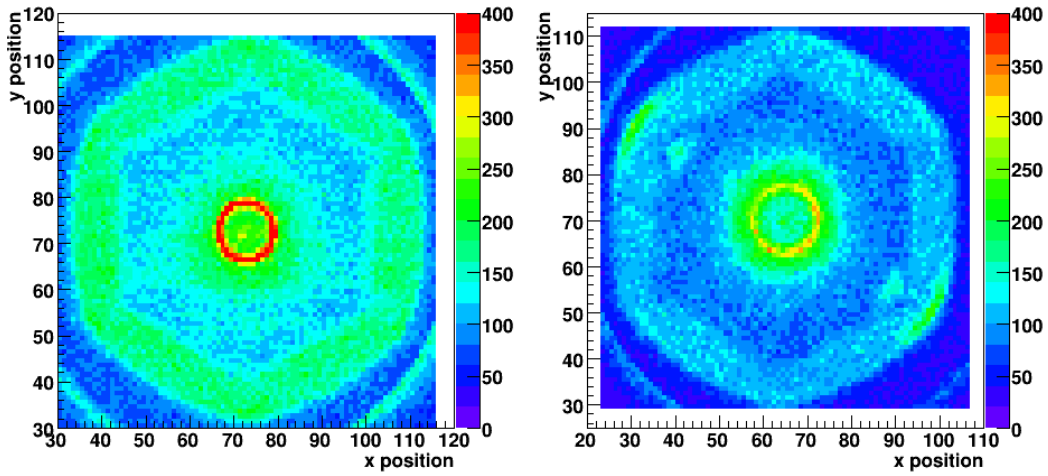

Figure 5.12: Photon interaction intensity maps for the low energy tail events seen by the core electrode for the S002 (left) and S003 (right) detectors.

5.2.2 Trajectory of Charge Carriers

Also evident from Figure 5.8 is that the segment boundaries of the S003 crystal appear inconsistent in y-position across the bore hole in all but the front ring. Upon closer inspection it is evident that, for both detectors, opposite segment boundaries are only co-linear when they lie on a primary lattice axis. For the geometry of AGATA detectors only the $\langle 100 \rangle$ axis coincides with a segmentation boundary and this can be seen in Figure 5.9. The patterns observed are direct evidence of the tensorial nature of the mobility of charge carriers, discussed in Section 2.4.3, which is only aligned with the electric field vector when the lattice orientation is such that it has rotational symmetry. Thus, when the electric field vector is not aligned with a primary lattice axis the charge carriers do not follow the expected radial path. The front ring does not display the same behaviour due to the fact that the electric field vector is no longer radial in the regions underneath the anode. The most significant result of this phenomenon is the difference in effective size of the segments within a ring. Segments in which the $\langle 100 \rangle$ axis is central have a smaller effective size.

5.3 Crystal Alignment

It is not acceptable to assume that the Ge crystal, and hence the detecting volume, is aligned precisely with the cryostat which holds it. Thermal isolation of the crystal necessitates spacing between the crystal surface and inner cryostat wall, quoted as (2.7±0.5) mm, and this in turn implies that there may be some inaccuracy in the crystal's position with respect to the cryostat, and hence to the laboratory reference frame. In the case of both detectors, the cryostat was aligned to the scanning table in the xy plane by eye. The z alignment was provided by using a spirit level on the only accessible horizontal surface of the detector (the top of the dewar). The precise positioning of each crystal with respect to the scanning table can be inferred from the intensity maps discussed in the previous section. From these plots it is possible to determine both the angle of rotation of the detector in the xy-plane and the geometrical centre of each ring, which leads to an angle of axial tilt from the z-axis.

5.3.1 Angle of Tilt

In order to accurately determine the centre of the detector, a centre of gravity approach upon the intensity plots shown in Figures 5.3 and 5.4 is adopted. Without assuming that the crystal's axis is aligned with the laboratory z-axis, the centre of each ring of segments is calculated to give the x and y-coordinates of the central axis as a function of z-depth. For each ring of segments, assuming i=1,2,3 ..n bins along the x-axis, and j=1,2,3 ..m bins along the y-axis, the x-coordinate of the centre of intensity is found by summation of the contents of all y-bins of each x-axis bin to give the total intensity of each x-bin, I_i. The following equation is then applied to give the x-coordinate of the centre of intensity

$$xc = \frac{\sum_{i=1}^{n} I_i x_i}{\sum_{i=1}^{n} I_i} \tag{5.1}$$

Similarly for the y-coordinate of the centre of intensity,

$$yc = \frac{\sum_{j=1}^{m} I_j y_j}{\sum_{j=1}^{m} I_j} \tag{5.2}$$

As the crystal geometry is symmetric about both x and y, this centre of intensity approach will be independent of any rotation of the crystal in the xy-plane. Figure 5.13 displays the results of applying Eq. 5.1 and Eq. 5.2 to the ring intensity maps (Figure 5.4) and the core intensity map (Figure 5.3) for the S002 crystal. Figure 5.14 shows the results for the S003 crystal. The depth dimension, z, is approximated as the geometrical mid-depth of the ring (or the whole detector in the case of the core electrode). An error of 0.5 mm is applied to the z-dimension and is not visible in the figure. The errors which can be seen originate from the counting uncertainty of the contents of each bin ($\sqrt{I_{ij}}$) and the uncertainty associated with the xy binning (0.5 mm). The fits performed yield the angle of axial tilt from the z-axis, θ, and the direction of the tilt in the xy plane from the positive x-axis, ϕ.

$$\begin{aligned} \theta_{S002} &= (1.81 \pm 0.17)^\circ \\ \phi_{S002} &= (48 \pm 3)^\circ \\ \theta_{S003} &= (1.12 \pm 0.17)^\circ \\ \phi_{S003} &= (323 \pm 5)^\circ \end{aligned}$$

5.3.2 Angle of Rotation

In order to find the angle by which the crystal is rotated in the xy-plane with respect to the measurement frame, a similar approach to that described above is adopted. The y value of the centre of intensity of each x-axis bin of the plots in Figures 5.3 and 5.4 was found and a linear fit was performed across all of the x-bins for each plot. However, it should be noted that the detectors' axial tilt, described in the previous section, leads to inconsistency across the xy plane of the physical distance

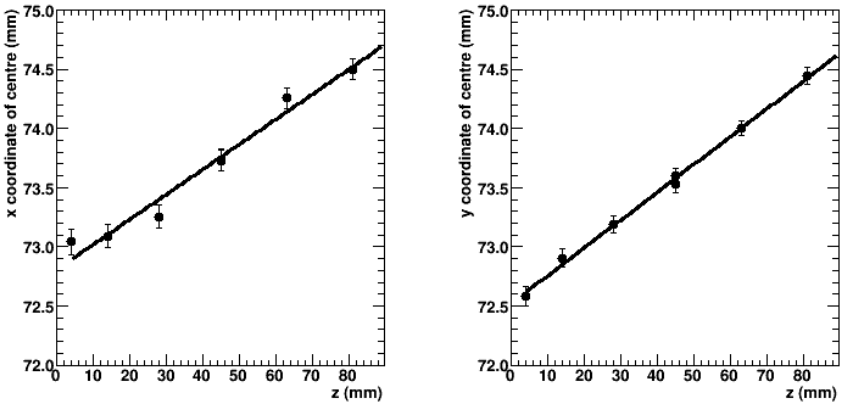

Figure 5.13: Coordinates of the centre of intensity for the S002 crystal as a function of depth. See text for further description.

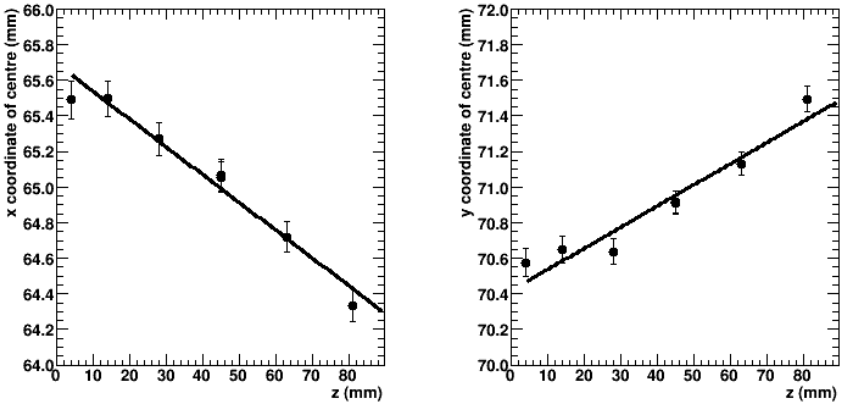

Figure 5.14: Coordinates of the centre of intensity for the S003 crystal as a function of depth. See text for further description.

in z from the source, as much as Δz=2.5 mm at the widest part of the S002 crystal. The intensity of electromagnetic radiation follows an inverse square law with distance from its origin, and the difference in intensity from one side of the detector to the other can therefore be calculated according to,

$$\frac{I_2}{I_1} = \frac{r_1^2}{(r_1 + \Delta z)^2} \tag{5.3}$$

The difference can be as much as 3 % at r_1=14 cm from the γ-source and is greater than the statistical error, $\sqrt{I}$ (typically ∼1.5 %). It is therefore necessary to correct the intensity of each bin according to the angle of axial tilt before the rotation calculation is performed to avoid skewing of the centre of each x-bin towards the direction of the axial tilt. The y centre of intensity for each x-bin, xc_i is given by

$$xc_i = \frac{\sum_{j=1}^{m} I_{ij} y_j}{\sum_{j=1}^{m} I_{ij}} \tag{5.4}$$

where I_{ij} is the corrected intensity of counts in the y=j, x=i bin. The linear fit was performed across the n bins of the x-axis and the method was repeated across the y-axis. The arithmetic mean of the results of Eq. 5.4 for both axes applied to all of the aforementioned intensity plots was determined to give the angle of rotation in the xy plane, ψ.

$$\psi_{S002} = (0.159 \pm 0.005)^\circ$$
$$\psi_{S003} = (0.140 \pm 0.005)^\circ$$

5.4 Radial Interaction Position

Traditionally, extraction of radial information for detectors of this type involves the anaysis of the rise time of the net charge pulse [De02, Gr05]. The concept is introduced in Section 3.4. Common charge pulse parameterisations include T90, T60 and T30, which refer to the time taken for the pulse to rise from 10 % to 90 %, 60 % and 30 % of its full magnitude. While the total rise time of the charge pulse is indicative of the

time taken for the charge carrier which takes the longest to collect, the partial rise time holds a degree of information on the shape of the charge pulse and hence the relative contribution of the two charge species. Figures 5.15, 5.16 and 5.17 show these rise time parameters averaged per xy position for each ring of S002 and S003. It should be noted that these plots are produced from events in which only one segment fires - a fold one event. Multiple hit segments can result in convoluted real and transient charge pulses, which would mask the spatial dependance of the rise time parameter.

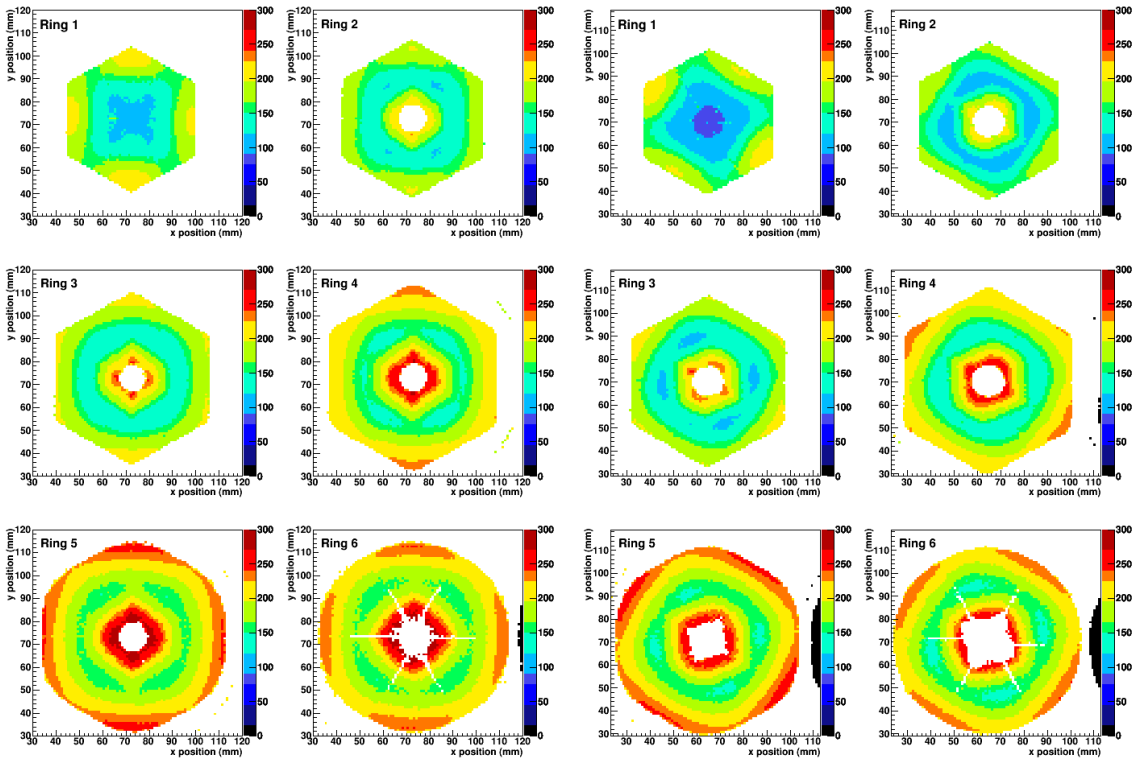

Figure 5.15: Average T90 risetime as a function of xy position for each ring of S002 (left) and S003 (right). The x and y axes denote the respective x and y positions of the collimator in millimetres. The z axis represents the T90 risetime and has units of nanoseconds.

As discussed in Section 2.4.3, the velocity of charge carriers in germanium at high electric fields is affected by the orientation of the crystal lattice with respect to the field vector. The 4-fold symmetry observed in the figures is a direct result of this and they

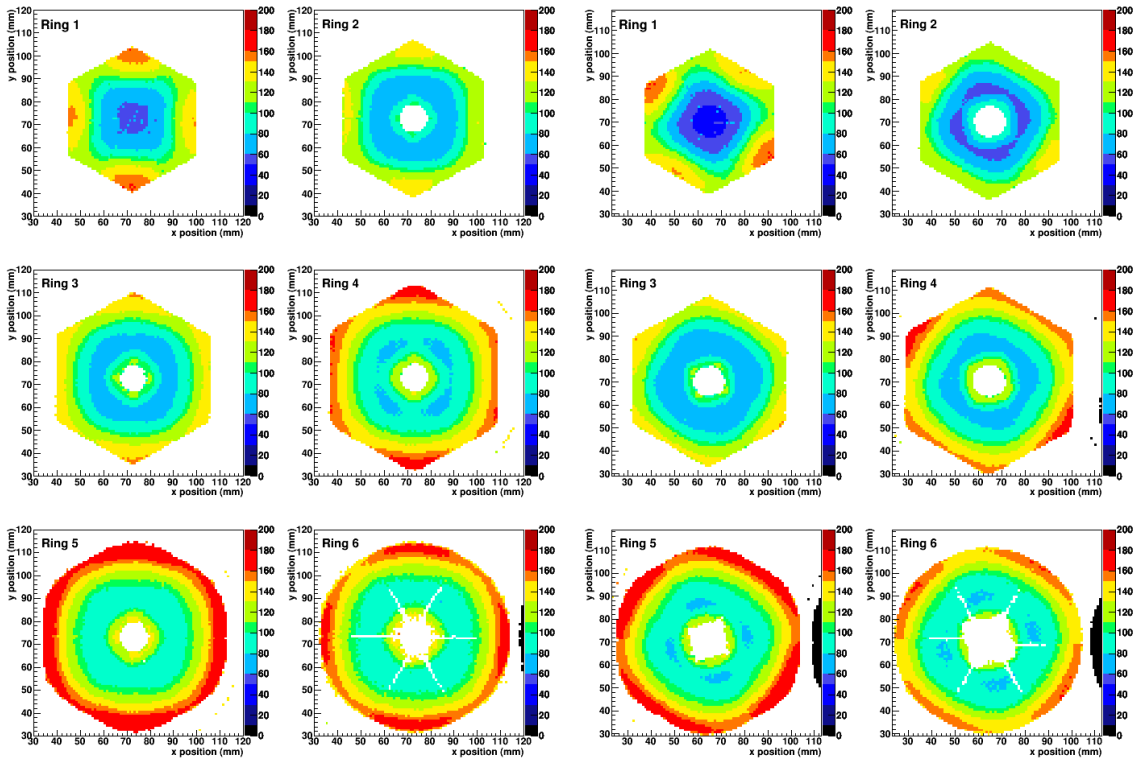

Figure 5.16: Average T60 risetime as a function of xy position for each ring of S002 (left) and S003 (right). The x and y axes denote the respective x and y positions of the collimator in millimetres. The z axis represents the T60 risetime and has units of nanoseconds.

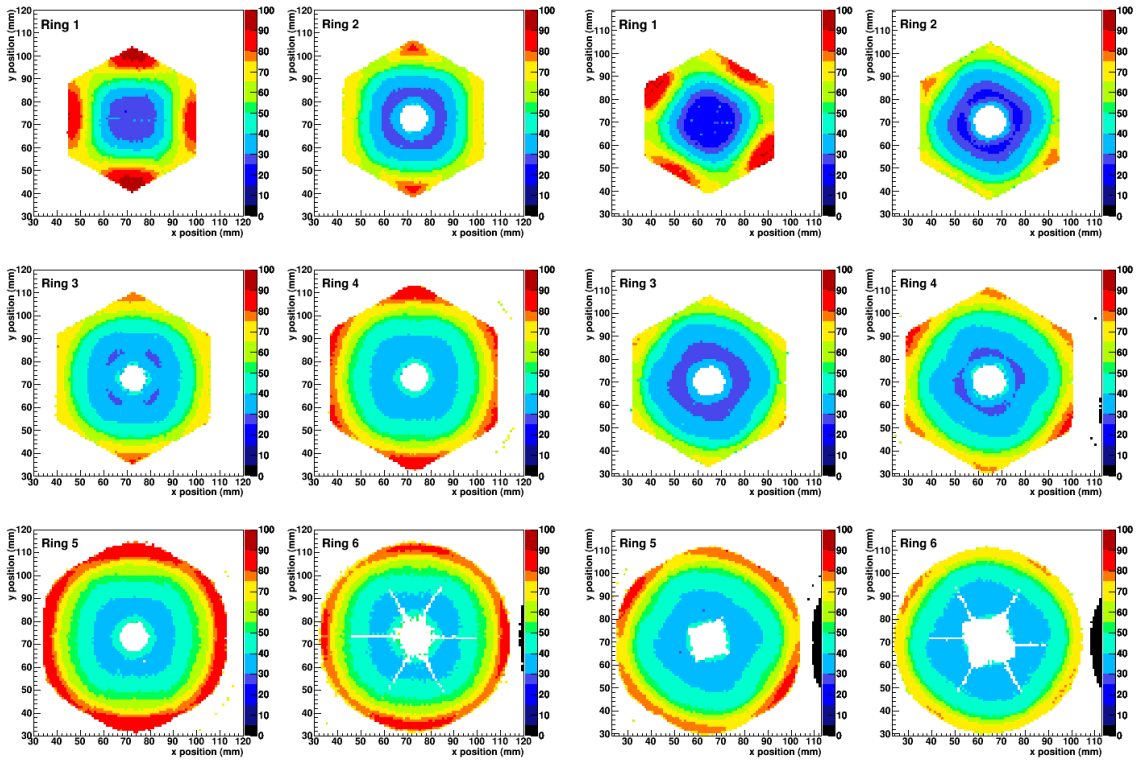

Figure 5.17: Average T30 risetime as a function of xy position for each ring of S002 (left) and S003 (right). The x and y axes denote the respective x and y positions of the collimator in millimetres. The z axis represents the T30 risetime and has units of nanoseconds.

therefore allow the lattice orientation to be inferred. The principal lattice directions are depicted in Figure 5.9. Evidently, although each of the rise time parameters varies strongly with radius, in each case the shape of the dependence is such that it has a minimum stationary point. This, in addition to the azimuthal dependance due to the crystal lattice, causes complications in determining the radius of an interaction to a significant degree of accuracy.

Given that all of the aforementioned rise time parameters suffer from the same lattice effects, in order to combat the azimuthal dependance on the risetime, one can consider a number of the risetime parameters simultaneously. A comparison is drawn between the T30 and T90 values as follows, and can be named the Rise Time Asymmetry (RTA),

$$RTA = \frac{T90 - T30}{T90 + T30} \tag{5.5}$$

This parameter, averaged per xy position, can be seen in Figure 5.18 for both prototype detectors and the absence of the crystal lattice effect can be observed. However, the relationship between this calculated parameter and radius is complicated and has many points of inflection. This is more evident in Figure 5.19.

5.5 Azimuthal Interaction Position

It is well established that the amount of charge induced on neighbouring segments to the interaction gives information on its position [De02]. This is illustrated in Section 3.4. The azimuthal angle of interaction is indicated by the relative sizes of the transient pulses from contacts in the same ring as, and adjoining, the hit segment. The total amount of charge induced on each contact during the transit time of the charge carriers is given by the total area of the induced charge pulse. It can be noted that, according to Equation 2.21, transient charges are opposite in polarity to that of the charge carrier whose motion causes it. Given that, as a result of each interaction,

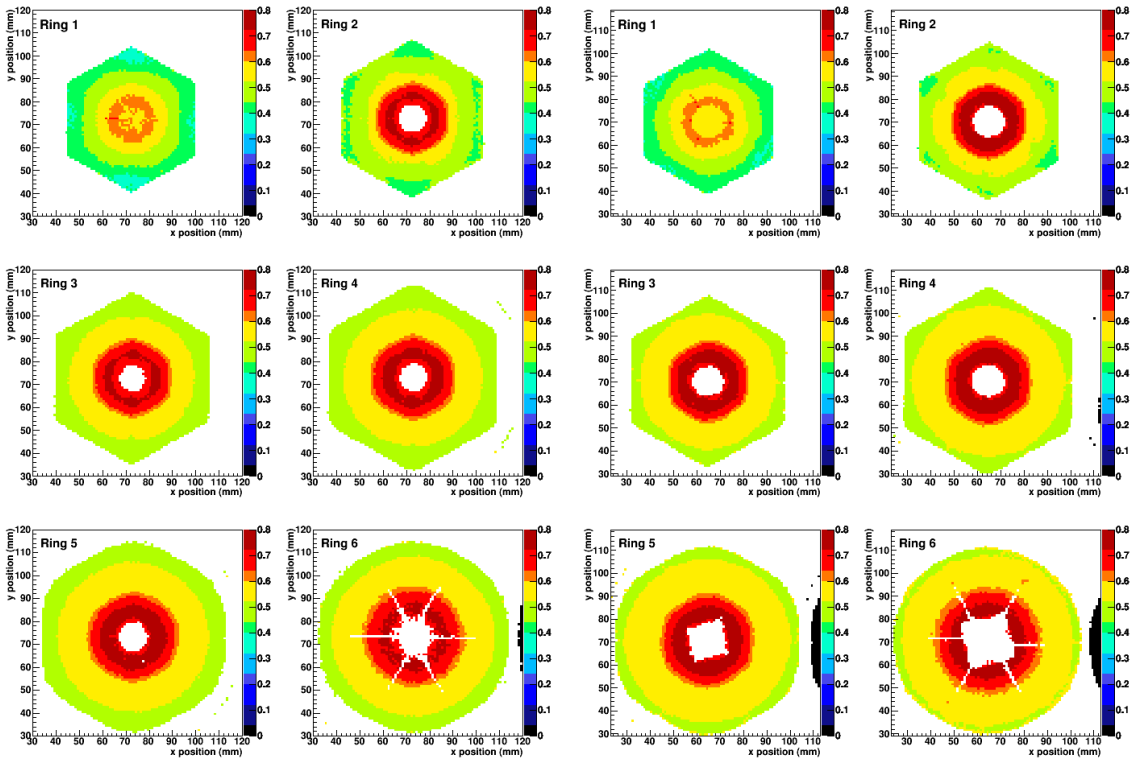

Figure 5.18: Average risetime correlation parameter as a function of xy position for each ring of S002 (left) and S003 (right). The x and y axes denote the respective x and y positions of the collimator in millimetres. The z axis has arbitrary units.

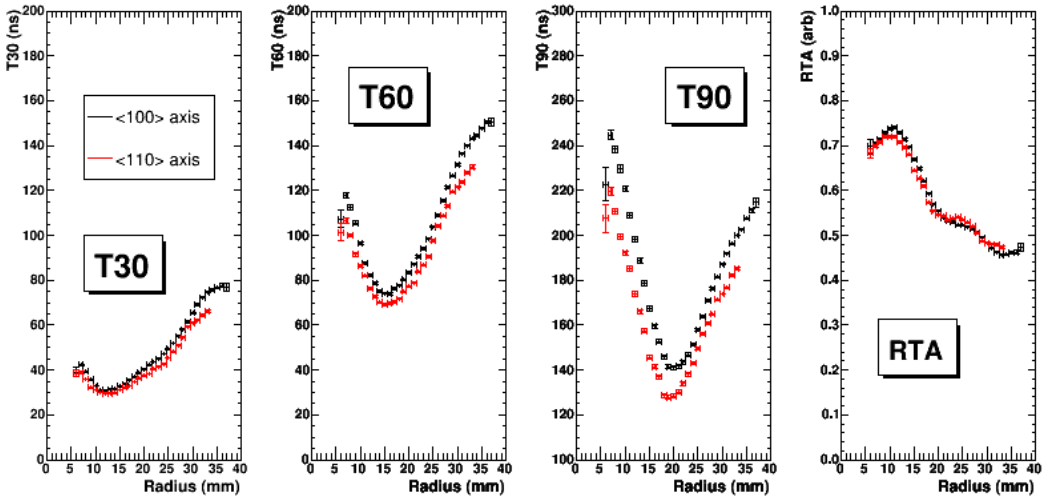

Figure 5.19: Rise time parameters as a function of radius along two of the principal crystallographic axes. A coaxial region in the third ring of the S002 detector was chosen to display the rise time parameters.

both electrons and holes are in motion, there will be a resulting positive and negative value of induced charge. Depending on the proximity of the interaction to the electric contacts, one species of charge carrier generally contributes more to the charge pulse than the other and dominates its polarity. However, there is a region approximately equidistant from the contacts in which the two charge species contribute comparably and it follows that the resulting induced charge pulses are significantly bipolar. In the worst cases, where the positive and negative components are induced simultaneously, they cancel one another out creating a region of insensitivity. In order to deal with the bipolar pulses, the modulus of the induced charge for each pulse sample is used to calculate the area of the pulse, A. The Image Charge Asymmetry, ICA, between the neighbouring segments can then be calculated according to,

$$ICA = \frac{A_{anticlockwise} - A_{clockwise}}{A_{anticlockwise} + A_{clockwise}} \tag{5.6}$$

The average ICA per xy position is plotted as a colour map in Figure 5.20 for both the S002 and S003 detectors. For the same reason as the rise time parameters, only fold one events were selected to produce these plots. Evidently the two detectors produce a similar transient response. The standard error of the mean ICA value is shown in Figure 5.21. For the bulk of the detectors, errors are small compared with the gradient of the trend itself. However, some segments display a worse performance than others and this can be loosely attributed to the noise performance of the segments from which the transients originate (Figure 4.11).

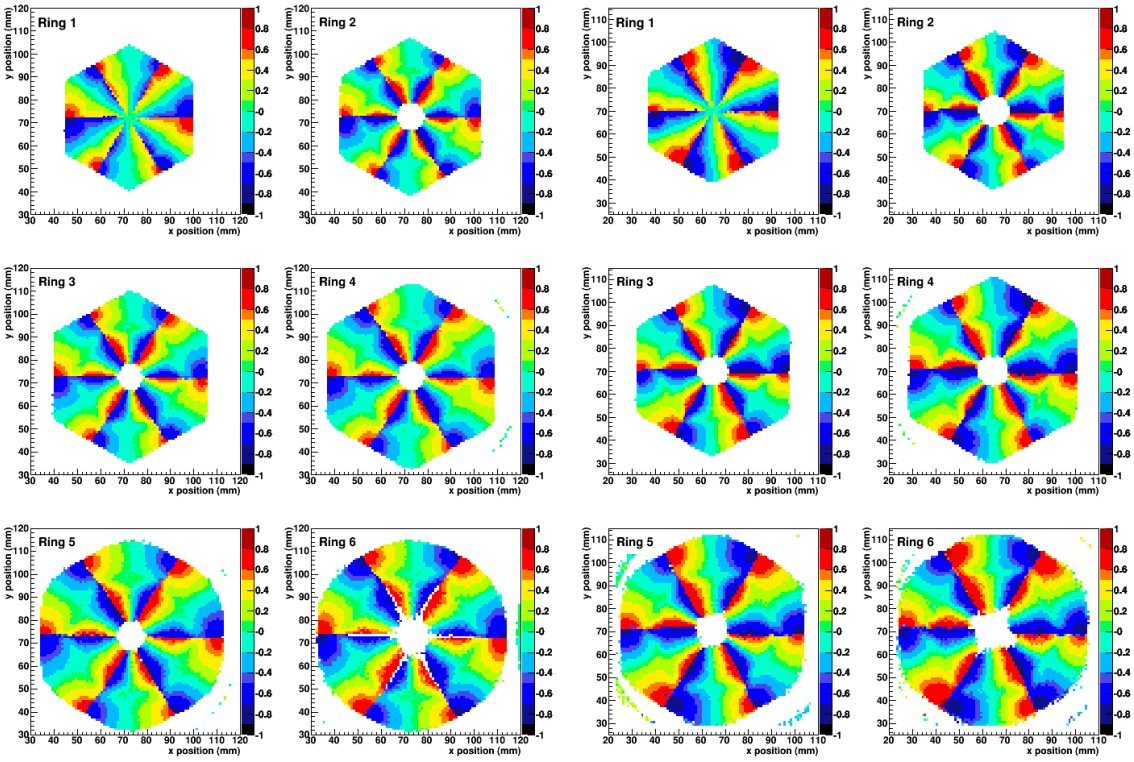

Figure 5.20: Average image charge asymmetry from neighbouring segments as a function of xy position for each ring of S002 (left) and S003 (right). The x and y axes denote the respective x and y positions of the collimator in millimetres. The z axis has arbitrary units.

The azimuthal variation of ICA is clear and is investigated further in Figure 5.22. There is an approximately linear dependence of ICA with azimuth for a large part of

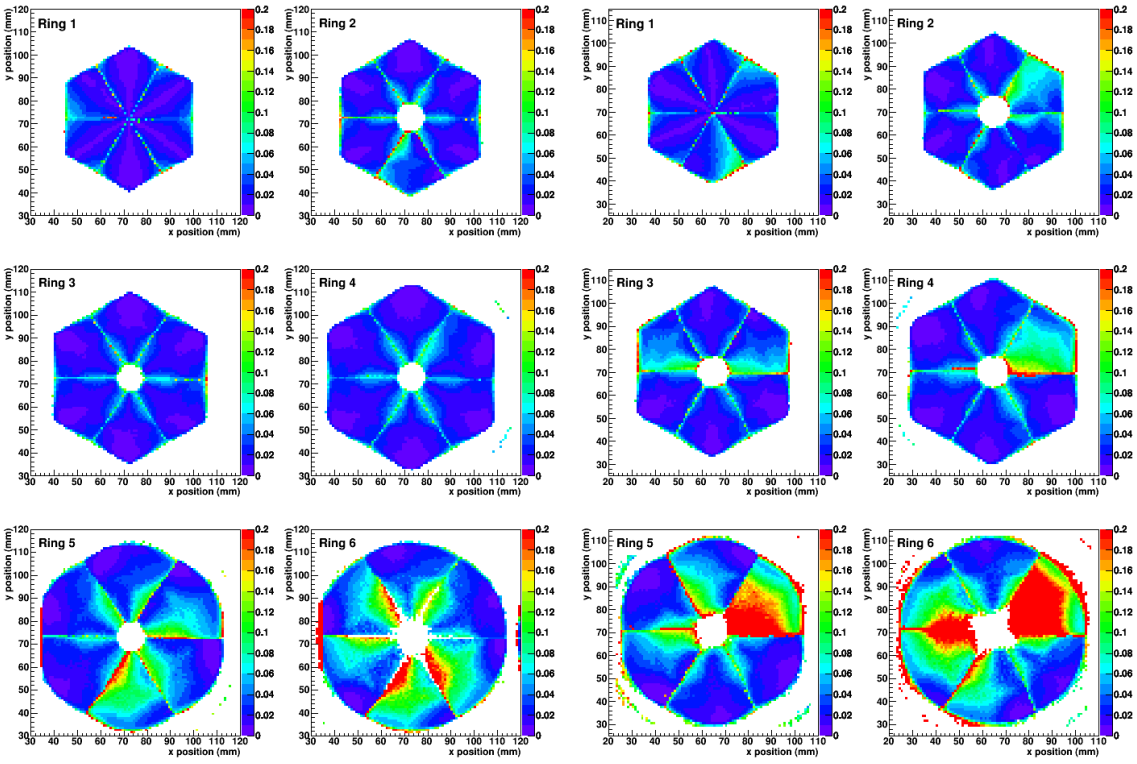

Figure 5.21: Standard error on the average image charge asymmetry from neighbouring segments as a function of xy position for each ring of S002 (left) and S003 (right). The x and y axes denote the respective x and y positions of the collimator in millimetres. The z axis has arbitrary units.

the segment but, close to mid-radii, this relationship does not hold. This is the case between $r\approx$20 mm and $r\approx$25 mm- closer to the outer electrode due to the greater velocity of electrons, which drift toward the anode, than holes. Evidently, ICA depends on the radius of the interaction as well as its azimuthal angle. Furthermore the ICA as a function of azimuth can not be regarded as truely linear and this is particularly evident at larger radii in Figure 5.22. Third order polynomial fits are applied to the data in this figure and are also displayed. Although the fits approximate fairly well, some sensitivity is still lost at mid-radii and mid-azimuth.

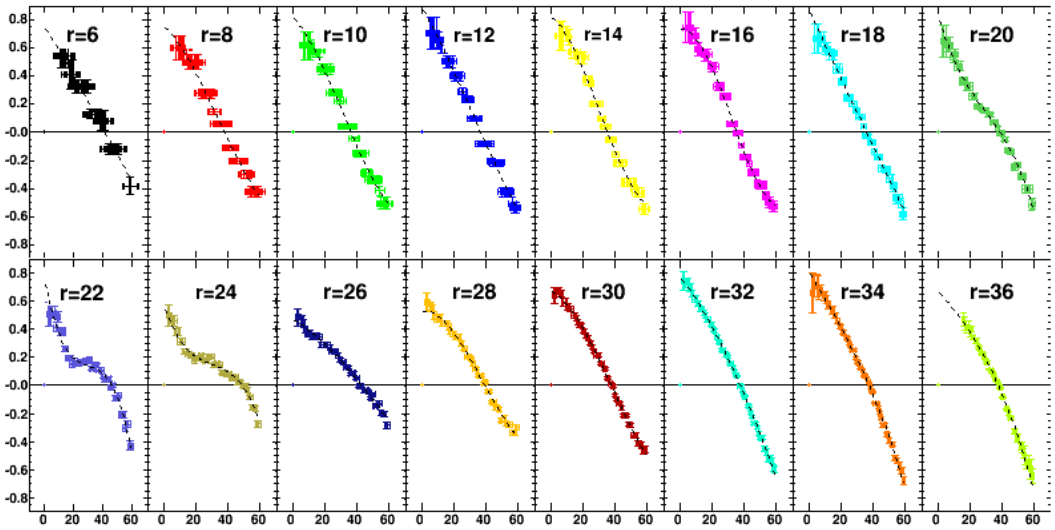

Figure 5.22: Average ICA as a function of angle of azimuth for various radii of segment C4 of S002. For each plot the x-axis shows the azimuthal angle across the segment (in degrees) and the y-axis shows the average ICA in arbitrary units. The duplicate values across many angles at small radii are explained by the scan step lenth of 1 mm and consequently the relatively large angular range per collimator position at these radii. Third order polynomial fits are also displayed on the plots as dotted black lines.

5.6 Spatial Calibration of S002

The rise time and image charge parameters of the S002 detector, as discussed in Sections 5.4 and 5.5, are used to create a spatial calibration based on polynomial fitting of the averaged parameters. As these parameterisations were produced from fold one events only, no attempt was made to find the xy locations of multiple fold events. The frequencies of segment fold events for the S002 detector are plotted in Figure 5.23. Out of ∼26 million events from the S002 front face singles scan, 33 % are fold one events.

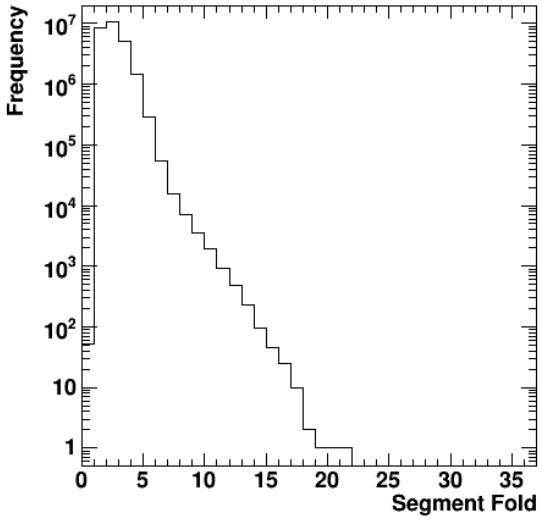

Figure 5.23: Frequency of segment folds from the front face singles scan of the S002 detector.

Determination of the xy location of an event is achieved by way of the following steps:

1. Fifth order polynomial fits of the rise time parameters T30, T60, T90 and RTA as a function of radius are produced using the bin contents of Figures 5.17, 5.16, 5.15 and 5.18. All azimuthal angles are taken into account resulting in one fit of each parameter for each ring.

2. The radii at which the stationary points of each of these curves occur are found.

3. The rise time parameters of the core pulse (T30, T60, T90 and RTA) for each fold one interaction are calculated and compared to the fits either side of the stationary points. A variable sized set of possible radii is produced.

4. A weighted arithmetic mean of this array is calculated, such that the values of the radius calculated using the RTA had twice the importance of the other values. This weighting was applied so that the incorrect root of each of the rise time curves would be eliminated as the roots of the RTA are more likely to be localised to the true radius.

5. The member of the set which deviates greatest from the mean is rejected and this is repeated successively until there are four possible radii left in the set. The arithmetic mean of the remaining set members is returned as the radius of the interaction. However, as the aforementioned fits are averaged over all azimuthal angles and large variation in the dimension exists, this radius is regarded as a first approximation.

6. Third order polynomial fits of the image charge asymmetry as a function of azimuthal angle are produced using the bin contents of Figure 5.20. As there are large deviations in the shapes of the curves with radius, a fit is created for every integer radius value. This is done for each segment as there are small deviations, which are largely due to the crystal lattice orientation.

7. The image charge asymmetry of the fold one event is calculated and compared to the fit pertaining to the hit segment and first approximation radius. The azimuthal angle at which the ICA of the interaction fits the curve is returned.

8. An additional set of polynomial fits of the T30 and T90 rise time parameters is produced in the same way as detailed in Step 1 but for each azimuthal angle

of each segment. The radius of each interaction is calculated again by following Steps 2 to 5 with the new fits for the T30 and T90 parameters only.

9. Step 7 is repeated with the new radius to determine the azimuthal angle of the interaction more precisely.

This method was derived after many attempts to accurately determine the interaction locations. In these trials, different approaches to the steps outlined above were tested, such as the number of risetime parameters used, the weighting applied and the elimination method of incorrect roots of ths risetime fits. The method discussed here was found to give the most accurate results, determinable by Figure 5.26. The procedure was applied to the front face singles scan data of both the S002 and S003 detectors, using the same S002 calibration for each. This provides a means to test the reproduciblity of the method between crystals.

5.6.1 Application to the S002 Scan Data

The results of applying the algorithm described in the previous section to the S002 scan data are detailed in the following figures. It should be remembered that the polynomial fits of the pulse shape parameterisations are produced from averaged results of this data set and therefore do not test the full capability of the method. Figure 5.24 shows both the radial and azimuthal precision of the algorithm for each ring of S002. This is produced by binning each event according to the modulus of the difference between the algorithm calculated radius (or azimuthal angle) and that given by the collimator position. The figure shows that the calculated radius of ∼27 % of events is correct to within 1 mm and ∼82 % of events are correct to within 5 mm. For the azimuthal angle, ∼12 % of events lie within 1° of the collimater position and ∼80 % of events are correct to within 10°. The sixth ring produces the worst precision in radius, and this is likely to be a result of the poor statistics acquired in this region of the detector. This is partly due to attenuation of the photon beam throughout the

length of the detector but also due to the inhomogenous electric field caused by the contacts abrupt end, despite the passivated layer of germanium at the back of the crystal. The second ring is also problematic in radius due to the effects of the electric field caused by the end of the anode.

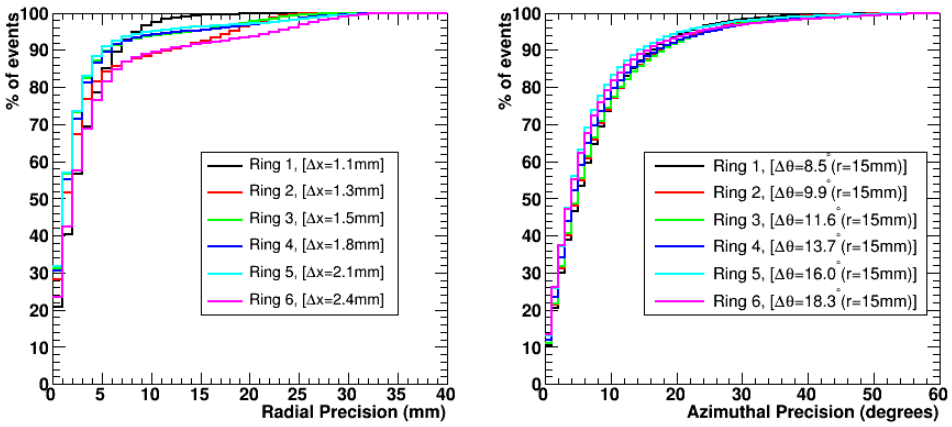

Figure 5.24: Radial and azimuthal precision of the spatial calibration applied to the S002 detector. An indication of the uncertainty of the collimator position is also given in terms of radius and angle for each ring. This is merely calculated from the geometric divergence of the photon beam and therefore increases with depth into the crystal. However the angular range of the beam divergence also depends on the radius of the interation and the uncertaintly in angle is thus given at a fixed radius of 15 mm, but can be much larger at smaller radii.

Figure 5.25 shows the effect of the two iterations of the algorithm on the precision achieved, the first iteration being up to Step 7 in the preceding algorithm description and the second uses the refined coordinates. The plot shows the results for the third ring only, the trend is similar for all other rings. The second iteration shows a significant improvement to the radial precision.

In order to determine areas of the detector which are problematic to the algorithm, the average difference between the calculated and known dimension can be plotted

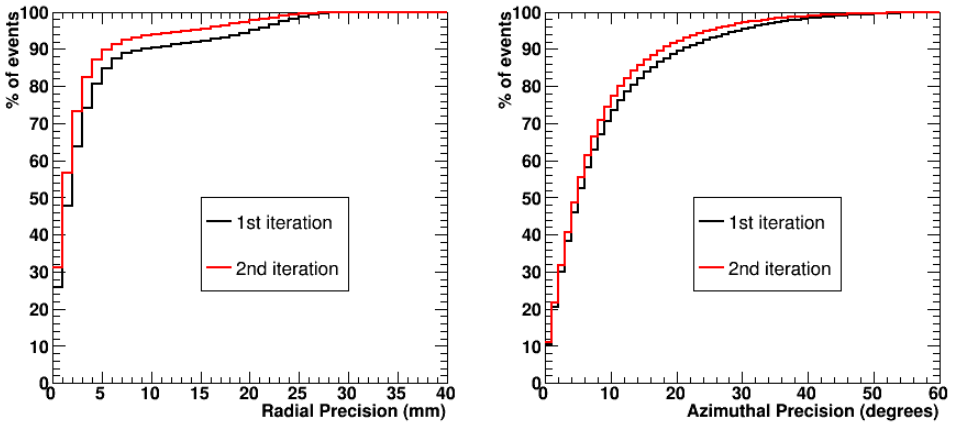

Figure 5.25: Radial and azimuthal precision achieved in the third ring of the S002 detector at two stages of the position determination process. The figure is discussed in more detail in the main body of text.

as a function of xy position. This can be seen in the left plot of Figure 5.26 for the interaction radius, and in the right plot for its azimuthal angle. Extreme radii produce the biggest problem for radial position information, while mid-radii regions consistently demonstrate the worst precision in azimuthal angle.

Upon consideration of the standard deviation of radial and azimuthal parameters as a function of position, it can be seen that the areas with large error in dimension determination, visible in Figure 5.26, do not correspond to areas with the greatest deviation from the mean. The standard deviation of T90 and ICA can be seen in Figure 5.27. It can be concluded that the largest uncertainty in position determination is caused by the inadequacy of the algorithm, derived from poor fitting of the complicated parameter distributions. The fact that standard deviations are low throughout the bulk of the detectors is a significant point. It can be seen from Figure 2.1 that, at a photon energy of 662 keV, Compton scattering is the dominant interaction mechanism and multiple site interactions are expected within a detecting volume. Due to the random nature of the scattering sequences, they will not be evident in the average

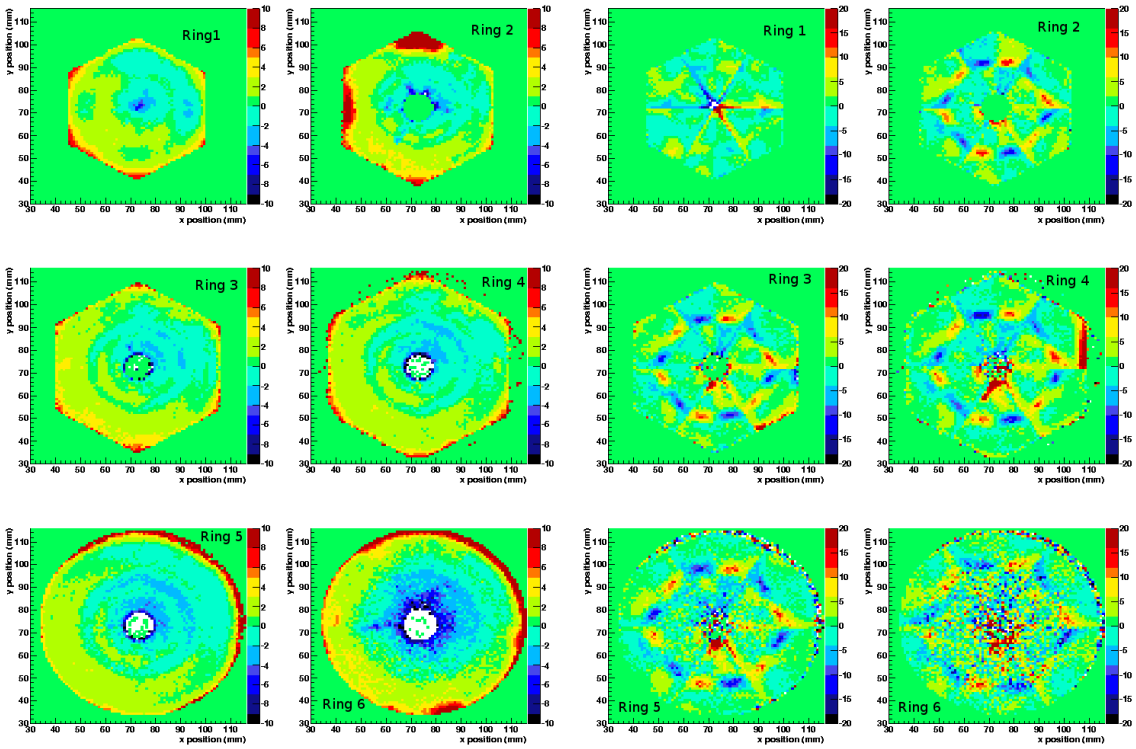

Figure 5.26: Average difference between the calculated radius and that given by the collimator position (*left*) and the calculated azimuthal angle and that given by the collimator position (*right*) as a funtion of xy position for each ring of S002. The x and y axes denote the respective x and y positions of the collimator in millimetres. The z axis represents the aforementioned difference and also has units of millimetres (*left*) or degrees (*right*).

pulse shape parameters but are expected to cause large standard deviations. The low standard deviations elude to the fact that the pulse shapes are not greatly affected by in-segment scattering.

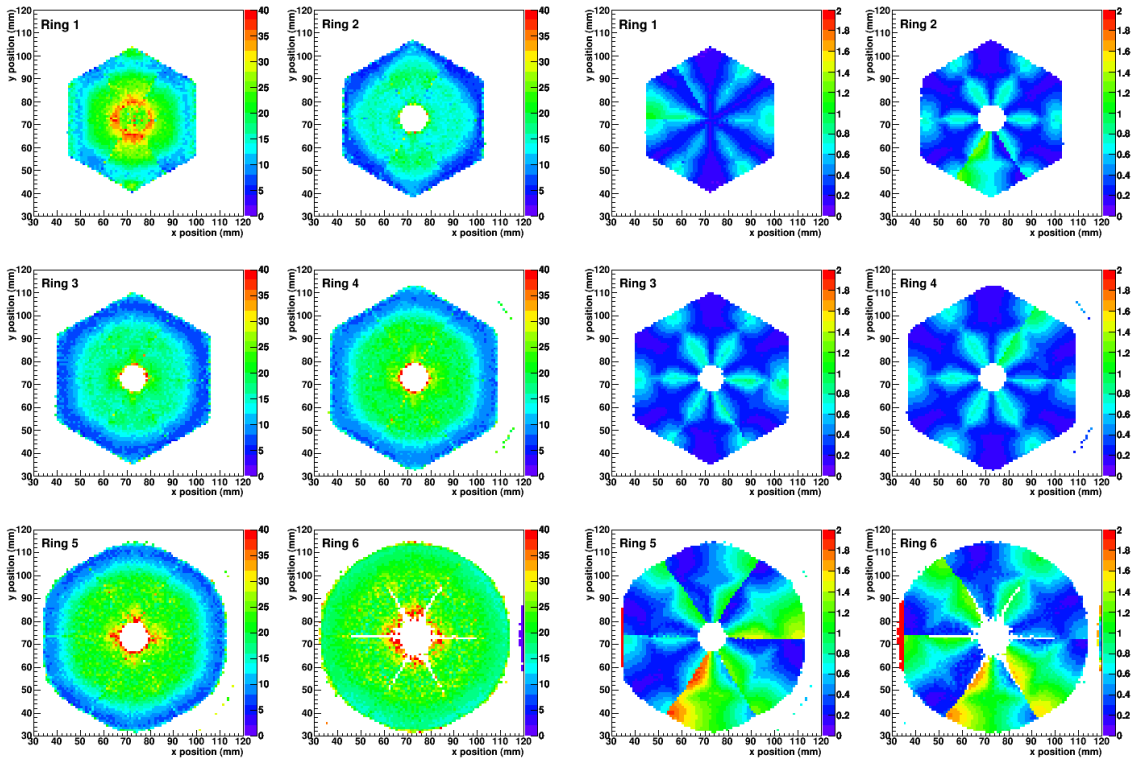

Figure 5.27: Standard deviation of the T90 risetime (*left*) and the ICA (*right*) as a funtion of xy position for each ring of S002. The x and y axes denote the respective x and y positions of the collimator in millimetres. The z axes have the same units as the parameters themselves, namely; nanoseconds (*left*) and arbitrary units (*right*).

5.6.2 Application to the S003 Scan Data

The spatial calibration of the S002 detector was applied to the data set obtained from the S003 front face scan, the results of which are summarised by the following figures. The pulse shape parameterisations of the S003 data were, where appropriate, compared to the S002 polynomial fits which matched the lattice orientation and not

the physical segmentation. Figure 5.28 shows that ∼17 % of events have a calculated radius correct to within 1 mm (∼27 % for S002) and ∼69 % are within 5 mm (∼82 % for S002). Only ∼9 % are correct to within 1° (∼12 % for S002) and ∼70 % of events have a precision of less than 10° (∼80 % for S002). Rings 1 and 6 produce the worst results in contrast to rings 2 and 6 for the S002 detector. Figure 5.29 shows the result of the two iterations of the algorithm, and is analogous to Figure 5.25 for the S002 detector. It can be seen that the impovement to the radial precision due to the second iteration is large compared with that achieved for the S002 detector, and again this pattern is repeated for all rings.

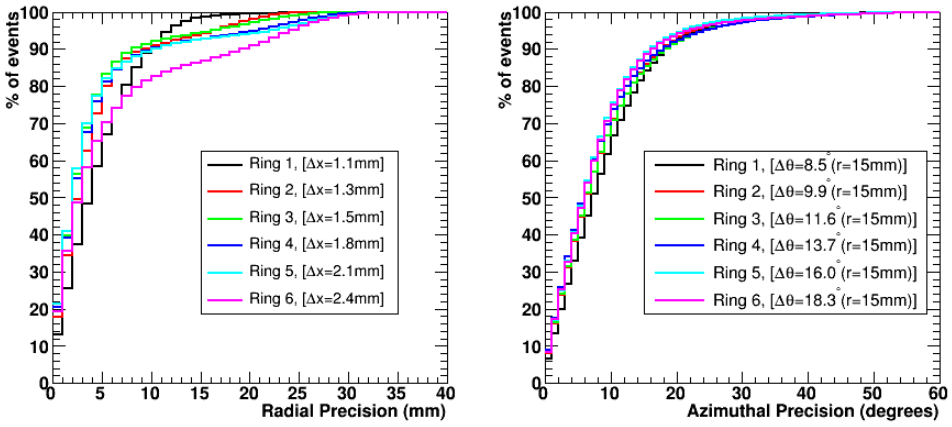

Figure 5.28: Radial and azimuthal precision of the spatial calibration applied to the S003 detector. See Figure 5.24 for more information.

The problematic areas of the S003 detector are plotted, as for the S002 data, as a function of xy position for each ring in Figure 5.30.

5.6.3 Comparison of Results

The deviations of the calculated x and y spatial coordinates, derived from r and θ values, from the collimator position are plotted for both detectors in Figures 5.31

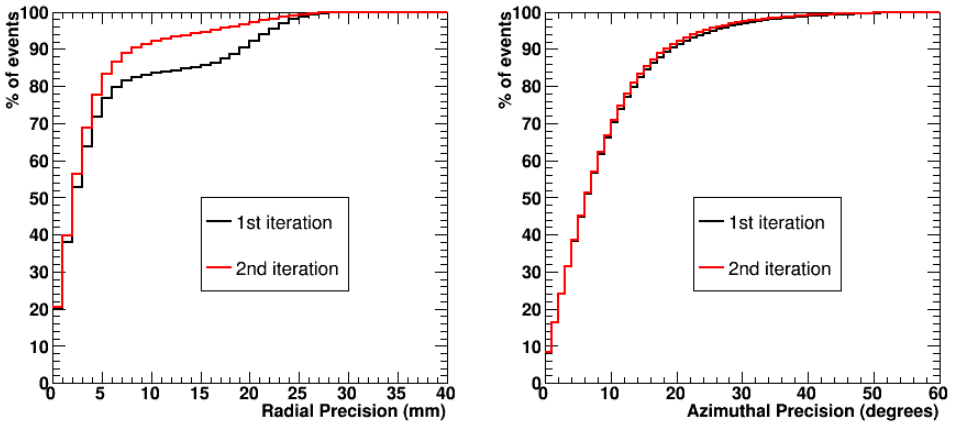

Figure 5.29: Radial and azimuthal precision achieved in the third ring of the S003 detector at two stages of the position determination process. The figure is discussed in more detail in the main body of text.

and 5.32. The plots were fitted with a skewed Gaussian and the resulting FWHM of each ring of each detector for each of the x and y dimensions is displayed on the figures. This gives an indication of the spatial resolution achievable with the present calibration. Averaged over all rings and both x and y dimensions, the resolution is 5.0 mm for the S002 detector and 9.3 mm for the S003 detector. The difference in the results of the two detectors are attributed to slight differences in the parameter trends observable from the polar risetime and ICA plots in Sections 5.4 and 5.5. In turn, these differing trends are likely to be caused by the different impurity concentration values of each crystal and their resulting operating voltages.

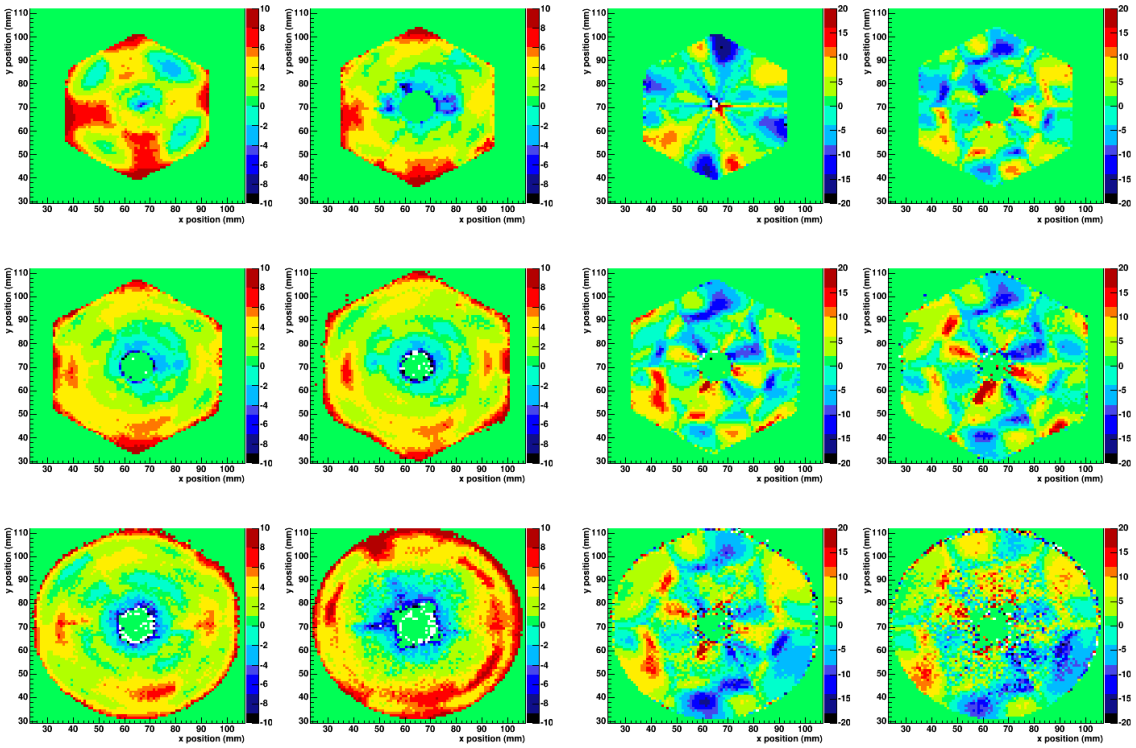

Figure 5.30: Average difference between the calculated radius and that given by the collimator position (*left*) and the calculated azimuthal angle and that given by the collimator position (*right*) as a funtion of xy position for each ring of S003. The x and y axes denote the respective x and y positions of the collimator in millimetres. The z axis represents the aforementioned difference and also has units of millimetres (*left*) or degrees (*right*).

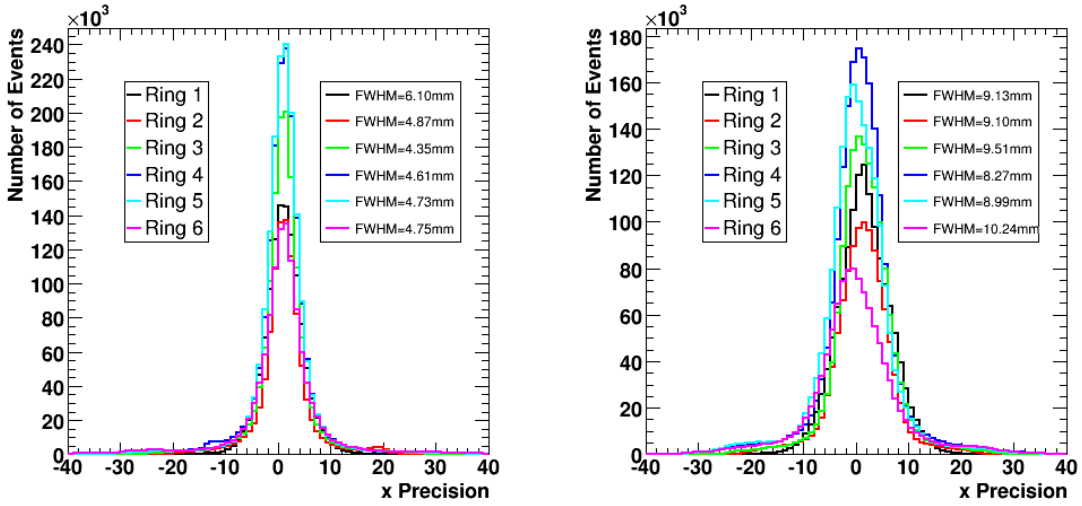

Figure 5.31: Precision in the x dimension for the spatial calibration applied to both the S002 (left) and S003 detectors (right). The FWHM of each plot is also displayed.

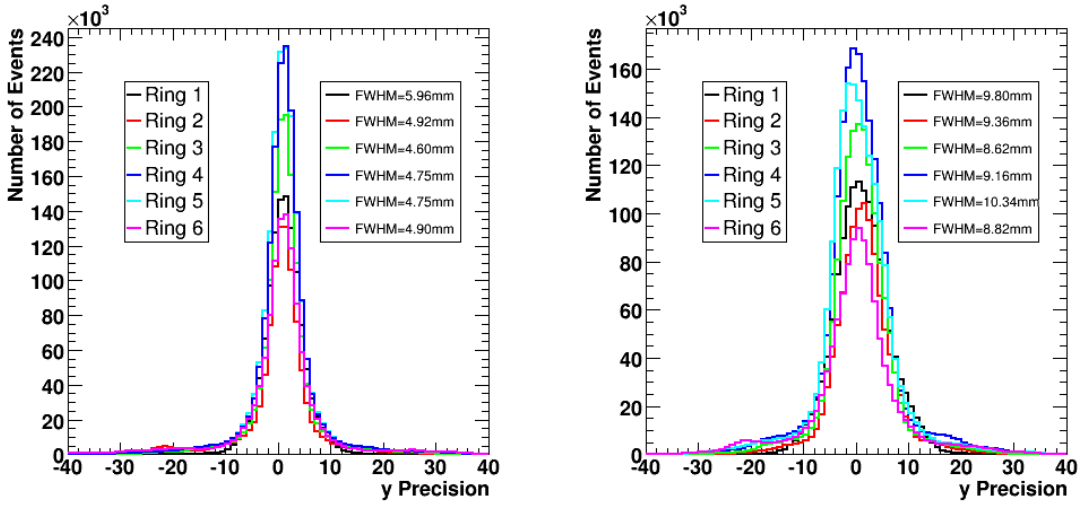

Figure 5.32: Precision in the y dimension for the spatial calibration applied to both the S002 (left) and S003 detectors (right). The FWHM of each plot is also displayed.

Chapter 6

Experimental Data

The three symmetric prototype AGATA detectors (S001, S002 and S003) were placed in a triple cluster cryostat for an in-beam experiment in the Summer of 2005. The beam was provided by the tandem accelerator at the *Institut für Kernphysik* at the University of Köln. The experiment was proposed and conducted by the AGATA collaboration [AG03] and its purpose was to assess the performance of the detectors in a comparable environment to which they are intended to be used. It provides a situation in which to test the functionality of PSA algorithms (see Section 3.4). The triple cluster was placed at 90° to the beam line to maximise Doppler broadening of the γ-spectra obtained and allow for a significant improvement to the resolution achieved. A ^{48}Ti beam at 100 MeV was incident on a deuterated natural Titanium target (220 μgcm^{-2}) creating a mixture of reaction channels, namely; one-nucleon transfer, Coulomb excitation and Fusion-Evaporation, with a typical recoil velocity of $v/c \approx 6.5$ %.

6.1 Particulars of the Experimental Setup

6.1.1 AGATA Detectors

The three AGATA detectors are labelled α (S001), β (S002) and γ (S003). The orientation of the detectors within the common cryostat can be seen in Figure 6.1. A photograph of the cryostat in place for the experiment can be seen in Figure 6.2. The precise values of the angles made by each detector with the laboratory coordinate axes[1] are listed in Table 6.1. These values derive from coordinates of the triple cluster calculated by F. Recchia using minimisation routines of the offline dataset [Re06][2].

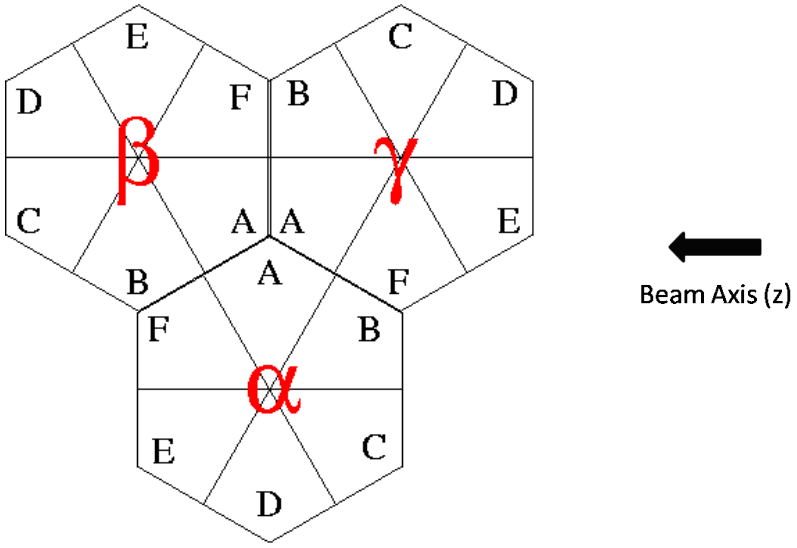

Figure 6.1: AGATA triple cluster detector labelling and orientation as viewed from the target position (looking along the negative y-axis in the laboratory coordinate system).

[1] In the laboratory coordinate system, the z-axis is in the direction of the beam line, the x-axis points vertically downwards to the laboratory floor and the y-axis is horizontal. See Figure 6.6 for further details.

[2] The point at which the front faces of the three detectors are closest (the midpoint of Figure 6.1) is defined using a combination of x, y and z dimensions as well as angles of the clusters' rotation about the coordinate axes.

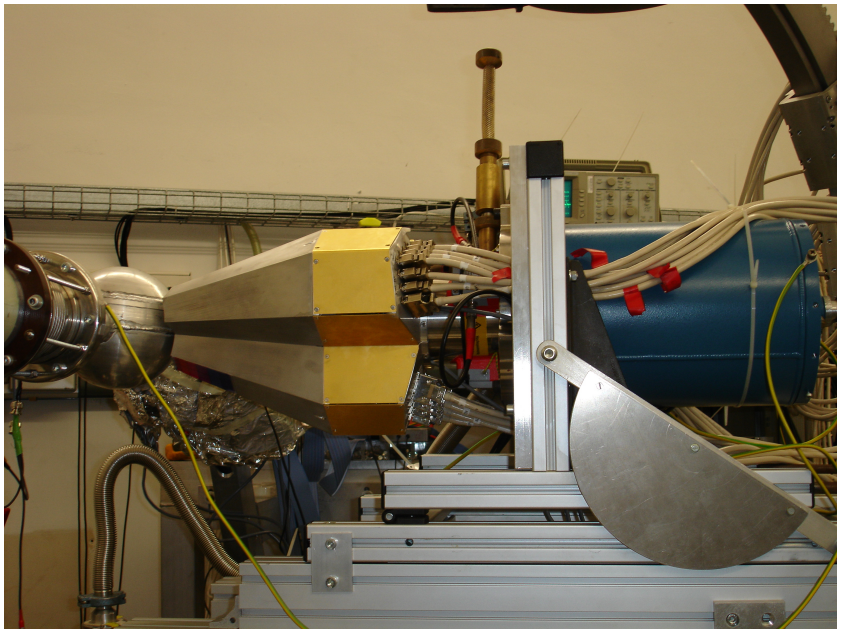

Figure 6.2: Photograph of the AGATA triple cluster in place for the in-beam experiment. The incident beam line can be seen to the left of the figure as can the target chamber containing the DSSSD (discussed in Section 6.1.2).

Detector	θ	ϕ
α	88.5°	-18.6°
β	75.7°	4.0°
γ	103.1°	4.5°

Table 6.1: The angle made by the centre of each detector and the beam line in the zy plane, θ, and by the centre of each detector and the y-axis in the yx plane, ϕ.

6.1.2 Particle Detector

An annular Double Sided Silicon Strip Detector (DSSSD) was used in the experiment to detect the angle and energy of the recoils produced such that the Doppler correction can be as precise as possible. The DSSSD was segmented into 64 sectors on one side and 32 rings on the other. A photograph of the DSSSD, which was operated within the vacuum of the target chamber, can be seen in Figure 6.3. Its dimensions and labelling scheme can be seen in Figure 6.4. Unfortunately this detector was not precisely aligned with the beam axis. This is visible from the non-unifrom intensity across sectors in Figure 6.5. The extent of the mis-alignment was calculated, as for the triple cluster coordinates, by F. Recchia [Re06] and is quantified in Figure 6.4. The DSSSD was 300 μm thick and a 16 μm thick Aluminium absorber was used directly in front of it to slow the recoils. A schematic representation of both the Si and Ge detectors can be seen in Figure 6.6 in the laboratory coordinate system. The Silicon detector was calibrated in energy using an α-source by F. Recchia [Re07b].

6.1.3 Data Acquisition and Presorting

The output of each of the 111 germanium channels was connected to the CWC converter boxes in order to convert from differential to single-ended signals. The signals were then input to DGF-4 digitising modules, made by XIA [Xi08], which sampled with a 14 bit FADC and a 40 MHz clock frequency. The trace length provided by the cards was 80 samples (2 μs). The three core signals were also input to analogue electronics in order to provide a trigger for the data acquisition. A logical OR was used between these 3 signals followed by an AND gate combining this and information from the Si detector. A schematic illustration of the trigger can be seen in Figure 6.7. The trigger was inhibited whilst the digitisers processed the Ge signals; the slow data rate and the large numbers of signals processed limited the trigger rate achieved. This contributed to the low statistics observable in the following analyses.

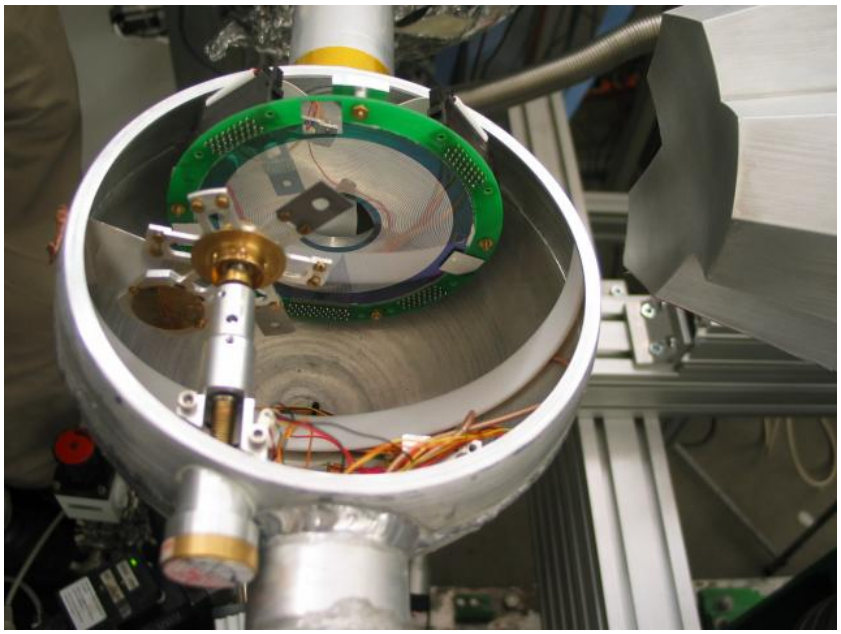

Figure 6.3: Photograph of the inside of the target chamber. The target holder and DSSSD can both be seen. Also visible to the right of the photograph is the front face of the triple cryostat.

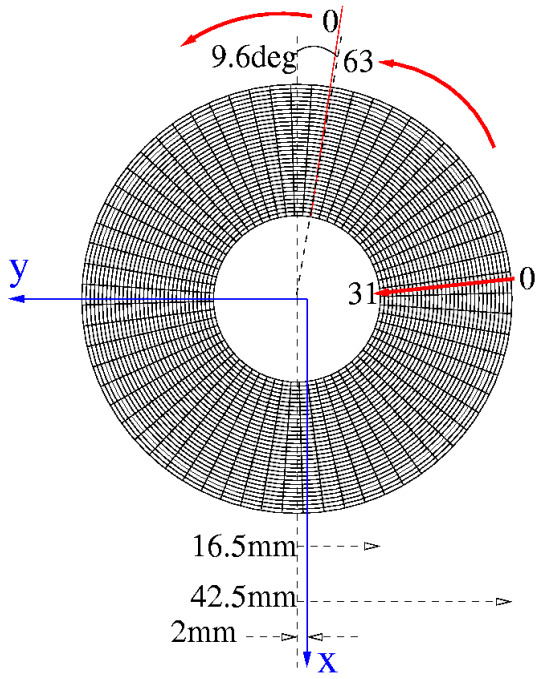

Figure 6.4: Dimensions and segmentation of the DSSSD. The schematic diagram also shows the detectors' positioning with respect to the laboratory coordinate axes in the xy plane. As for the triple cluster, the coordinates of the Silicon detector are provided by [Re06]. Not apparent in the diagram is the DSSSD's z position. The reader is referred to Figure 6.6 for further information. The sectors are labeled 0-63 in an anti-clockwise direction and the rings are labeled 0-31 from the outer ring to the inner. The offset of the detector's centre with the co-ordinate axis is discussed in the main text.

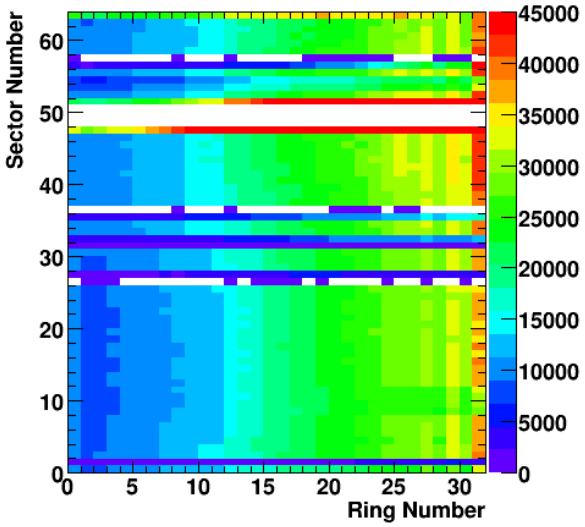

Figure 6.5: Intensity map for single pixel events (1 segment and 1 ring firing in coincidence) in the Silicon detector. A number of sectors were missing from the experimental dataset. As the sizes of the pixels, and therefore the number of particles detected, vary with ring number, the number of interactions is normalised to its size. An indication of the mis-alignment is visible. It can be noted that this plot supports the notion that the outermost ring is labelled 0 whilst the innermost ring is 31 - one would expect there to more interactions closest to the beam axis.

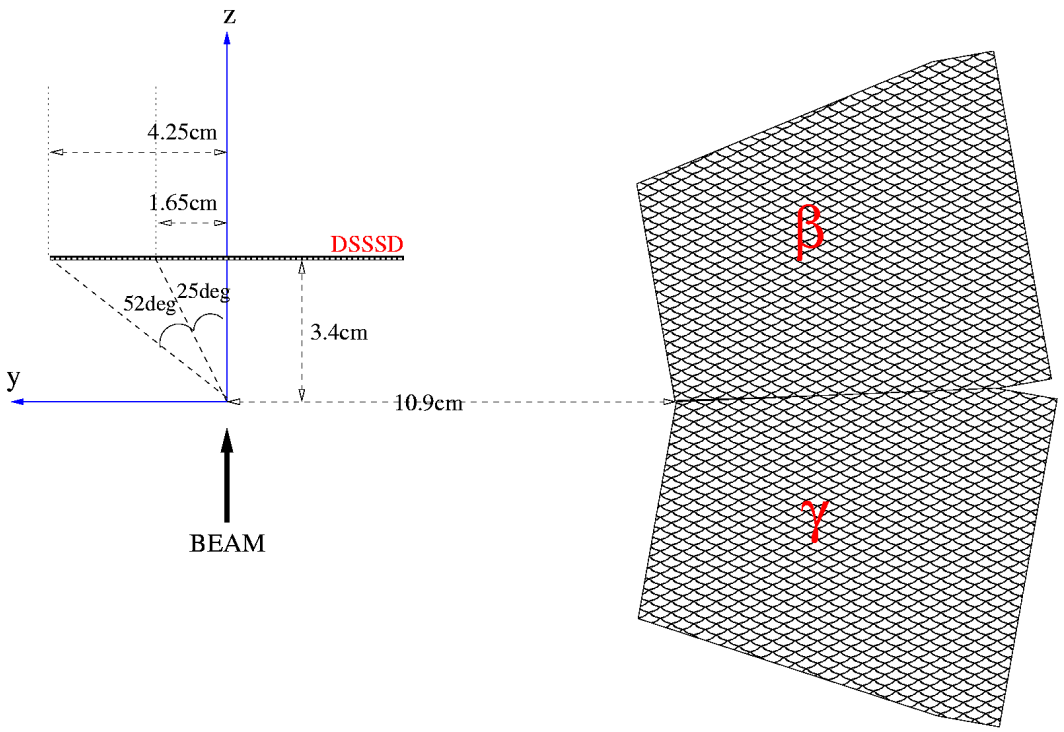

Figure 6.6: Schematic of the laboratory coordinate system as seen from above. The x-axis points vertically down to the laboratory floor (into the page in the figure). The angular range of the DSSSD can also be seen. Only the β and γ detectors are visible from this view, α is directly underneath them. It should be noted that the DSSSD is not precisely aligned with the target position in the xy plane; this is not visible in the figure. Figure 6.4 depicts and quantifies the offset.

Over ∼12 days of beam time, ∼1 TB of data was written to 25 SDLT tapes in GSI format, however only 16 of these tapes contained usable run data[3]. The data set used in this work was presorted to 86 GB in ROOT tree format [RO07] by F. Recchia [Re07b] and contained ∼22 million events. It can also be noted that, in the presorting process, the events of this data set were separated according to the three independent crystals and it was not possible to recombine events in which multiple crystals were hit in coincidence.

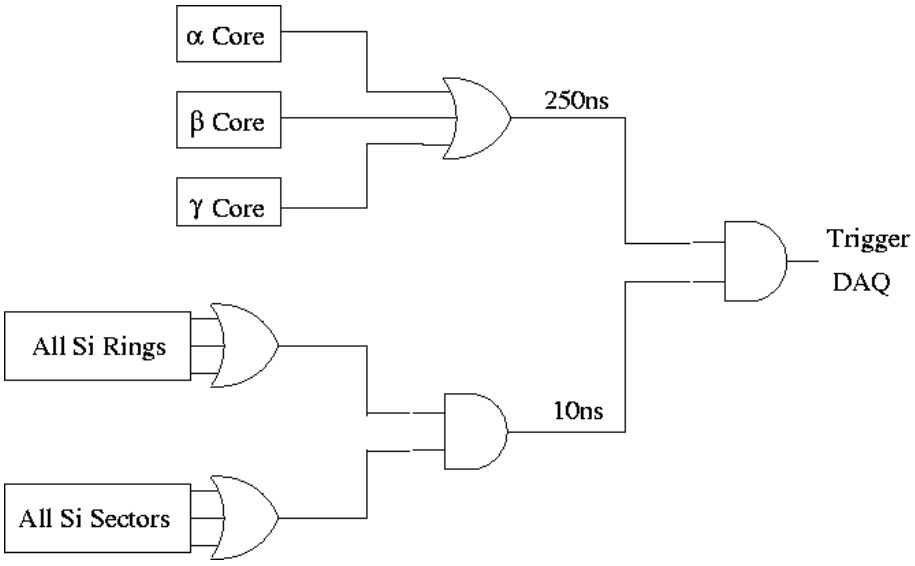

Figure 6.7: Schematic diagram of the data acquisition trigger.

6.2 Energy Calibration

There was limited usable calibration data available from the experiment. In the presorted dataset, tapes 21 and 22 contained data collected in the germanium detectors from a ^{60}Co source and this was used to calibrate the 111 AGATA channels. The calibrated energy spectra of the three core channels from tape 21 are displayed in

[3]In addition to a number of the tapes containing calibration and singles data, the target and beam energy were changed during the experiment rendering some of the tapes unusable.

Figure 6.8 and the corresponding energy resolutions from the ^{60}Co peaks can be seen in Table 6.2.

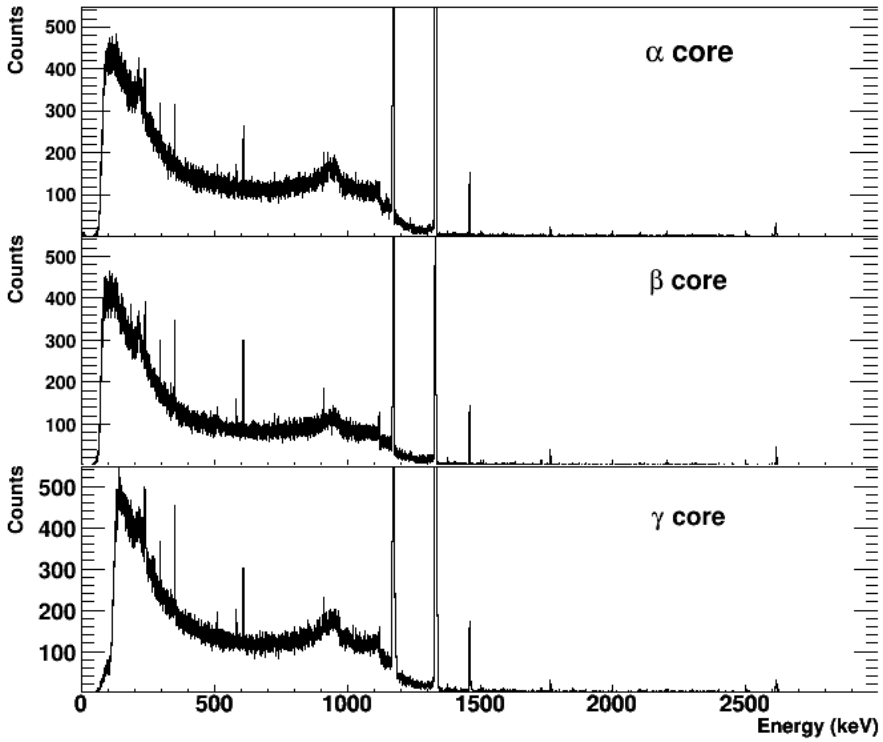

Figure 6.8: Calibrated ^{60}Co spectra of the three AGATA core contacts from tape 21. The spectra have 16k bins in total with ∼0.3 keV/channel.

Unfortunately the electronics were unstable and some channels drifted significantly during the time of the experiment. An attempt was made to quantify the drift between the calibration tapes and to determine whether an energy dependence was present. The peaks belonging to the ^{60}Co source and any other peaks from the natural background present in the spectra were used for this study and are detailed in Table 6.3. The drift between tapes 21 and 22 of the β detector's core channel can be seen in Figure 6.9. Due to the sporadic nature of the data points and the large error bars associated with most peaks, no suitable fit of the data could be achieved and an energy dependent drift of the electronics was not considered in the subsequent analysis.

Detector	Resolution at 1173keV (keV)	Resolution at 1332keV (keV)
α(S001)	3.03	3.26
β(S002)	2.64	2.82
γ(S003)	3.55	3.75

Table 6.2: Energy resolution achieved for the three core channels using a ^{60}Co source.

Peak Energy (keV)	Origin	Peak Energy (keV)	Origin
295	^{214}Pb	1173	^{60}Co source
352	^{214}Pb	1332	^{60}Co source
511	annihilation	1460	^{40}K
583	^{208}Tl	1764	^{214}Bi
609	^{214}Bi	2614	^{208}Tl
911	^{228}Ac		

Table 6.3: Peaks present in the calibration spectra of tapes 21 and 22.

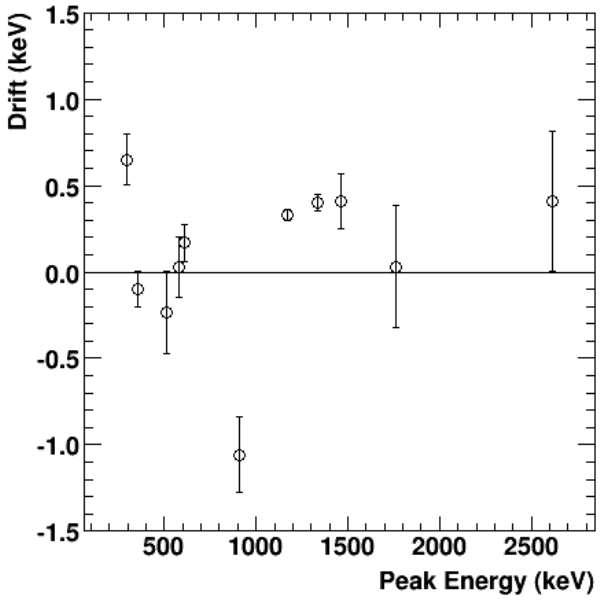

Figure 6.9: Drift between tapes 21 and 22 of the energy response of the β core channel. The error bars are reflective of the quality of the Gaussian fits used to estimate the peak centroid and are therefore dependent on the number of counts in the photopeaks and the background in the peak region.

One implication of this instability is that it was not possible to sum the two calibration tapes channel by channel in order to increase the statistics and hence the accuracy of the calibration. The Full Width at Half Maximum (FWHM) of the ^{60}Co peaks were measured for both tapes and the spectra with the lowest energy resolution were used for calibration purposes. A linear fit was implemented for each of the 111 AGATA electronics channels, where the calibrated energy, E is calculated according to

$$E = a + bx \tag{6.1}$$

where x is the spectral channel number and a and b are the determined calibration coefficients.

An attempt was made to correct the calibration for the drift of the electronics throughout the experimental run. As the spectral peaks resulting from the nuclear reaction were subject to large Doppler effects, they were unsuitable to extract meaningful information on the drift. No environmental peaks were visible in the in-beam spectra. However the 5ll keV γ-rays resulting from positron annihilation within the detectors were visible in all spectra and are not subject to the same Doppler effects as the those from the reaction. The 511 keV peak was therefore used to determine the extent to which each channel had drifted between tapes and this can be seen in Figure 6.10. Despite the significant change in the trend, in an attempt to keep statistics high, all of the tape numbers visible in this figure were used in the subsequent experimental analysis.

6.3 Reaction Specifics

The proposed experiment was to study the transfer reaction ^{47}Ti(d,p)^{48}Ti with inverse kinematics. To clarify, a ^{47}Ti beam was expected. However, upon inspection of the γ-rays produced in the reaction, it became apparent that they were attributed

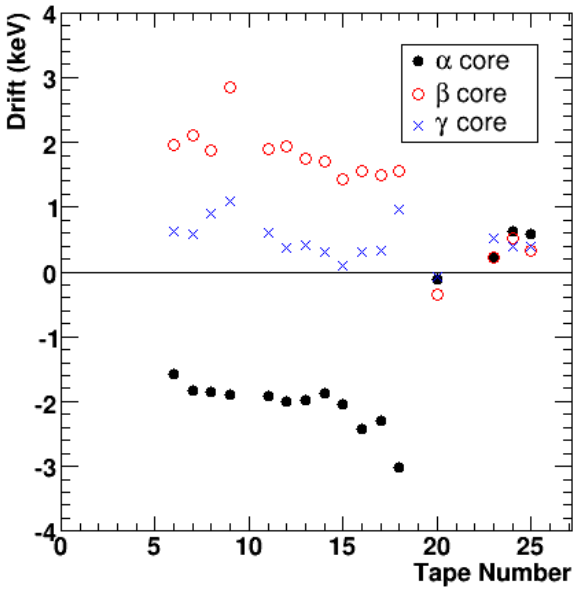

Figure 6.10: Drift of the 511 keV peak between the calibration tape used (tape 21) and each of the usable in-beam tapes for each of the three core channels. It is not clear why the trends change drastically after tape 20.

to ^{49}Ti. Furthermore, upon removal of the target, analysis of the gamma-ray energy spectra acquired indicated a strong presence of ^{48}Ti. It was concluded that the beam particles produced by the accelerator were ^{48}Ti and that ^{49}Ti was produced in the reaction. The ^{49}Ti level scheme, taken from Reference [Fe69], can be seen in Figure 6.11. Figure 6.12 shows the calibrated spectrum from the α (S001) core electrode for all of the usable in-beam tapes. It should be noted that no Doppler correction has been applied to this spectrum, so shifting of the γ-ray energies will be present, as well as broadening of the spectral peaks. The γ-rays from the excited ^{49}Ti nucleus are indicated, the most prominent of which results from the decay of the first excited $(3/2^-)$ state at 1382 keV to the ground state $(7/2^-)$ at 0 keV [Fi96]. Also visible in the spectrum is the resultant γ-ray from the decay of the 1723 keV state $(1/2^-)$ to the 1382 keV resulting in a 342 keV γ-ray. Also visible are γ-rays attributed to ^{48}Ti and these arise from excitation of the beam particles in the presence of the Coulomb field of the target nuclei. The 983 keV γ-ray is from the decay of the first excited (2^+) state to the ground state of ^{48}Ti (0^+).

6.3.1 Transfer Reaction

The differeential cross-section $(\mathrm{d}\sigma/\mathrm{d}\Omega)$ of the transfer reaction, ^{48}Ti(d,p)^{49}Ti, was calculated using a computer code based on a Distorted Wave Born Approximation, namely TWOFNR [TW77]. The results of the calculation can be seen in Figure 6.13 as a function of proton angle. The integration of this curve gives the total cross section of the transfer reaction and is approximately equal to 140mb. Figure 6.14 shows the reaction cross section according to the software in the approximate angular range of the DSSSD and integrates to 19 mb.

As a transfer reaction can be considered a single-step process, its kinematics can be reconstructed using energy and momentum conservation laws. Thus many of the parameters that are necessary to correct the Doppler shifted energy, according to Equation 2.40, can be calculated from the energy and angle of the proton detected in

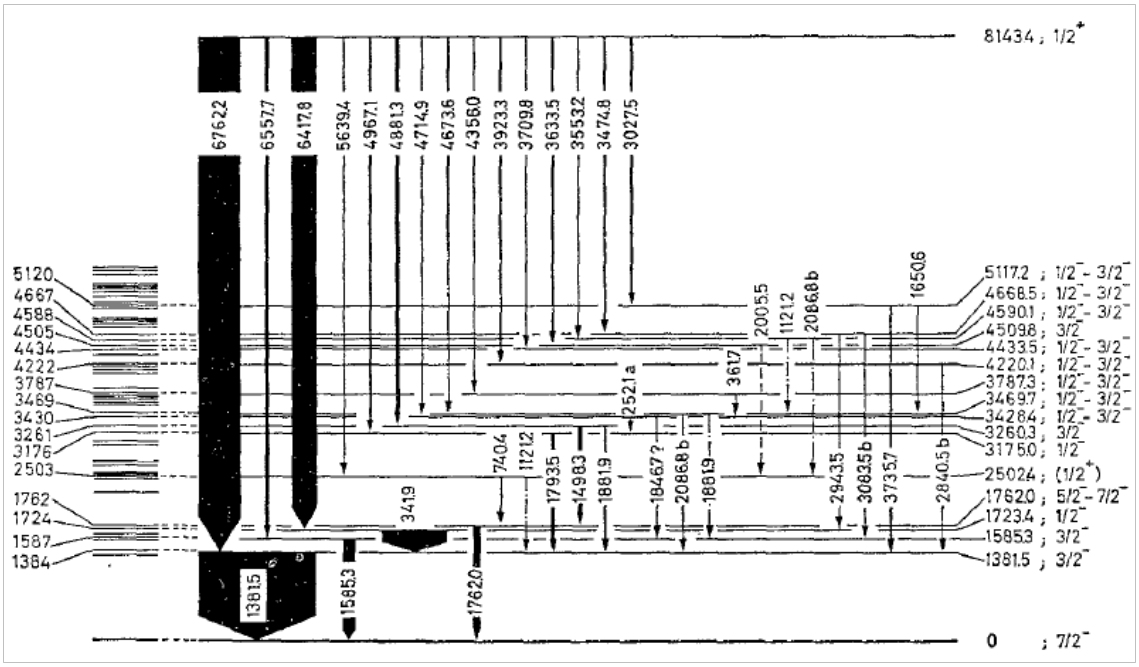

Figure 6.11: The ^{49}Ti level scheme, taken from Reference [Fe69]. It can be noted that this reference also contains the level scheme for ^{48}Ti.

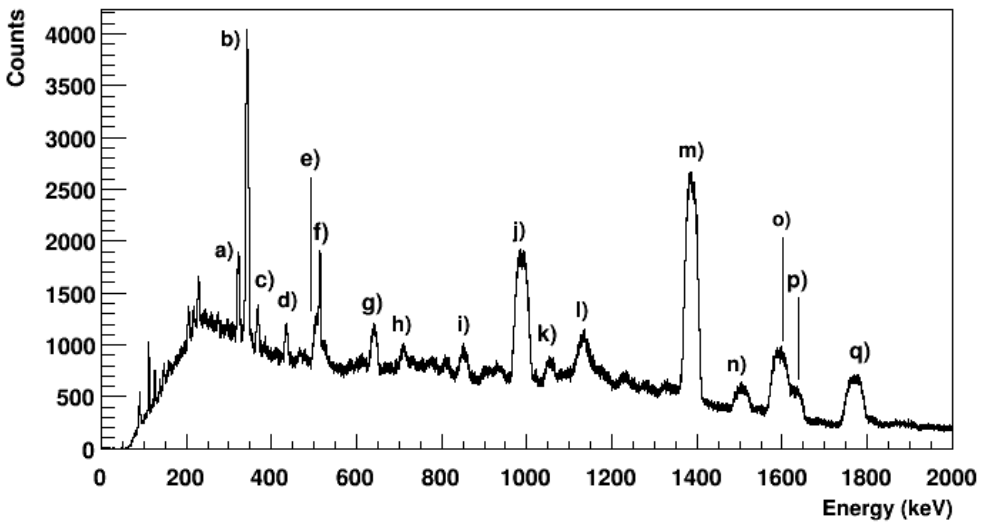

Figure 6.12: Raw γ-ray spectrum from the core channel of the α (S001) detector. Some of the more prominent peaks are discussed in the text and identified in Table 6.4.

Label	E_γ (keV)	Nucleus	Transition $E_{Level(in)} \rightarrow E_{Level(fi)}$ (keV)
a)	322	Unknown	
b)	342	^{49}Ti	1723→1382
c)	367	Unknown	
d)	434	^{49}Ti	4222→3788
e)	499	^{49}Ti	2261→1762
f)	511	Annihilation	
g)	638	^{49}Ti	2261→1623
h)	709	^{49}Ti	2471→1762
i)	848	^{49}Ti	2471→1623
j)	984	^{48}Ti	984→0
k)	1055	Unknown	
l)	1139	^{49}Ti	2517→1382
m)	1382	^{49}Ti	1382→0
n)	1499	^{49}Ti	3261→1762
p)	1586	^{49}Ti	1586→0
q)	1623	^{49}Ti	1623→0

Table 6.4: Energy and associated information of the prominent peaks in Figure 6.12.

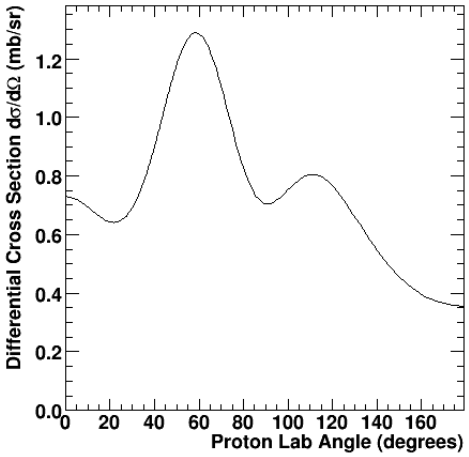

Figure 6.13: Transfer reaction cross section as a function of proton angle in the laboratory coordinate system.

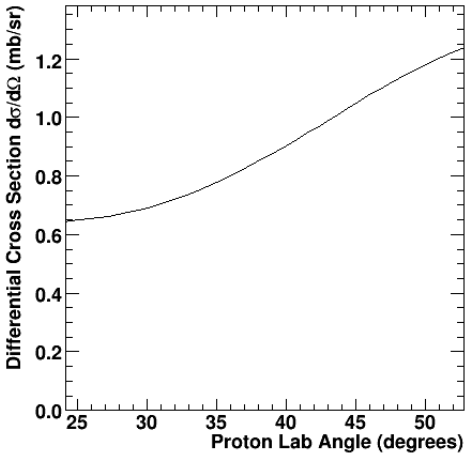

Figure 6.14: Transfer reaction cross section as a function of proton angle in the laboratory coordinate system. The angular range matches that of the DSSSD.

the DSSSD. The Q value of the reaction is defined as follows

$$Q = (M_1 + M_2) - (M_3 + M_4) \tag{6.2}$$

Here M denotes the mass energy of the nuclei and the subscripts indicate the particle as detailed in Table 6.5. Nuclear masses are calculated from atomic masses [Au03] corrected for the electron mass and binding energy [Lu03] to give a Q-value for the transfer reaction of 5.92 MeV.

Subscript	Particle
1	Beam nucleus
2	Target nucleus
3	Beam-like recoiling nucleus
4	Target-like projectile nucleus

Table 6.5: Subscript notation of the nuclei involved in the kinematic reconstruction.

Conservation of energy states that the total initial energy before the reaction must equal the final total energy, as follows

$$\sum W_{in} = \sum W_{fi} \tag{6.3}$$

In the case of each particle involved,

$$W_i = M_i + T_i + E_i \tag{6.4}$$

where T represents the kinetic energy of the particle and E is its excitation energy, where appropriate, and i=1,2,3 or 4 as described in Table 6.5. Equation 6.3 then becomes,

$$M_1 + T_1 + M_2 = M_3 + T_3 + E_3 + M_4 + T_4 + E_4 \tag{6.5}$$

For the transfer reaction, the proton excitation energy, E_4, is zero and that of the ^{49}Ti nucleus, E_3, is dependent on the state being investigated. This is determined from the γ-ray energy and a knowledge of the level scheme [Ma81]. For example, in the case of the 1382 keV peak, it is likely that this is the excitation energy, however the 342 keV peak comes from the 1723 keV state.

Equations 6.2 and 6.5 can be combined and substituted into Equation 6.6, derived from the law of momentum conservation,

$$P_3^2 = P_1^2 + P_4^2 - 2P_1P_4\cos\theta_4 \tag{6.6}$$

where P_i is the momentum of each particle and θ_i is its angle from the beam axis. A relativistic approach was adopted in which

$$P_i = \sqrt{2M_iT_i + T_i^2} \tag{6.7}$$

The preceding equations reduce to a solvable quadratic equation for the projectile kinetic energy as a function of its angle from the beam axis. This in turn enables the kinetic energy of the recoiling nucleus to be calculated by reapplication of conservation

laws, along with its velocity by rearrangement of Equation 6.8. The results of these calculations can be seen in Figures 6.15, and 6.16.

$$T = M\left(\frac{1}{\sqrt{1-\beta^2}} - 1\right) \tag{6.8}$$

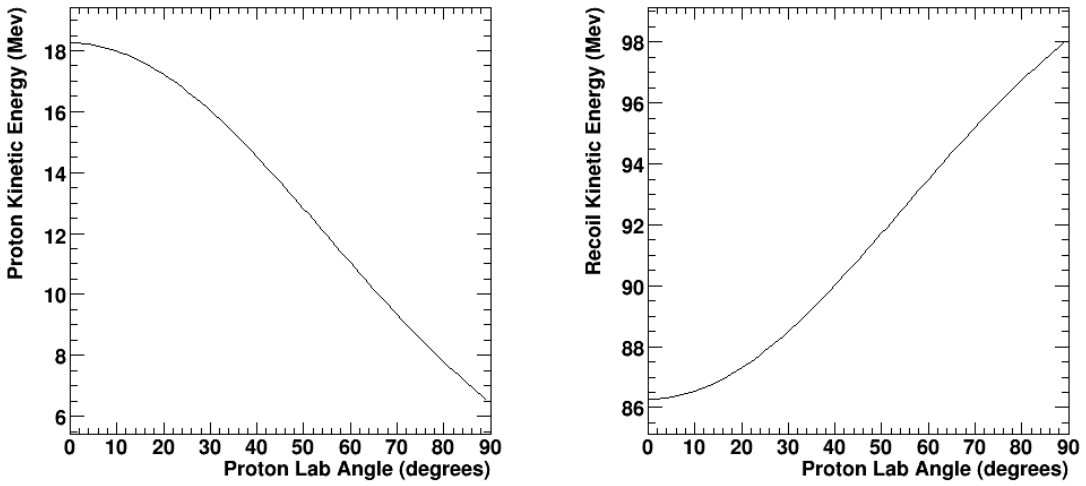

Figure 6.15: Kinetic energy of the residual particles from the transfer reaction as a function of proton angle in the laboratory coordinate system. Namely that of (*left*) the proton and (*right*) the recoiling ^{49}Ti nucleus.

6.3.2 Fusion-Evaporation Reaction

The Coulomb barrier for fusion of the incident ^{48}Ti beam particle and the ^{2}H target nucleus, arising due to the electrostatic repulsion of the charged nuclei, is given by software [qv96] as 94.4 MeV. At a beam energy of 100 MeV it is possible for the nuclei to fuse and form ^{50}V with a total cross section of 157 mb, given by a PACE calculation in quantum mechanical mode [LI02]. The Q value of the reaction is given by the software as 13.9 MeV. However the ^{50}V can subsequently decay via proton or neutron emission to create ^{49}Ti or ^{49}V respectively. The neutrons will not be detected

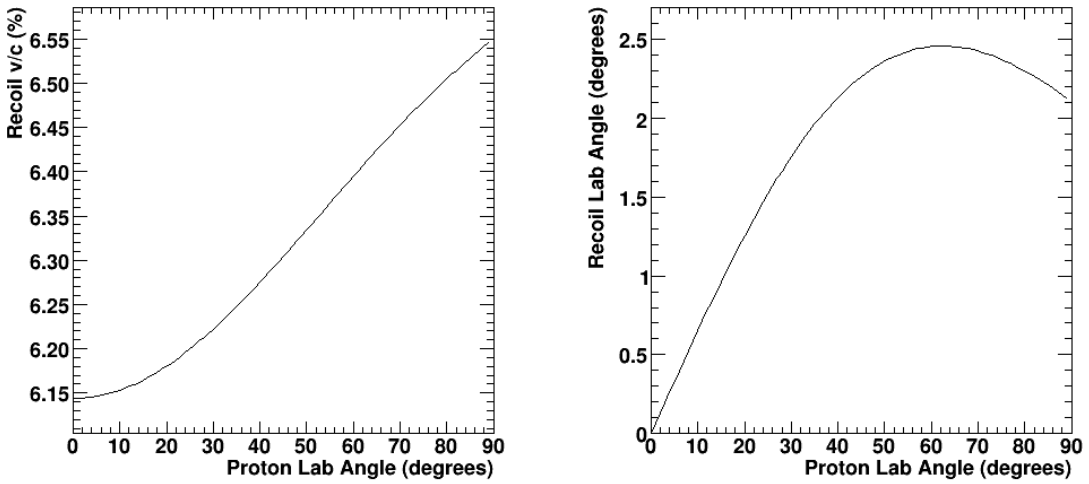

Figure 6.16: Velocity (*left*) and laboratory angle (*right*) of the recoiling ^{49}Ti nucleus from the transfer reaction as a function of proton angle in the laboratory coordinate system.

in the DSSSD and will therefore not trigger the data acquisition. The cross section of the p-channel is given by the PACE calculation as 26.3 mb. As the fusion-evaporation mechanism is a two step process and probabilistic in nature, it is not possible to calculate the expected angles and energies of the residual nuclei as for a direct reaction. Furthermore, there is little information on how the cross section varies as a function of emission angle, although it is acceptable to assume that fusion evaporation residual nuclei are generally strongly forward focused. PACE uses a Monte Carlo approach to estimate the reaction frequencies. The angular distribution of the protons given by the calculation in the laboratory reference frame is presented in Figure 6.17. Also shown in the figure is a polynomial fit of the distribution and representative maximum and minimum curves.

6.3.3 Coulomb Excitation and Inelastic Scattering

Inelastic scattering of the beam particles by the target is also likely to occur. The nuclei interact electromagnetically and can be left in an excited state. The beam particles can scatter off the contaminants expected to be present on the target, namely

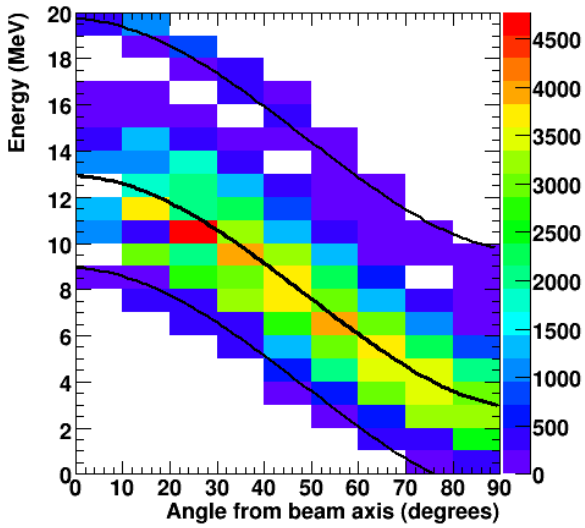

Figure 6.17: Proton energy as a function of its emission angle from the fusion evaporation reaction, ^{48}Ti(d,p)^{49}Ti. The data is taken from a PACE calculation.

^{12}C and ^{16}O. The same kinematic reconstruction as for the transfer reaction can be applied to this direct reaction. In this case the Q value of the reaction is zero as the nuclear masses remain unchanged following the reaction. The excitation energy of the ^{49}Ti nucleus is obtained in the same manner as for the ^{49}Ti in the transfer reaction. However in the case of the Coulex resulting from the contaminants, where there are more than 2 nucleons in the projectile (target-like) particles, they can also have an excitation energy. It is most probable that the first excited states in these nuclei are occupied and these are at energies of 4439 keV for the ^{12}C nucleus (2^+) and 6917 keV for ^{16}O (2^+). The results of these calculations can be seen in Figures 6.18 and 6.19 for the two possible Coulomb excitation reactions.

6.4 Separation of Reaction Channels

As both the fusion evaporation and transfer reactions result in an excited ^{49}Ti nucleus, it is not possible to differentiate between the two types of reaction from the γ-ray

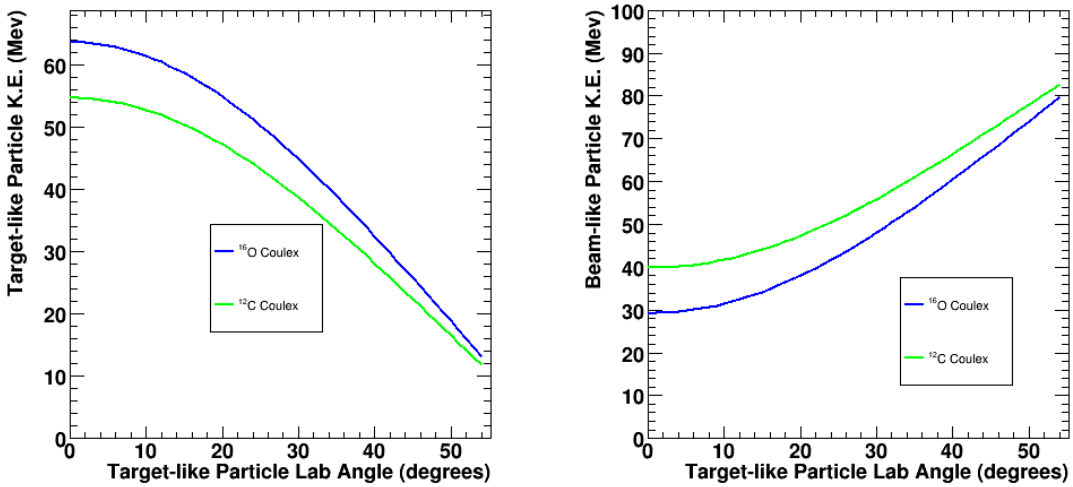

Figure 6.18: Kinetic energy of the residual particles from the various Coulomb excitation reactions as a function of the target-like particle angle in the laboratory coordinate system. Namely that of (*left*) the target-like (light) nucleus and (*right*) the beam-like (heavy) nucleus.

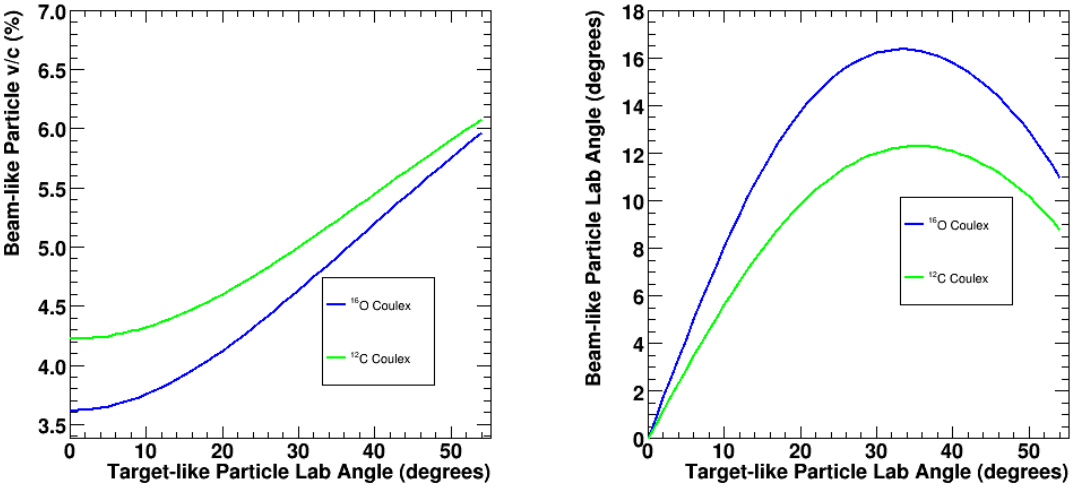

Figure 6.19: Velocity (*left*) and laboratory angle (*right*) of the recoiling ^{48}Ti nuclei from Coulomb excitation as a function of the target-like particle angle in the laboratory coordinate system.

energy detected. It was previously established that the fusion evaporation mechanism is a two step process and therefore the properties of the residual nuclei cannot be reconstructed from the knowledge of the beam and target properties. It is not possible in this case to perform an event-by-event Doppler correction, and it is necessary to remove γ-rays associated with this type of event from the spectra obtained. In order to do this, one can select the γ-rays correlated with particles detected in the DSSSD which follow the expected pattern of angle and energy according to Figure 6.15 (a). The Silicon ring in which a particle is detected is closely attributed to its angle with respect to the beam axis. Figure 6.20 displays the particle energy as a function of the DSSSD ring in which it is detected.

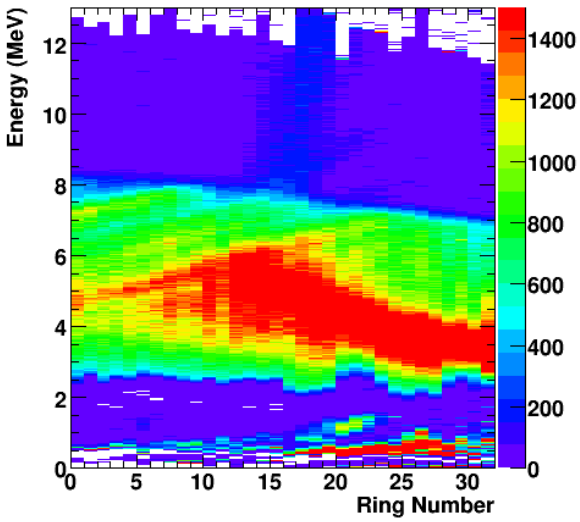

Figure 6.20: Energy deposited as a function of ring number in the particle detector. The reader is reminded that the angle from the beam axis is in the reverse direction to the ring numbering.

Unfortunately, in the case of the transfer and fusion evaporation reaction channels the projectile kinetic energy was too large to be fully deposited in the silicon detector, even upon consideration of the energy lost in the aluminium absorber. The average

energy lost per unit path length of the proton in the DSSSD, the absorber and the remaining target material[4] is calculated using reference [NI08a]. It should be noted that the nuclear and electronic stopping power of the target and absorber material are used in the following calculations as this constitutes the total energy lost by the particle. However, in the detector, only the electronic stopping is considered, as the energy lost due to atomic motion (nuclear stopping) is not available to create electron-hole pairs and will therefore not be detected. The stopping powers as a function of particle energy are displayed graphically in Appendix D. The results of these calculations can be seen in Figure 6.21 as a function of angle from the beam axis. It should be noted that the thickness of the target, absorber and detector at an angle of 0° from the beam axis, $T_\circ$, is 0.488 μm, 16 μm and 300 μm respectively. However at an angle, θ, from the beam axis, the effective thickness of each material, T, is

$$T = \frac{T_\circ}{\cos\theta} \tag{6.9}$$

The average detectable energy deposited in the silicon is the difference between the blue and red curves and is plotted in the left plot of Figure 6.24 for the approximate angular range of the DSSSD. In order to understand the pattern in the DSSSD more precisely, the energy deposited by the Coulomb excitation projectiles (namely, ^{12}C and ^{16}O) can also be calculated. In this case, the energy lost per unit path length was calculated using local software (Gostop) [Go97] according to [Br77]. Again, these stopping powers are displayed in Appendix D. As for the deuterium, the contaminants are considered to be on the outer surface of the target material. The results of these calculations can be seen in Figure 6.23. The energy deposited in the silicon detector for the Coulomb excitation reactions is also plotted in the left plot of Figure 6.24. Also visible in this plot are the limits to the proton energy range from the fusion evaporation

[4]It is assumed here that the deuterium is located on the surface of the Titanium target and the nuclear reaction occurs on the beam-side of the target material. The projectile must then traverse the thickness of the target material.

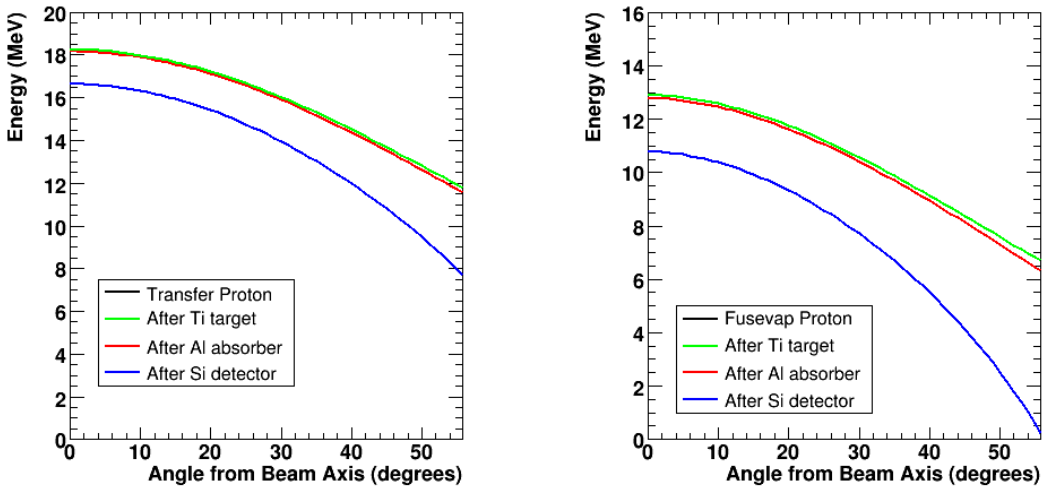

Figure 6.21: Proton energy from the reaction mechanism as a function of its angle from the beam axis (black). Remaining energy after the proton has passed through the target (green), Aluminium absorber (red) and Silicon detector (blue). The black line is barely visible behind the green line; there is little change in the proton energy upon passing through the target material. The proton energy from the transfer reaction (*left*) is as detailed in Section 6.3.1 and that of the fusion evaporation reaction (*right*) is discussed in Section 6.3.2.

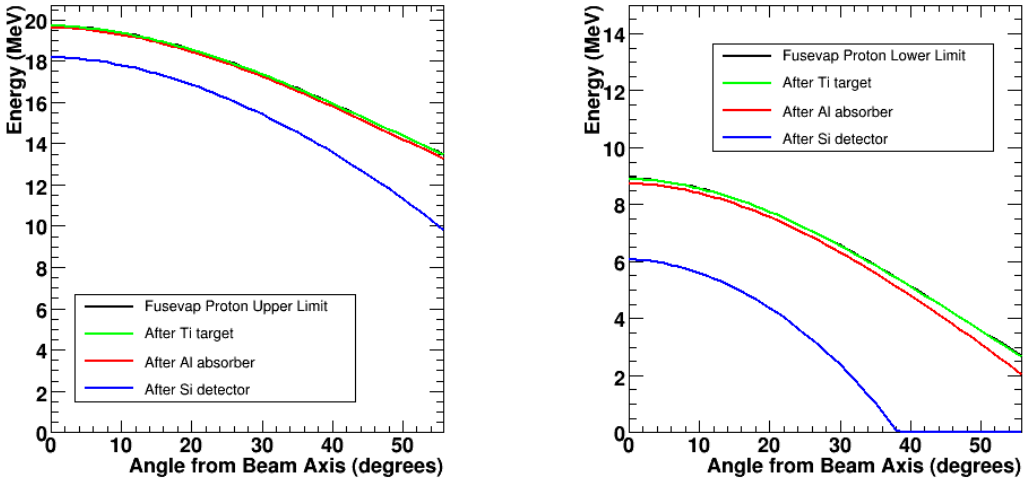

Figure 6.22: Proton energy from the reaction mechanism as a function of its angle from the beam axis (black). Remaining energy after the proton has passed through the target (green), Aluminium absorber (red) and Silicon detector (blue). The black line is barely visible behind the green line; there is little change in the proton energy upon passing through the target material. The protons' initial energy is taken as the upper limit (*left*) and the lower limit (*right*) of the fusion evaporation reaction as displayed in Figure 6.17.

reaction as shown in Figure 6.17 and the proton energy from the transfer reaction to the 1723 keV state of ^{49}Ti. These curves are overlaid onto the real data from the DSSSD in the right plot of Figure 6.24. It can be noted that, in this figure, the likely fusion evaporation energy deposition in the Si detector appears to be outside of the maximum and minimum curves. This is explained by consideration of Figure 6.22 and the right-hand plot of Figure 6.21. It can be seen that the upper limit to the proton energy from the fusion evaporation reaction deposits less energy than the likely proton energy from this reaction as it passes through the Si detector.

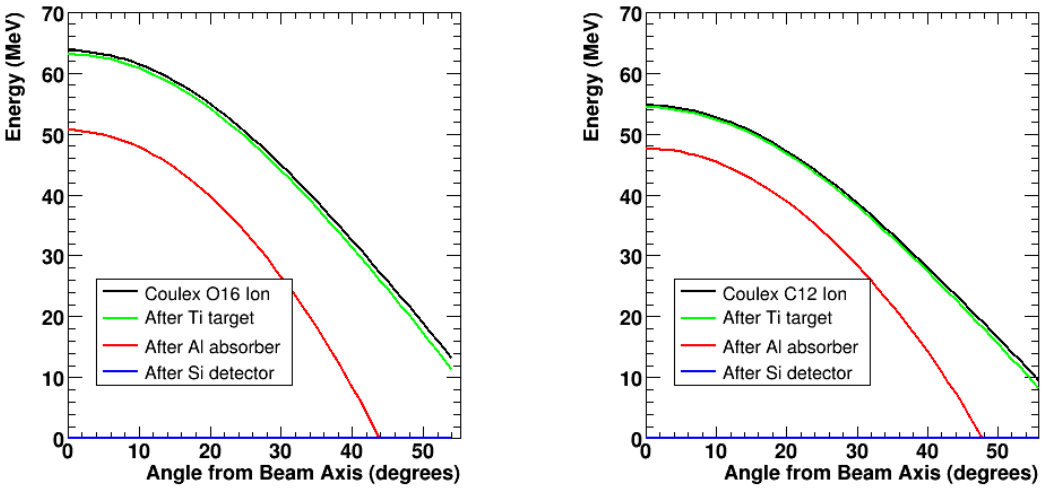

Figure 6.23: As for Figure 6.21 but using the kinematic reconstruction of the inelastic scattering of the beam particles on the contaminants ^{16}O (a) (*left*) and ^{12}C (b) (*right*) to calculate the kinetic energy of the respective nucleus as a function of its angle from the beam axis.

Evident from Figure 6.24 is that the calculated angular and energy range of the transfer reaction does not match the region of the DSSSD which contains particles from the strongest reaction. In order to understand the DSSSD patterns more clearly, the peaks in the gamma-ray energy spectra can be selected and the corresponding DSSSD data can be projected. The results of this investigation can be seen in Fig-

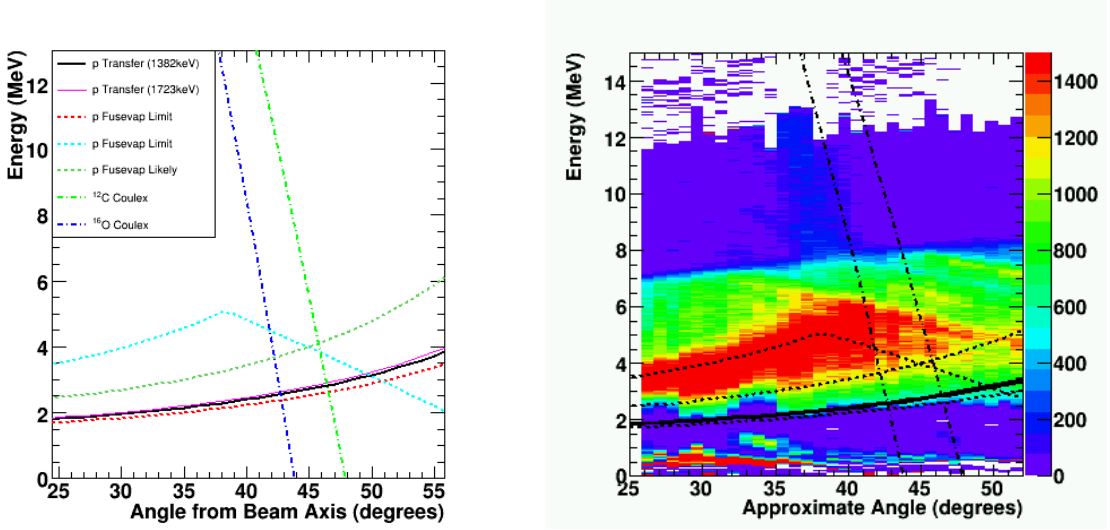

Figure 6.24: (a): (*left*) Average energy deposited in the Silicon detector for nucleon transfer to the 1382 keV and 1723 keV states of ^{49}Ti, and from the various Coulomb excitation reactions. Also shown is the average energy deposited by the fusion evaporation reaction, fitted from a PACE calculation (discussed in Section 6.3.2) as well as the energy deposited from the approximate limits of the proton energy from the reaction. The energy lost in the target and absorber is accounted for as well as the fact that the particles punch-through the silicon detector. (b): (*right*) Energy deposited in the silicon detector. The ring number was converted to an approximate angle taking no consideration of the offset of the detector from the beam axis. The curves displayed in the left plot of Figure 6.24 are overlaid on the plot in order to ease comparison.

ure 6.25. In the right-hand plot of Figure 6.25, the calculated energies as a function of angle for the Coulomb excitation particles shows good correlation with that which is detected, giving confidence in the calculation methods. Furthermore, the calculated location of the fusion evaporation proton, Figure 6.25 (a), is in reasonable agreement with the data from the silicon detector. However, there is little experimental evidence to support the location of the calculated transfer reaction proton, and, the DSSSD range where the 1382 keV peak is most intense has no expected reaction associated with it.

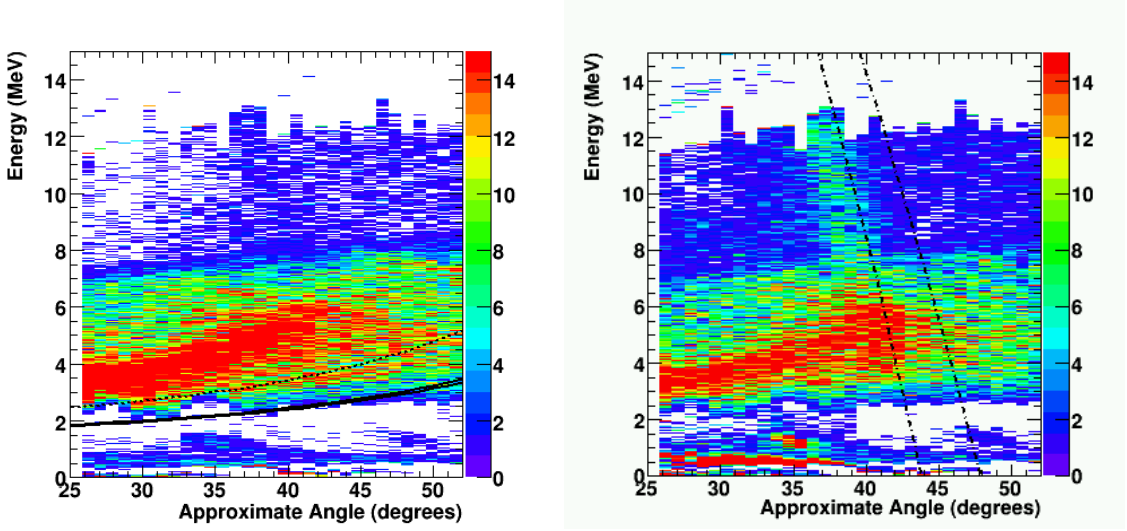

Figure 6.25: Energy detected in the DSSSD versus its approximate angle from the beam axis when placing a gate on the γ-ray energy deposited in the AGATA detectors. The first energy gate was placed around the 1382 keV peak from ^{49}Ti (a) (*left*) and the expected locations of the transfer and fusion evaporation reaction protons are overlaid in order to ease comparison. The second energy gate was placed around the 984 keV γ-ray from ^{48}Ti (b) (*right*) and the expected locations of the Coulomb excitation particles are again overlaid.

There are a number of possible explanations for the lack of particles detected in the expected range of the DSSSD for the transfer reaction:

1. The calibration of the Silicon detector is not correct. In order to correlate the

expected transfer proton range with the most intense region of the DSSSD, the calibration would need to be offset by approximately -1.5 MeV. However, this would imply that the calculated location of the Coulomb excitation particles was incorrect. Given the good correlation of the Coulomb excitation particles, it is assumed that the calibration is correct.

2. The construction of the target is assumed in this work to be largely natural titanium material which has deuterium and contaminants on its outer surface. The nuclear reactions are therefore assumed to occur beam-side of the target and the residual particles must then traverse the thickness of the material. If the target is not constructed in this way, and indeed the nuclear reactions do not occur on its outer surface, the straggling of the beam particle energy within the material should be considered. The energy lost by the 100 MeV ^{48}Ti beam particles can be estimated from the total stopping power in titanium material, as for the residual nuclei. The stopping power as a function of energy can be seen in Appendix D. Assuming that the reaction occurs in the centre of the target material, the straggling is expected to reduce the beam energy by an average of 1.8 MeV. Applying this difference in beam energy to the curves seen in Figure 6.24 makes no visible difference to their location. It can be concluded that straggling of the beam particle energy is not responsible for the discrepancy in the transfer proton location.

3. It must be considered that there may be some incorrect or omitted information concerning the target, absorber or some other aspect of the experimental setup that gives rise to the discrepancy.

4. The transfer reaction to the 1382 keV ^{49}Ti state is weak in comparison to the other reaction mechanisms. It is usual to normalise the cross section given by a TWOFNR calculation to the observed reaction frequency and it is therefore difficult to compare the cross sections of the various reaction mechanisms in the absence of a reliable absolute value. Consideration of the shape of the reaction

cross section which increases with angle, displayed in Figure 6.14, suggests that the expected location of the protons is correct but that the cross section may not be large enough until the larger angles. The most populated region of the DSSSD would therefore require some other reaction in explanation of its presence. A likely candidate for this is a transfer reaction to a higher energy state of ^{49}Ti and then subsequent decay to the 1382 keV state. Rough calculations predict that a state in ^{49}Ti at $\sim$7 MeV would cause the observed pattern in the DSSSD.

In order to further understand the reaction mechanisms, graphical cuts can be created around the various regions of Figure 6.24 and the associated γ-rays can be investigated. Some of the applied graphical cuts can be seen in Figure 6.26 and are labelled *a*, *b*, *c* and *d*. The γ-rays associated with these graphical cuts can be seen in Figure 6.27.

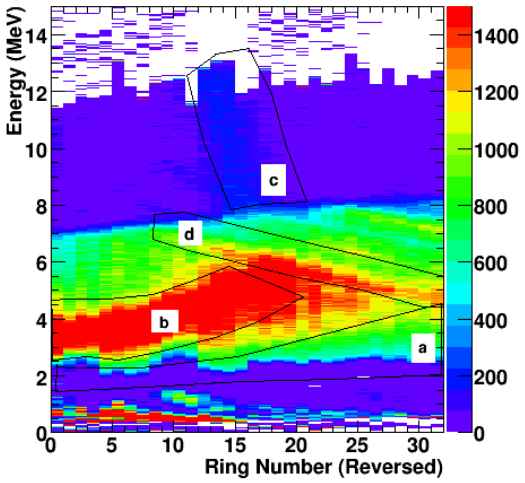

Figure 6.26: Energy deposited in the particle detector as a function of its ring - in this plot the ring number displayed is 32-R where R is the actual ring number. The graphical cuts around various regions of the data are also displayed in the figure and are labelled *a*, *b*, *c* and *d*.

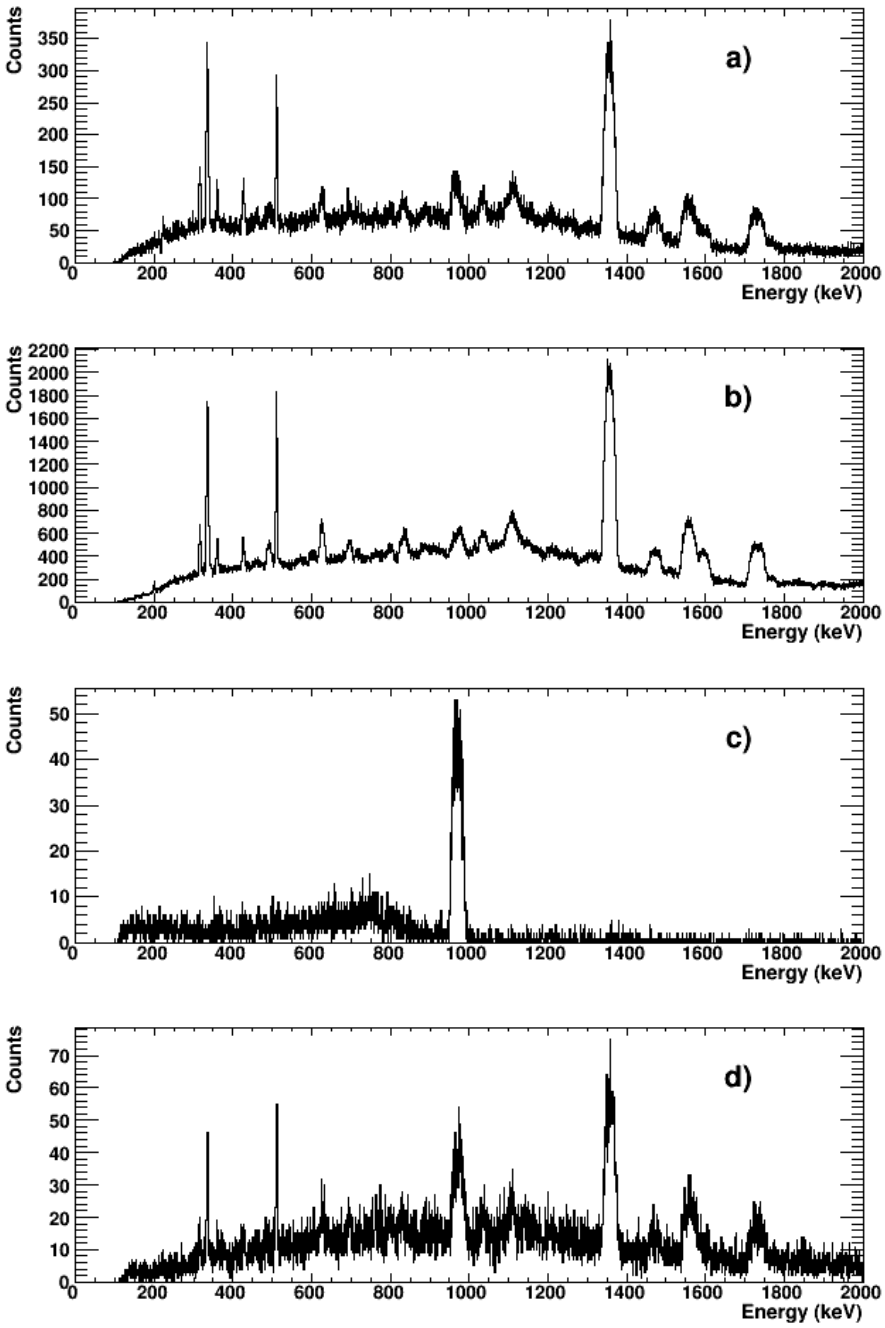

Figure 6.27: Gamma spectra resulting from the graphical cuts placed on the data in the particle detector. The graphical cuts, labelled *a*, *b*, *c* and *d*, can be seen in Figure 6.26.

It can be seen from Figure 6.27 that the region of expected transfer reaction protons, region *a*, contains largely γ-rays attributed to ^{49}Ti (these are listed in Table 6.4). The 984 keV peak attributed to ^{48}Ti is also present in this spectrum with far less intensity than the peaks of ^{49}Ti. However, it can only be concluded that in this projectile energy and angular region, ^{49}Ti is produced from the reaction ^{48}Ti(d,p)^{49}Ti via the fusion evaporation *or* one nucleon transfer mechanism.

Gating on region *b* of Figure 6.26 produces a similar γ-ray pattern to region *a*, albeit with far greater statistics. The same conclusion can be drawn as for region *a*. However, gating on region *c* of the Silicon detector produces only the γ-ray peak attributed to ^{48}Ti. This region was predicted to be the location of the Coulomb excitation projectiles and the resultant spectrum is consistent with the reaction. Region *d* shows the presence of both ^{48}Ti and ^{49}Ti γ-rays.

6.5 Doppler Correction

The energy deposited in the AGATA detectors was corrected according to Equation 2.40 event-by-event. In this equation the value of β was calculated according to the kinematics dictated by the location of the particle detected in the DSSSD. This can be seen for the transfer reaction in Figure 6.16 (a) and for the various Coulomb excitation reactions in Figure 6.19 (a). The angle of the recoiling nucleus from the beam axis was also calculated in this way and the projection of this angle in the *zy* plane was found. This was added to the projection of the angle between the photon and the beam axis in the same plane to give the total angle between the recoil and the photon, θ_γ.

The Doppler correction was applied to fold 1 events only, as convoluted pulses would not produce comparable parameterisations. Figure 6.28 shows the frequencies of the various segment folds for this data set. There are no events with a segment

fold greater than 36 due to the fact that the events were separated in the presorting process according to the crystal which fired. Out of ∼22 million events, only 17 % are fold one.

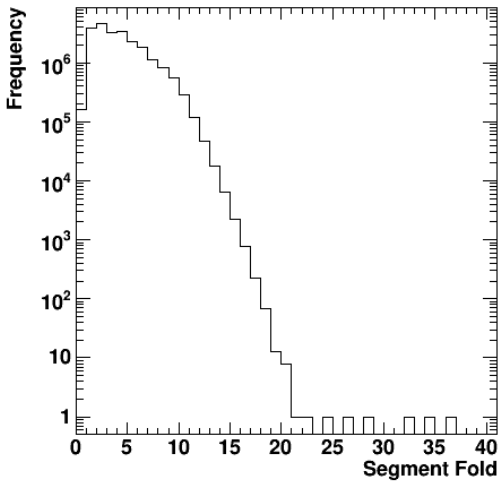

Figure 6.28: Frequencies of segment folds for the entire experimental data set.

For the first instance, θ_γ, was calculated to the level of precision of each detector, such that the γ-interaction was presumed to be at the centre of the detector. Secondly, information from the segment which fired was used to improve the precision of θ_γ to segment level, such that the centre of the hit segment was taken as the location of the γ-interaction. Finally, the r and θ coordinates of the γ-interaction within each segment were calculated according to the method discussed in Section 5.6 and the depth dimension was taken as the mid-point of the physical segmentation boundaries. Figure 6.29 displays the resulting spectra from this analysis of the 1382 keV peak using events from the graphical cut labelled a in Figure 6.26. Application of the graphical cut as well as the requirement for fold 1 events has created poor statistics in this figure. In each of the following figures, where a FWHM is displayed, it is obtained from Gaussian fitting of the spectral peaks at each stage of the Doppler correction and is quoted in keV. Consistently the peaks obtained from the S003 (γ) detector had

the lowest FWHM, at all levels of the Doppler correction and it is a selection of these peaks that are shown in the following figures.

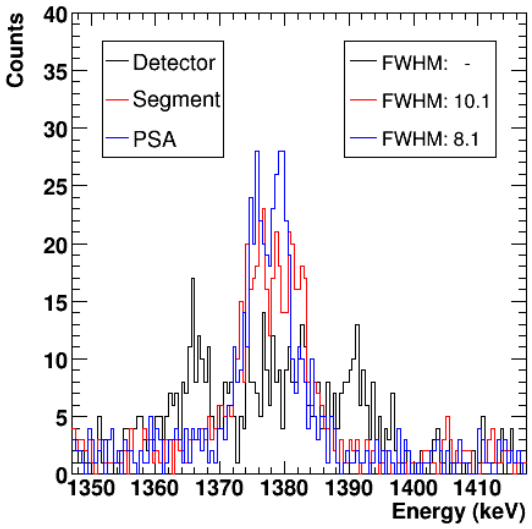

Figure 6.29: The 1382 keV peak as seen by the central contact of the S003 detector. Only events which fall into the graphical cut labelled *a* in Figure 6.26 are included in the spectrum. The text provides more information on the Doppler correction applied as well as the 3 levels of spatial precision used, indicated in the figure by the 3 coloured spectra. The value of v/c was calculated event-by-event using the kinematics of the transfer reaction as this region of the Si detector is where the transfer protons are expected according to Figure 6.24. It can be noted that no suitable fit could be obtained for the detector level spatial resolution, shown in black.

The reader may be aware of an inaccuracy in the peak energy visible in Figure 6.29, by which the peak energy is at ∼1378 keV as opposed to 1382 keV. There are a number of possible explanations for this unexpected discrepancy. One possibility is the presence of an error in the energy calibration. The thorough approach to the energy calibration, as detailed in Section 6.2, in addition to the close energy value of the peaks used for calibration (1173 keV and 1332 keV) to that currently under

investigation, a calibration error is not believed to be responsible for this discrepancy. Further evidence for the likelihood that the aforementioned discrepancy is not caused by a calibration error can be found in the fact that the 511 keV peak energy is unshifted.

Another possible explanation for the discrepancy is an error in the calculated position of the detectors with respect to the beam line, which would lead to an energy dependent mis-calculation of the true value of E_γ. Determination of the position of the AGATA detectors in the laboratory co-ordinate system is discussed in Section 6.1.1 and is not within the scope of this work. The plausibility of this explanation is investigated further by consideration of the difference in the peak energies between the three different detectors, as can be seen in Figure 6.30. Evidently the spectra which are not Doppler corrected (left plot of the Figure) show no visible sign of the difference in energy, only the expected Doppler shift. The right plot of this figure shows the same energy spectra Doppler corrected with PSA level spatial information. The S001 detector has the most accurate peak energy; this is the detector which is closest to an angle of 90° to the recoil direction (see Table 6.1). The energies form S002 and S003 are both shifted lower in energy, indicating that the whole triple cluster is mis-aligned. Rearrangement of Equation 2.40 allows the photons' emission angle for a 4 keV shift in energy to be estimated. An angle of 92.6° is obtained form this calculation. Figures 6.31 to 6.32 show the same effect for various combinations of peak energies and graphical cuts.

Figure 6.31 shows the Doppler corrected spectra, again for the S003 detector at the three levels of spatial precision, but only using events which fall into the graphical cut labelled *b* in Figure 6.26 (that is the region of highest intensity in the DSSSD). This selection of events shows a greater reduction in the FWHM than that pertaining to the region of the expected transfer reaction protons (7.3 keV as opposed to 8.1 keV). However the far greater statistics in the former could be responsible for the improved

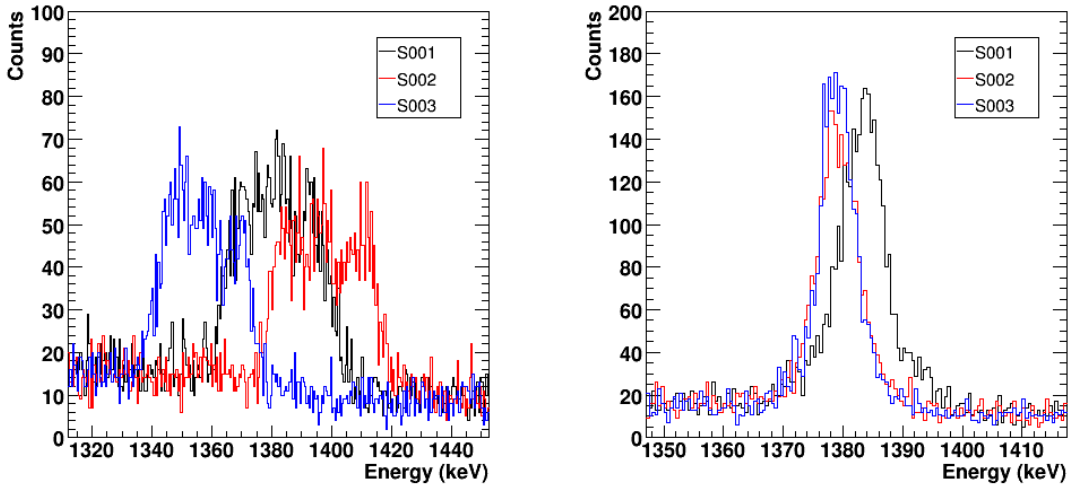

Figure 6.30: 1382keV peaks from all three detectors with no Doppler correction applied (*left*) and with application of PSA level Doppler correction (*right*). The value of v/c was calculated event-by-event using the kinematics of the transfer reaction.

peaks and no conclusion as to the nature of the originating reaction is drawn from this evidence. Figure 6.32 shows the 342 keV ^{49}Ti peak. A PSA level FWHM of 3.2 keV can be observed.

The best energy resolution achieved for the 1382 keV peak using this method can be compared to Figure 3.8 which relates the spatial resolution achieved to the energy resolution obtained following the Doppler correction. It can be seen in the Figure that an energy resolution of 7.3 keV implies a position resolution of ∼9 mm. The reader may recall from Section 5.6.3 that a position resolution of 9.3 mm was achieved for the S003 detector, in excellent agreement with the prediction. However, Section 5.6.3 also derives a spatial resolution of 5 mm for the S002 detector, and a significantly better energy resolution could therefore be expected. Evident from Section 6.2 is that the electronics for the S003 detector were far more stable than those of S002 and S001, and this instability is believed to be responsible for the poorer energy resolutions obtained.

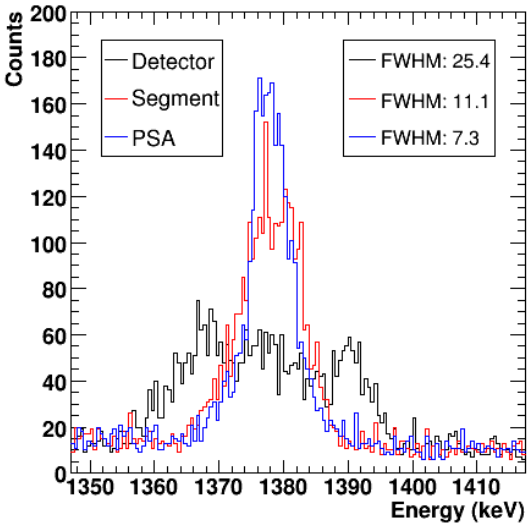

Figure 6.31: The 1382 keV peak of the S003 detector's core channel. Only events which fall into the graphical cut labelled *b* in Figure 6.26 are included in the spectra. The text provides more information on the Doppler correction applied as well as the 3 levels of spatial precision used, indicated in the figure by the 3 coloured spectra. The value of v/c was calculated event-by-event using the kinematics of the transfer reaction. The statistics are far greater in these spectra than those in Figure 6.29 as the region of the Si detector associated with this graphical cut contained more events.

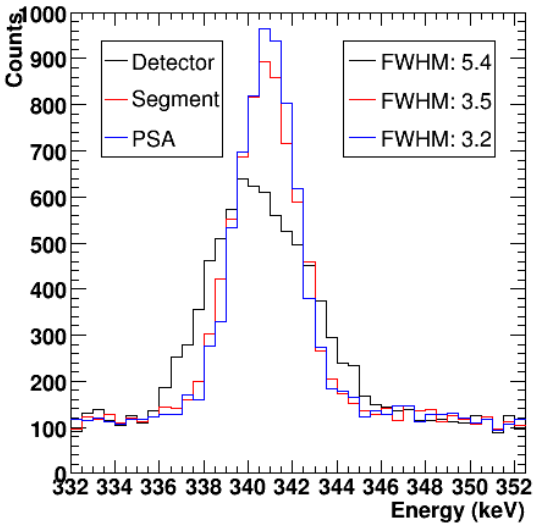

Figure 6.32: The 342 keV peak of the S003 detector's core channel. Only events which fall into the graphical cut labelled *b* in Figure 6.26 are included in the spectrum. The text provides more information on the Doppler correction applied as well as the 3 levels of spatial precision used, indicated in the figure by the 3 coloured spectra. The value of v/c was calculated event-by-event using the kinematics of the transfer reaction.

Chapter 7

Summary, Conclusions and Recommendations

7.1 AGATA Prototype Detectors

Prototype AGATA detectors have been scanned and characterised both in this work, to aid analysis of the experimental data, and in more general terms in Reference [Di07]. Some of the prominent findings in this work are highlighted below.

1. From Section 4.1.3, it is evident that there is a lack of understanding of the depletion of the crystals as the available theoretical predictions imply that the detectors are not fully depleted within the specified operating conditions. The impurity concentration values given in the S003 datasheets, included in Appendix C, support the linearity of this value with respect to the length of Ge. This is evident in Figure 4.2. This work does not rule out the hypothesis that there may be a radial variation in impurity concentration which is responsible for the apparent depletion of the crystals throughout their detecting volumes despite the theoretical calculations. It is recommended, and already widely accepted, that the detector response as a function of position should be investigated for various operating voltages to aid understanding of the depletion of

charge carriers. It is also identified that a value of the uncertainty on the crystal impurity concentrations would be advantageous and could be supplied by the manufacturers.

2. In the conditions described in Section 4.3.1, superior energy resolution is achieved by the S002 detector, compared to the S003 detector, by an average of $\sim$0.1 keV. However, analysis in the time domain, in Section 4.3.3, suggests that there is more low frequency noise associated with the S002 segment preamplifiers than with those of S003. With a frequency of $<$1 MHz, the period of this noise would be $\sim$1 μs. This is reflected by the noise analysis of the two detectors in Figure 4.11.

3. Section 5.2.1 highlights the different segment labelling of the two detectors with respect to their principal crystallographic axes. It is suggested that future characterisation, and indeed the acquisition and analysis of experimental data, would be made simpler if some consistency in segment labelling were achieved in subsequent AGATA detectors. This view is heightened by the expected ease with which this could be achieved.

4. This work has shown that the locations of the crystallographic axes not only influence the magnitude of charge carriers drift velocities but also have a significant affect on their trajectory (Section 5.2.2). Charge carriers are seemingly preferentially drawn to the $\langle 110 \rangle$ axes, creating larger effective detecting volumes where these axes are present. This is evident upon comparison of the intensity of interactions seen by segments within in each ring in Figures 5.8 and also in the bottom plot of Figure 4.11.

5. From an efficiency calculation, the results of which are displayed in Figure 4.10, S002 is the more efficient detector. This is explained by the insensitivity to incoming radiation at the innermost regions of the S003 detector, visible in Figures 5.3, 5.4, 5.5, 5.6 and 5.7. The reason for this difference in the effective

radius of the bore hole is not clear.

6. The alignment of the crystals with respect to the scanning table coordinate axes is defined to a high level of precision in Section 5.3. However, unless the positioning of the cryostat within the laboratory can be reproduced, this alignment cannot be used on other datasets. It would be beneficial to future users of the prototypes, and the ensuing asymmetric detectors, if a common and accurate reference frame or dedicated measuring apparatus could be incorporated in the outer cryostat design such that the alignment of a crystal or crystals within their cryostats can be identified. This would not only benefit the characterisation process but also the ultimate placing of the detectors in their array configuration.

7.2 Parametric Pulse Shape Analysis

Standard pulse shape analysis techniques were conducted to form a 2-dimensional spatial calibration of the S002 detector, based on polynomial fitting of pulse parameters. This is described in Section 5.4 to Section 5.6. Applying the method adopted to the S002 scan dataset gives a spatial resolution in x and y of 5.0 mm. Application of this method to the S003 dataset gives a spatial resolution of 9.3 mm. Generally, the third ring of each detector performs the best and this is believed to be due to the radial nature of the electric field lines in the near-coaxial geometry of these regions.

The spatial resolution achieved was poorer than expected. This is likely to be due to the difficulties encountered in fitting the complicated parameter distributions. No attempt to separate multiple interaction sites due to Compton scattering within a segment was made in this work and furthermore the low standard deviations of parameters suggest that the pulse shapes are not significantly affected. This is discussed in more detail in Section 5.6.1.

This work has not attempted to investigate any energy dependance in the pulse parameters obtained. Clearly the number of charge carriers produced will be affected by the energy of the incoming radiation. The discussion in Section 2.4.4 implies that the amount of charge induced from a particular interaction location will be proportional to the number of number of charge carriers present. However, it is expected that the relative sizes of the induced pulses, and hence the Image Charge Asymmetry, will remain consistent across energies. This could be verified by taking a small number of coincidence measurements (discussed briefly in Section 4.2) using a source with more than one gamma-ray energy, for example ^{152}Eu. The effect of varying gamma-ray energy on pulse risetimes could be more complicated due to the fact that the presence of some charge carriers could cause a pertubation in the electric field strength seen by the other charges and hence affect their mobility. The measurement discussed above could easily discount this.

7.3 Experimental Data

Although a single AGATA detector has been used in an in-beam experiment in the past [St05], many challenges were encountered by the AGATA Collaboration [AG03] in the set-up of the triple cluster experiment. This is evident in the difficulties that arose in the offline calibration of the spectra, caused by drifting of the electronics. This drifting can be seen in Section 6.2 and is made more curious by the change in the trend between tapes 18 and 20. It is readily perceived that this should and can be avoided in the future. Furthermore, offline analysis would benefit from a greater emphasis on the aquisition and availibility of calibration data.

Alignment of the detectors with respect to one another as well as with the laboratory frame is also a significant issue. For the analysis of the experimental dataset, the position of one reference point of the triple cluster was defined, as discussed in Section 6.1.1. It was then assumed in this work that the inter-crystal spacing was

uniform throughout the length of the tapered edges and that there was no rotation of the crystals about their central axes or angles of axial tilt (other than that which is necessary for the crystals to tesselate due to their tapering). Item 6 in the above list could endeavour to understand the crystals' positioning more easily as well as a separate definition for each of the crystals' locations.

The experimental analysis was unnecessarily complicated due to the ambiguous production mechanism of ^{49}Ti, discussed in Section 6.3. The attempt to separate the fusion-evaporation and transfer reaction channels was laborious and the basic principles used to differentiate between them envoked little conviction. Investigation into the suitability of future experiments which use the performance of the Doppler correction as an indicator of the spatial resolution achievable is recommended. Two possible experimental approaches could be suitable. A fusion evaporation reaction with highly inverse kinematics would produce stongly forward focussed residual nuclei. An assumption that these nuclei were travelling in the beam direction would eliminate the requirement for a particle detector and allow for a greatly simplified experimental analysis. The beam and target could be chosen such that the cross section for nucleon transfer was negligible. Alternatively a nucleon transfer reaction in which the fusion evaporation cross section was significantly lower could be devised.

7.4 Doppler Correction

The pulse shape parameterisation procedure described in Chapter 5 was applied to the experimental data to locate the photon interaction sites. This was then used to impove the energy resolution of the spectral peaks by calculating the photon's angle of emission from the recoiling nucleus and then correcting the Doppler shifted photon energy according to Equation 2.40. The best improvement to a spectral peak was obtained from events that occured in the S003 detector. The inadequacies of S001 and S002 are attributed to the problems in the set-up of the electronics. The best

energy resolution obtained from the Doppler correction of the experimental spectra was 7.3 keV at a peak energy of 1382 keV (0.5 %). This figure is 71 % lower than the FWHM obtained using detector level spatial information (25.4 keV), and 34 % lower than the FWHM obtained using segment level spatial information (11.1 keV). The energy resolution obtained by the S003 detector is predicted by Figure 3.8 for the achieved spatial resolution of this detector (9.3 mm). Thus the theoretical relationship is proven for the S003 detector.

The best energy resolutions were achieved for the S003 detector, despite the spatial calibration being performed on the S002 detector. This would imply that the difference in the pulse shape parameters between the two detectors is not the most significant factor in applying the Doppler correction, and gives confidence in the ability to use one detector's spatial calibration for the other detectors.

The use of the incorrect positioning of the Ge detectors is discussed in Section 6.5. It is believed that the Doppler correction applied in ths work could be significantly improved upon by using the correct positioning of the Ge detectors. The Doppler correction could further be improved by selecting the subset of the experimental data tapes which follow the same pattern of electronic drift (tapes 6 to 18), as observable in Figure 6.10. All of the experimental data tapes were used in this work due to the apparent limited statistics associated with the transfer reaction. Furthermore, an attempt to correct the data using the value of v/c obtained for the fusion evaporation reaction could impove the energy resolution achieved following the Doppler correction, as it appears to be the strongest producer of ^{49}Ti according to Figure 6.25.

Some of the pulse shape database PSA methods discussed in Section 3.4.2 have proven to produce greater improvements to the Doppler corrected spectra than the parametric approach discussed in this work. However there is still much room for improvement in this method. For example, analysis of data acquired in scans of the

detectors' tapered sides can be analysed with a view to calibrating the image charge asymmetry of the vertically adjacent segments as a function of vertical position. Thus, the third dimension of an interaction site can be inferred. In addition, improvements to the interaction position determination algorithm, described in Section 5.6, could be made. For example, investigation into further iterations of the pulse parameters is suggested. Other avenues of investigation include the possibility of using the polarity of image charges in neighbouring segments to give a rough indication of the interaction radius. This would enable the exclusion of one of the possible radial determinations arising from the minimum stationary points in the parameter trends, visible in Figure 5.19.

This work has gone some way to validate the use of a parametric approach to pulse shape analysis for use in a tracking array. However, in order to be viable the method needs further work; the suggestions made in this Chapter would provide a step towards achieving this.

Appendix A

Table of Constants

Description	Symbol	Value	Units
Permittivity of free space	ϵ_0	8.854×10^{-12}	Fm^{-1}
Electronic charge	e	1.602×10^{-19}	C
Electron rest mass energy equivalent	m_0	511.0	keV
Proton rest mass energy equivalent	m_p	938.3	MeV
Density of Aluminium	ρ_{Al}	2.70	gcm^{-3}
Density of Silicon	ρ_{Si}	2.33	gcm^{-3}
Density of Titanium	ρ_{Ti}	4.51	gcm^{-3}
Speed of light in a vacuum	c	3×10^{8}	ms^{-1}
Germanium atomic number	Z	32	-
Germanium density	ρ_{Ge}	5.32	gcm^{-3}
Relative permittivity of Germanium	ϵ	16	-
Germanium Fano factor (at 77K)	F	$\sim$0.1	-
Germanium Ionisation Energy (at 77K)	ϵ	2.96	eV

Table A-1: Properties of germanium and other constants used in this work. The germanium data is largely taken from [Kn00] and the other constants from [NI08b].

Appendix B

Excerpts from the S002 Data Sheets

The following pages contain scanned images of the data sheets for the S002 AGATA prototype detector supplied by the detector and cryostat maufacturers [Can] [CTT] that are relevant to this work.

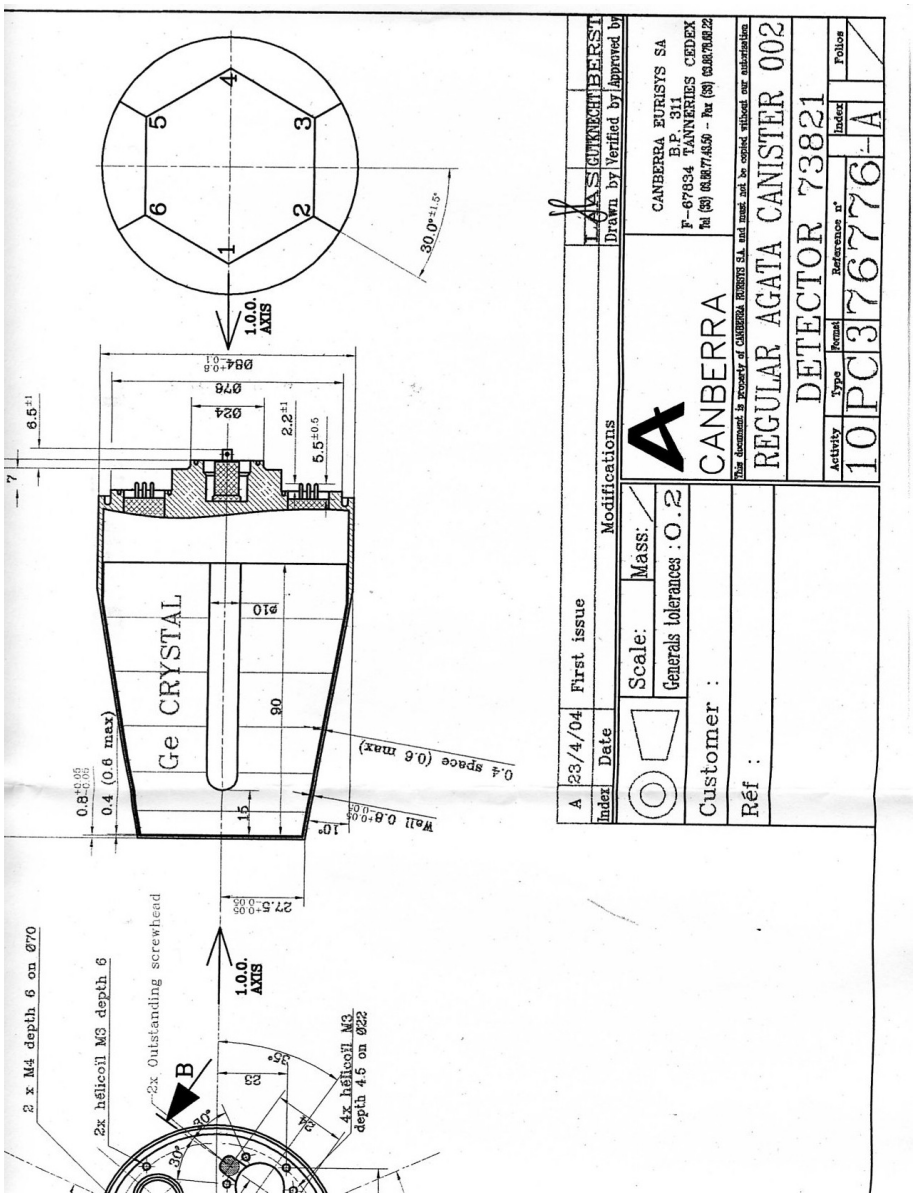

Figure B-1: Scanned image of a page from the S002 data sheets. The diagram shows the location of the [100] crystalographic axis.

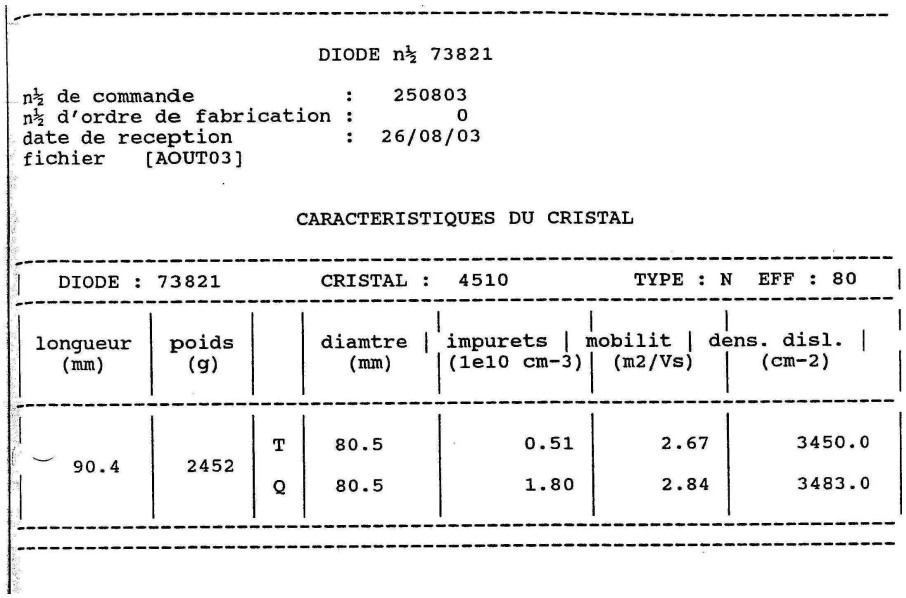

DIODE n½ 73821

n½ de commande : 250803
n½ d'ordre de fabrication : 0
date de reception : 26/08/03
fichier [AOUT03]

CARACTERISTIQUES DU CRISTAL

DIODE : 73821 CRISTAL : 4510 TYPE : N EFF : 80

longueur (mm)	poids (g)		diamtre (mm)	impurets (1e10 cm-3)	mobilit (m2/Vs)	dens. disl. (cm-2)
90.4	2452	T	80.5	0.51	2.67	3450.0
		Q	80.5	1.80	2.84	3483.0

Figure B-2: Scanned image of a page from the S002 data sheets. The table shoos the impurity concentration of the detector at T and Q. This labelling is described by Figure C-4.

Appendix C

Excerpts from the S003 Data Sheets

The following pages contain scanned images of the data sheets for the S003 AGATA prototype detector supplied by the detector and cryostat maufacturers [Can] [CTT] that are relevant to this work.

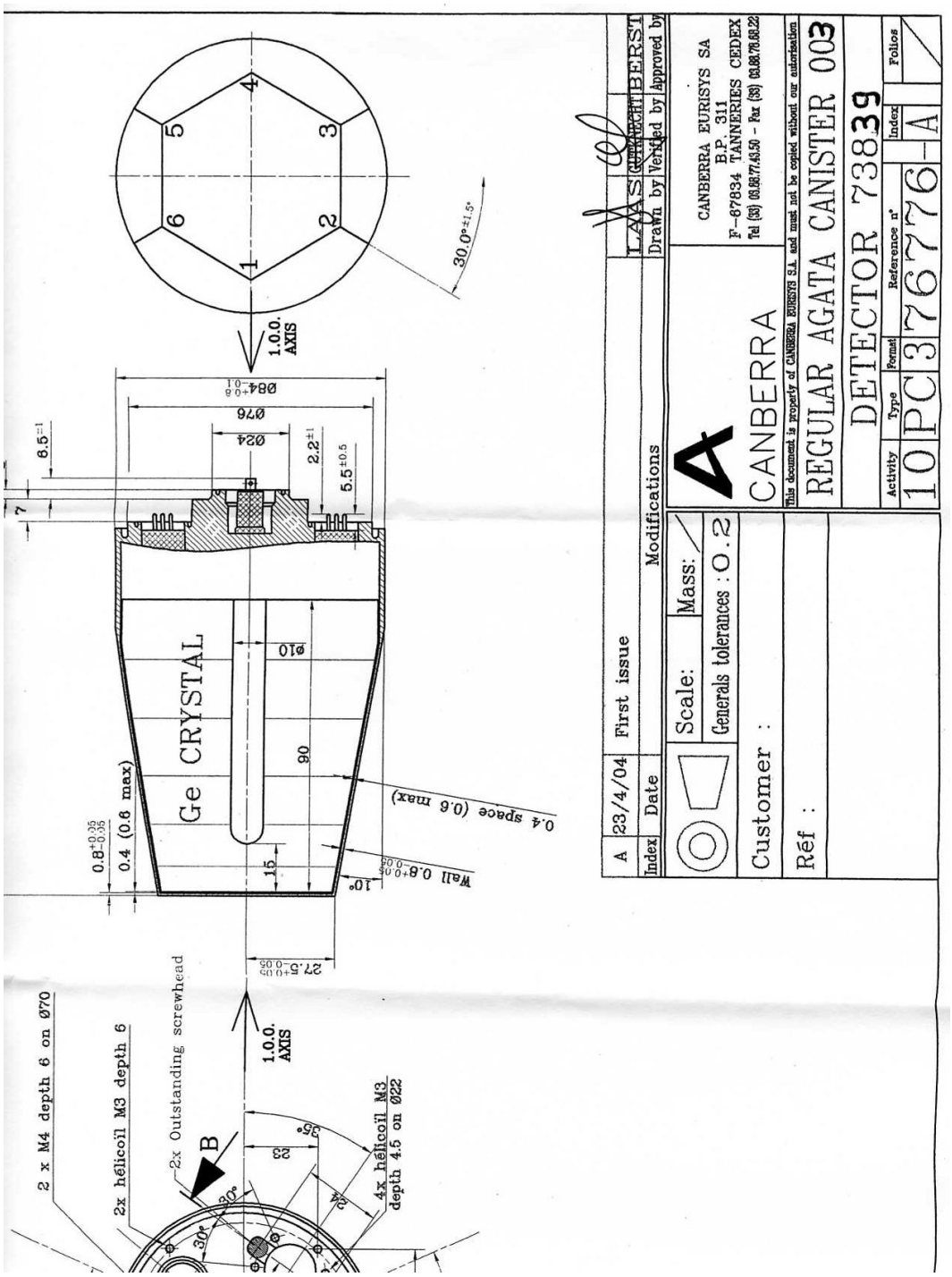

Figure C-1: Scanned image of a page from the S003 data sheets. The diagram shows the location of the [100] crystalographic axis.

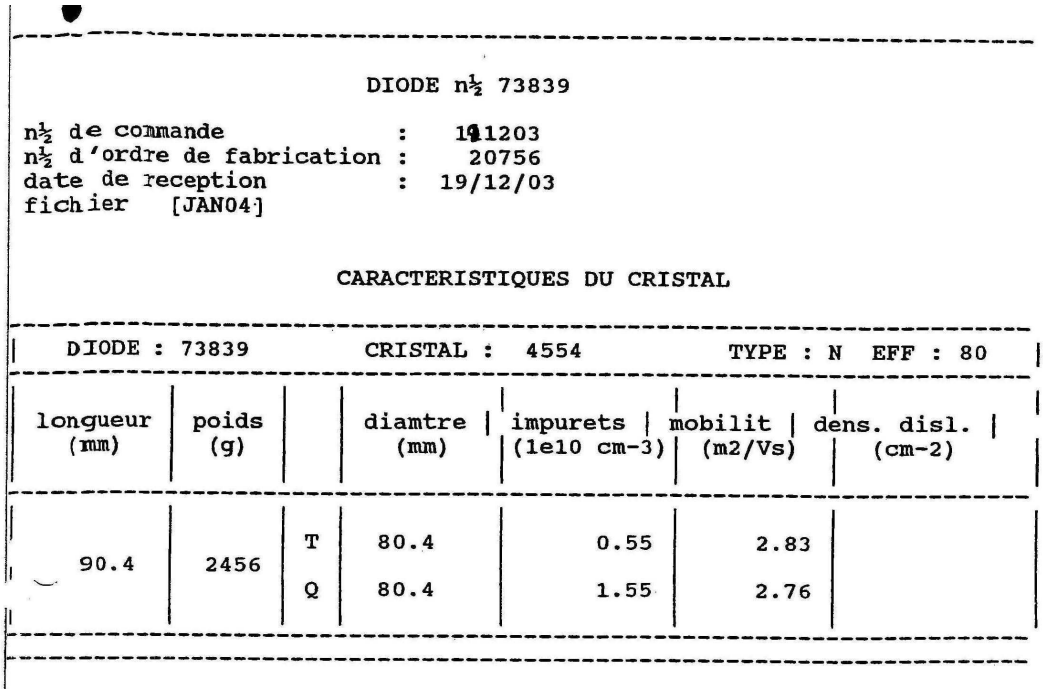

DIODE n½ 73839

n½ de commande : 111203
n½ d'ordre de fabrication : 20756
date de reception : 19/12/03
fichier [JAN04]

CARACTERISTIQUES DU CRISTAL

DIODE : 73839 CRISTAL : 4554 TYPE : N EFF : 80

longueur (mm)	poids (g)		diamtre (mm)	impurets (1e10 cm-3)	mobilit (m2/Vs)	dens. disl. (cm-2)
90.4	2456	T	80.4	0.55	2.83	
		Q	80.4	1.55	2.76	

Figure C-2: Scanned image of a page from the S003 data sheets. The table shows the impurity concentration of the detector at T and Q. This labelling is described by Figure C-4.

DIODE n½ 73839

[JAN04.dat]

PREVISION / TENSION DE DEPLETION

diamtre extrieur : 80.4 mm
diamtre intrieur : 11.0 mm

	position (mm)	conc. *e10 cm-3	Vdep. (V)	Vdep.(r=0) (V)
tte	0.00	0.55	2279.0	2513.1
1 / 5	18.08	0.75	3107.7	3427.0
2 / 5	36.16	0.95	3936.4	4340.9
3 / 5	54.24	1.15	4765.1	5254.8
4 / 5	72.32	1.35	5593.8	6168.6
[illegible]e	90.40	1.55	6422.5	7082.5

Figure C-3: Scanned image of a page from the S003 data sheets. The table shoos the impurity concentration of the detector at various crystal depths.

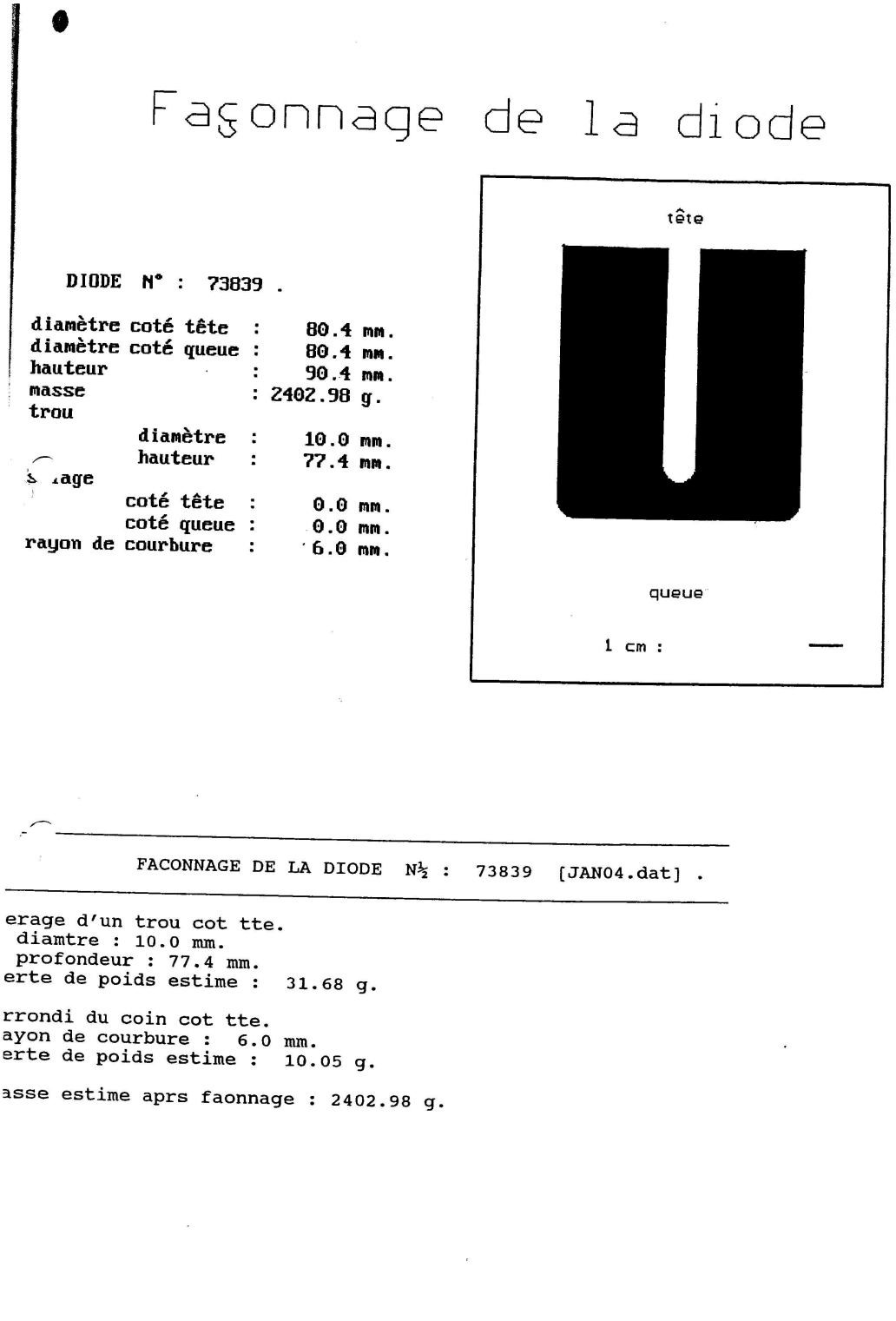

Façonnage de la diode

DIODE N° : 73839 .

diamètre coté tête	:	80.4 mm.
diamètre coté queue	:	80.4 mm.
hauteur	:	90.4 mm.
masse	:	2402.98 g.
trou		
diamètre	:	10.0 mm.
hauteur	:	77.4 mm.
ş ıage		
coté tête	:	0.0 mm.
coté queue	:	0.0 mm.
rayon de courbure	:	6.0 mm.

FACONNAGE DE LA DIODE N½ : 73839 [JAN04.dat] .

erage d'un trou cot tte.
diamtre : 10.0 mm.
profondeur : 77.4 mm.
erte de poids estime : 31.68 g.

rrondi du coin cot tte.
ayon de courbure : 6.0 mm.
erte de poids estime : 10.05 g.

asse estime aprs faonnage : 2402.98 g.

Figure C-4: Scanned image of a page from the S003 data sheets. The diagram shows the locations of T and Q with respect to the cystal geometry.

Appendix D

Relevant Stopping Powers

This section details the stopping powers of the projectiles used in the experiment described in Chapter 6. The stopping powers were used to estimate the average energy lost per unit path length in the Titanium target material, Aluminium absorber and the Silicon detector, where appropriate.

D-1 Stopping of Protons

Figure D-1 displays the average energy lost per unit path length of protons in Titanium and Aluminium due to both nuclear and electronic processes. Figure D-2 shows the average energy lost per unit path length of protons in Silicon due to electronic processes only.

D-2 Stopping of ^{2}H Ions

Figure D-3 displays the average energy lost per unit path length of ^{2}H ions in Titanium and Aluminium due to both nuclear and electronic processes. Figure D-4 shows the average energy lost per unit path length of ^{2}H ions in Silicon due to electronic processes only.

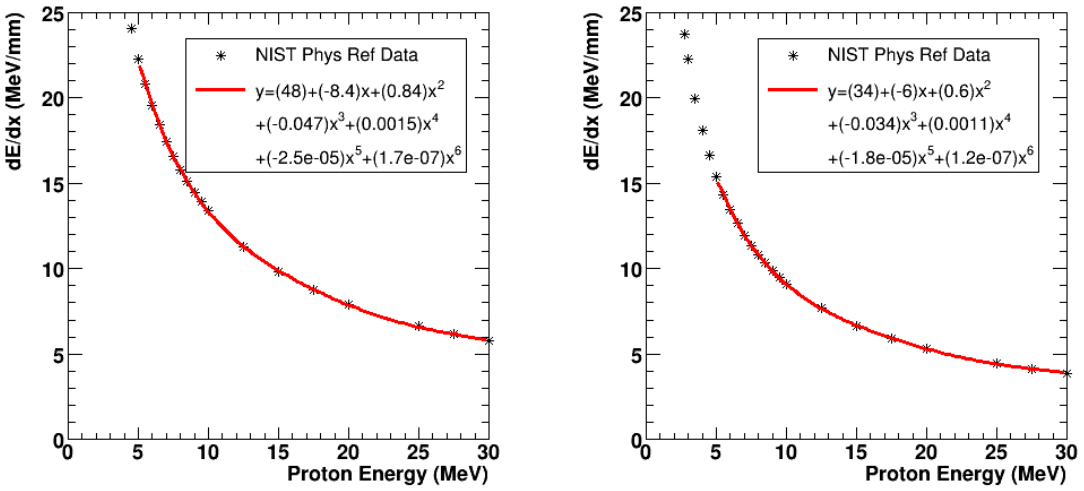

Figure D-1: Total stopping power of protons in Titanium (*left*) and Aluminium (*right*). The data is taken from [NI08a] and fitted with a sixth order polynomial in an appropriate range, the equation of which is also shown.

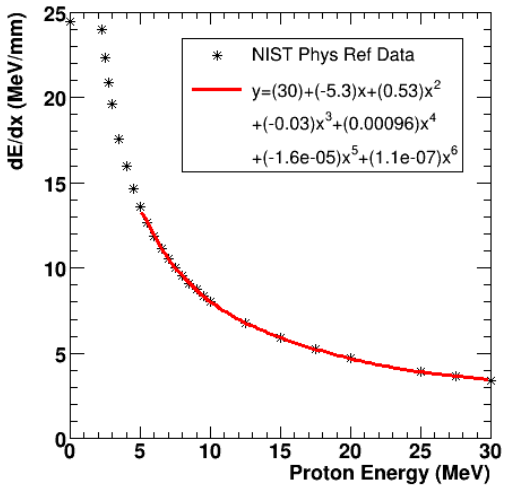

Figure D-2: Electronic stopping power of protons in Silicon. The data is taken from [NI08a] and fitted with a sixth order polynomial in an appropriate range, the equation of which is also shown.

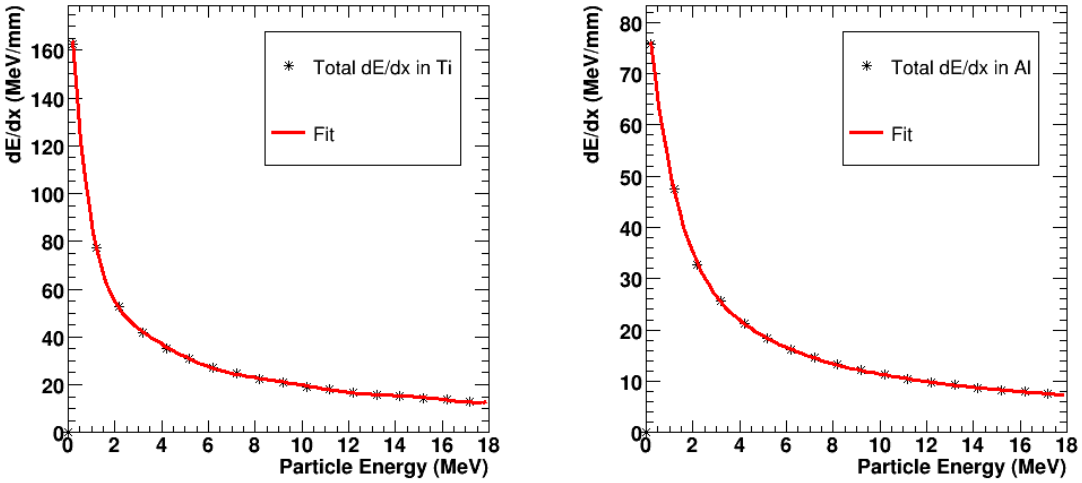

Figure D-3: Total stopping power of ^{2}H ions in Titanium (*left*) and Aluminium (*right*). The data is taken from a calculation performed using local software [Go97] and fitted with a sixth order polynomial in an appropriate range.

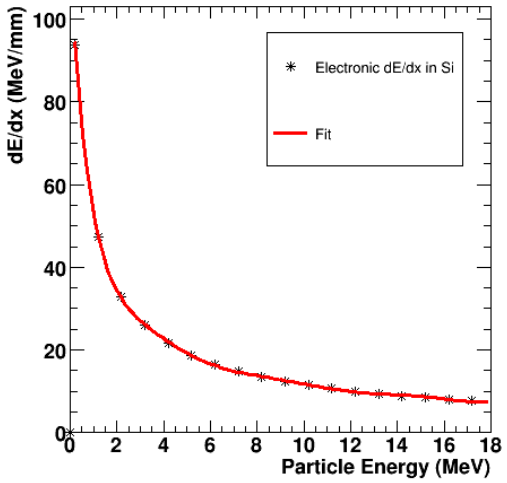

Figure D-4: Electronic stopping power of ^{2}H ions in Silicon. The data is taken from a calculation performed using local software [Go97] and fitted with a sixth order polynomial in an appropriate range.

D-3 Stopping of ^{12}C Ions

Figure D-5 displays the average energy lost per unit path length of ^{12}C ions in Titanium and Aluminium due to both nuclear and electronic processes. Figure D-6 shows the average energy lost per unit path length of ^{12}C ions in Silicon due to electronic processes only.

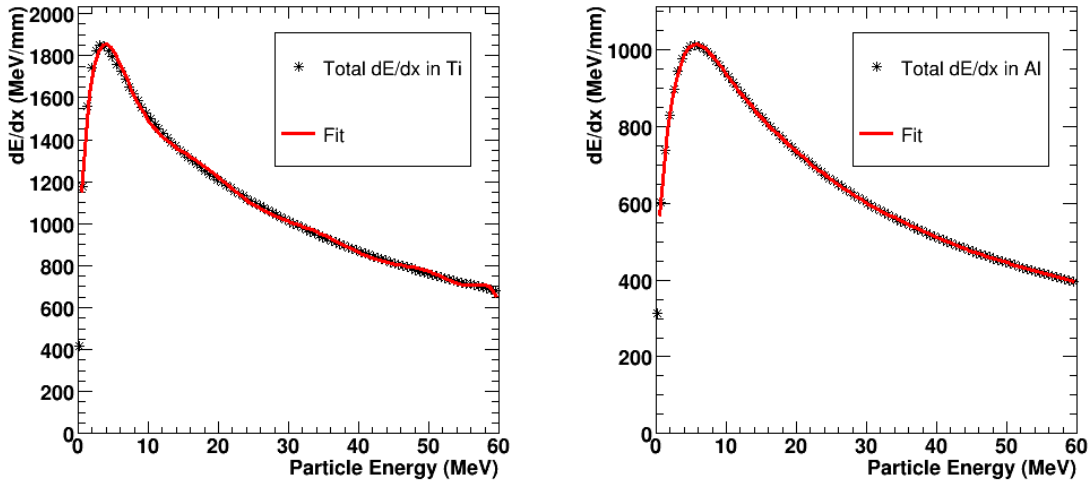

Figure D-5: Total stopping power of ^{12}C ions in Titanium (*left*) and Aluminium (*right*). The data is taken from a calculation performed using local software [Go97] and fitted with a high order polynomial in an appropriate range.

D-4 Stopping of ^{16}O Ions

Figure D-7 displays the average energy lost per unit path length of ^{16}O ions in Titanium and Aluminium due to both nuclear and electronic processes. Figure D-8 shows the average energy lost per unit path length of ^{16}O ions in Silicon due to electronic processes only.

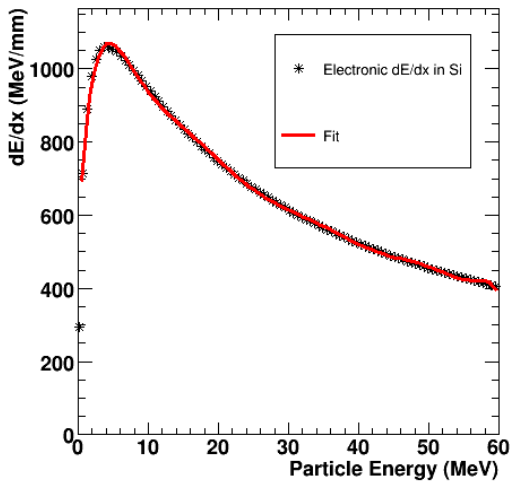

Figure D-6: Electronic stopping power of ^{12}C ions in Silicon. The data is taken from a calculation performed using local software [Go97] and fitted with a high order polynomial in an appropriate range.

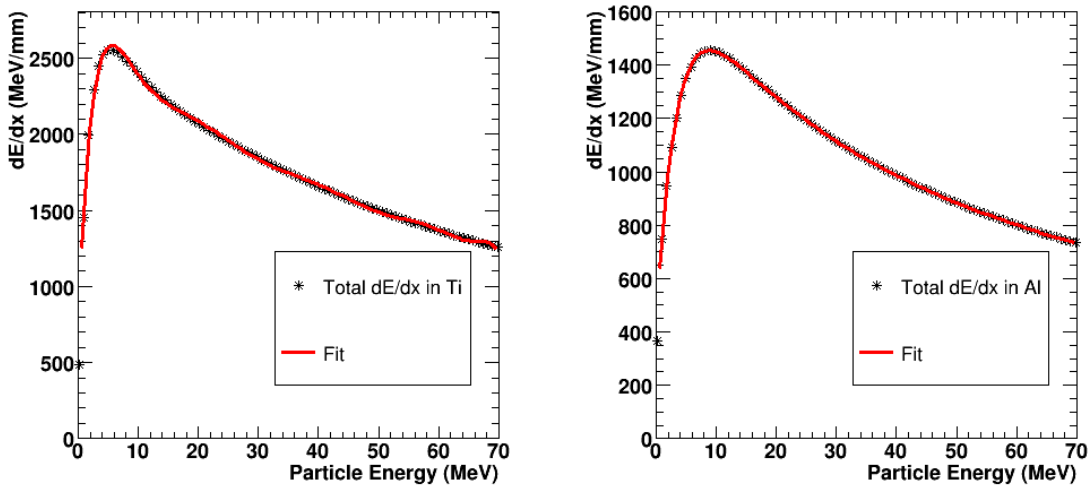

Figure D-7: Total stopping power of ^{16}O ions in Titanium (*left*) and Aluminium (*right*). The data is taken from a calculation performed using local software [Go97] and fitted with a high order polynomial in an appropriate range.

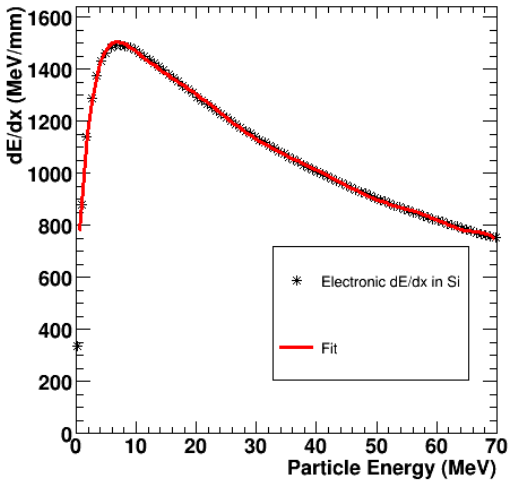

Figure D-8: Electronic stopping power of ^{16}O ions in Silicon. The data is taken from a calculation performed using local software [Go97] and fitted with a high order polynomial in an appropriate range.

D-5 Stopping of ^{48}Ti Ions

Figure D-9 shows the total stopping power of the ^{48}Ti beam particles in the target material.

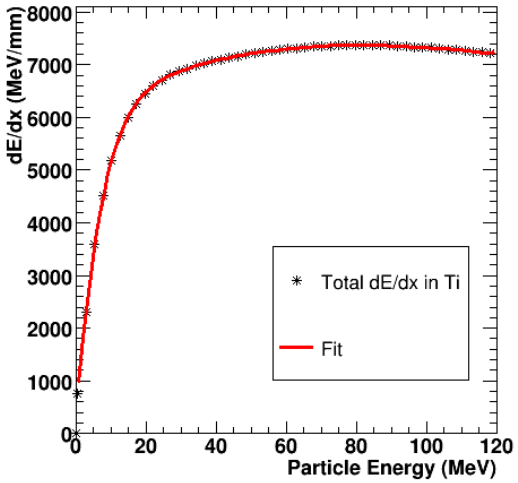

Figure D-9: Total stopping power of ^{48}Ti beam particles in Titanium. The data is taken from a calculation performed using local software [Go97] and fitted with a high order polynomial in an appropriate range.

Bibliography

[Au03] G. Audi, A.H. Wapstra, Nucl. Phys. **A729** (2003) 337

[AG03] AGATA Official Site (2008)
Website: http://www-win.gsi.de/agata/overview.htm

[Be96] C.W. Beausang and J. Simpson, J. Phys. G **22** (1996) 527

[Br77] K. Braune *et al*, GSI-Bericht J-1-77 (1977)

[Br06a] B. Bruyneel, *Characterisation of Segmented Large Volume, High Purity Germanium Detectors*, Ph.D. Thesis, University of Cologne (2006)

[Br06b] B. Bruyneel *et al*, Nucl. Inst. Meth. **A569** (2006) 264

[Can] Canberra Eurisys, Lingolsheim, Detector Manufacturer (2008)
Website: http://www.canberra.com/default.asp

[Cr07] F.C.L. Crespi *et al*, Nucl. Inst. Meth. **A570** (2007) 459

[CTT] Cryostat and Detector Technique Thomas (2008)
Website: http://www.apo-coaches.com/ctt.swf

[Cw96] S. Cwiok *et al*, Nucl. Phys. **A611** (1996) 211

[Da52] C.M. Davisson, R.D. Evans, *Gamma-Ray absorption coefficients*, Rev. Mod. Phys. **24** (1952) 79

[De88] Gammasphere Proposal *A National Gamma-ray Facility*, ed. by M.A. Deleplanque and R.M. Diamond (1988)

[De99] M.A. Delaplanque *et al*, Nucl. Inst. Meth. **A430** (1999) 292

[De02] M. Descovich, *Improving the position resolution of Highly Segmented HPGe Detectors using Pulse Shape Analysis Methods*, Ph.D. Thesis, University of Liverpool (2002)

[De05] M. Descovich *et al*, Nucl. Inst. Meth. **A553** (2005) 535

[Di07] M. Dimmock, *Characterisation of AGATA Symmetric Prototype Detectors*, Ph.D. Thesis, University of Liverpool (2008)

[Dr55] G. Dresselhaus *et al*, Phys. Rev. 98 (1955) 368

[Eb96] J. Eberth *et al*, Nucl. Inst. Meth. **A369** (1996) 135

[Eb01] J. Eberth *et al*, Prog. Part. Nucl. Phys. **46** (2001) 389

[Fa03] E. Farnea *et al*, LNL-INFN Annual Report (2003) 158

[Fe69] P. FETTWEIS and M. SAIDA'NE, Nucl. Phys. **A139** (1969) 113

[Fi96] R.B. Firestone, *Table of Isotopes, Volume I*, Eighth Edition, John Wiley and Sons (1996)

[Ge01] AGATA Proposal, *Technical Proposal for an Advanvced Gamma Tracking Array for the European Gamma Spectroscopy Community*, ed. by J. Gerl and W. Korten (2001)

[Go97] E.S. Paul, *Gostop*, Liverpool University Nuclear Structure Group Software (utilises [Br77]).

[Go03] A. Görgen, *Position sensitivity of the AGATA prototype crystal analyzed using a database of calculated pulse shapes* (2003)

[Gr90] I.S. Grant and W.R. Phillips, *Electromagnetism*, John Wiley and Sons (1990)

[Gr05] S. Gros, *Characterisation of an Exogam Clover Germanium Detector*, Ph.D. Thesis, University of Liverpool (2005)

[Gu05] D. Gutknecht, Private communication (2005)

[He01] Z. He, Nucl. Inst. Meth. **A453** (2001) 250

[Kl29] O. Klein, Y. Nishina, Z. Physik **52** (1929) 853

[Kn00] G.F. Knoll, *Radiation Detection and Measurement*, John Wiley and Sons (2000)

[Ko96] M.F. Kogan, *Electronics Noise and Fluctuations in Solids*, Cambridge Univ. Press (1996)

[Kr88] K.S. Krane, *Introductory Nuclear Physics*, John Wiley and Sons (1988)

[La04a] M. Lauer, *Digital Signal Processing for Segmented HPGe Detectors Preprocessing Algorithms and Pulse Shape Analysis*, Ph.D. Thesis, Heidelberg University (2004)

[La04b] I.H. Lazarus *et al*, Trans. Nucl. Sci. **51** (2004) 1353

[Le93] W.R. Leo, *Techniques for Nuclear and Particle Physics Experiments*, Springer-Verlag (1993)

[Le03] I.Y. Lee *et al*, Rep. Prog. Phys. **66** (2003) 1095

[LI02] D. Bazin *et al*, Nucl. Instr. and Meth. **A482** (2002) 307.
Webpage: http://www.nscl.msu.edu/lise

[Lu03] D. Lunney, J.M. Pearson, Rev. Mod. Phys. **75** (2003)

[Lu00] G. Lutz, *Semiconductor Radiation Detectors*, Springer-Verlag (2001)

[Ma81] P.A. Mando *et al*, Phys. Rev. **C23** (1981)

[Me04] P. Medina *et al*, IMTC Proceedings, Vol.3 (2004) 1828

[Mi00a] L. Milhailescu *et al*, Nucl. Inst. Meth. **A477** (2000) 350

[Mi00b] L. Milhailescu *Principles and Methods for γ-ray Tracking with Large Volume Germanium Detectors*, Ph.D. Thesis, University of Bonn (2000)

[Mi03] MIDAS, Multi Instance Data Acquisition System (2008)
Website: http://midas.psi.ch

[Mi04] L. Milechina, B. Cederwall, Nucl. Instr. and Meth. **A508** (2003) 394

[MT06] MTSort, Data Sorting Package.
Website: http://ns.ph.liv.ac.uk/MTsort-manual/MTsort.html

[No94] P.J. Nolan *et al*, Ann. Rev. Nucl. Part. Sci **45** (1994)

[Ne06] L. Nelson, *A Proposal for Scanning AGATA Detectors at the University of Liverpool in 2006*, Internal Document (2006)

[Ne07] L. Nelson *et al*, Nucl. Inst. Meth. **A537** (2007) 153

[NI08a] NIST Physical Reference Data (2008)
Webpage: http://physics.nist.gov/PhysRefData/Star/Text/contents.html

[NI08b] The NIST Reference on Constants, Units, and Uncertainty (2008)
Webpage: http://physics.nist.gov/cuu/Constants/

[NI08c] NIST XCOM: Photon Cross Sections Database (2008)
Webpage: http://physics.nist.gov/cgi-bin/Xcom/xcom2

[Ol06] A. Olariu *et al*, Trans. Nucl. Sci. **53** (2006) 1028

[Ol07] A. Olariu *Matrix Method on the Liverpool Coincidence Scan Data*, PSA Team Meeting Presentation, CSNSM, Orsay (2007)

[Or08] Ortec HPGe Detector Manufacturer (2008)
Webpage: http://www.ortec-online.com/detectors/photon/a1_1.htm

[Ot75] G. Ottaviani *et al*, Trans. Nucl. Sci. NS-22 (1975) 192

[Pa07] Parker, Motion and Control Technology Comapany (2008)
Website: http://www.parker.com/portal/site/PARKER

[Pu04a] A. Pullia *et al*, IEEE Nuclear Science Symposium Conference Record (2004)

[Pu04b] A. Pullia *et al*, IEEE Trans. Nucl. Sci. **51** (2004) 831

[qv96] E.S. Paul, *Qval*, Liverpool University Nuclear Structure Group Software

[Ra39] S. Ramo, *Currents induced by electron motion*, Proceedings of the I.R.E. (1939) 584

[Re06] F. Recchia, Private Communication (2006)

[Ro04] C. Rossi Alvarez, Brazillian Journal of Physics **34** (2004) 3A

[Re07a] F. Recchia, Acta Physica Polonica **B38** 1297

[Re07b] F. Recchia, *Status of the AGATA in-beam test experiment*, 5th AGATA Week Presentation (2007)

[RO07] ROOT, Object oriented data analysis package (2008)
Website: http://root.cern.ch

[Sc99] G.J. Schmid *et al*, Nucl. Inst. Meth. **A430** (1999) 69

[Sc05a] H. Scheid *First Experiments at REX-ISOLDE and MINIBALL*, GANIL Seminar Presentation (2005)

[Sc05b] H.C. Scraggs *et al*, Nucl. Inst. Meth. **A543** (2005) 431

[Sh38] W. Shockley, J. Appl. Phys. **9** (1938) 635

[Sh50] W. Shockley, Phys. Rev. **78** (1950) 173

[Si97] J. Simpson *et al.*, Z Phys **A358** (1997) 139

[Si00] J. Simpson *et al.*, APH N.S. Heavy Ion Physics **11** (2000) 159

[St67] V.M. Strutinsky, Nuclear Physics **A95** (1967) 420

[St68] V.M. Strutinsky, Nuclear Physics **A122** (1968) 1

[St05] T. Steinhhardt, *A First In-Beam-Experiment with the 36-fold Segmented AGATA-Detector*, Orsay AGATA Week Presentaion (2005)

[TW77] M. Igarashi, TWOFNR code (1977).
Website: http://www.tac.tsukuba.ac.jp/∼yaoki/twofnr.pdf

[Tw86] P.J. Twin *et al*, Phys. Rev. Lett. **57** (1986) 811

[Ve00a] K. Vetter *et al*, Nucl. Inst. Meth. **A452** (2000) 105

[Ve00b] K. Vetter *et al*, Nucl. Inst. Meth. **A452** (2000) 223

[Ve07] R. Venturelli, *GRID SEARCH - Last News*, PSA Team Meeting Presentation, CSNSM, Orsay (2007)

[Xi08] XIA, Nuclear Instrumentation Company (2008)
Website: http://www.xia.com/DGF_products.html